Two-dimensional, Hydrodynamic Modeling of Electrothermal Plasma Discharges

Micah J. Esmond

Dissertation submitted to the Faculty of the
Virginia Polytechnic Institute and State University
in partial fulfillment of the requirements for the degree of

Doctor of Philosophy
in
Mechanical Engineering

Leigh Winfrey, Co-Chair
Francine Battaglia, Co-Chair
Yang Liu
Brian Vick
Wayne Scales

May 2, 2016
Blacksburg, Virginia

Keywords: Electrothermal plasma, capillary discharge, plasma simulation

Two-dimensional, Hydrodynamic Modeling of Electrothermal Plasma Discharges

Micah J. Esmond

ABSTRACT

A two-dimensional, time-dependent model and code have been developed to model electrothermal (ET) plasma discharges. ET plasma discharges are capillary discharges that draw tens of kA of electric current. The current heats the plasma, and the plasma radiates energy to the capillary walls. The capillary walls ablate by melting and vaporizing and by sublimation. The newly developed model and code is called the Three-fluid, 2D Electrothermal Plasma Flow Simulator (THOR). THOR simulates the electron, ion, and neutral species as separate fluids coupled through interaction terms. The two-dimensional modeling capabilities made available in this new code represent a tool for the exploration and analysis of the physics involved in ET plasma discharges that has never before been available.

Previous simulation models of ET plasma discharges have relied primarily on a 1D description of the plasma. These models have often had to include a tunable correction factor to account for the vapor shield layer — a layer of cold ablated vapor separating the plasma core from the ablating surface and limiting the radiation heat flux to the capillary wall. Some studies have incorporated a 2D description of the plasma boundary layer and shown that the effects of a vapor shield layer can be modeled using this 2D description. However, these 2D modeling abilities have not been extended to the simulation of pulsed ET plasma discharges. The development of a fully-2D and time-dependent simulation model of an entire ET plasma source has enabled the investigation of the 2D development of the vapor shield layer and direct comparison with experiments. In addition, this model has provided novel insight into the inherently 2D nature of the internal flow characteristics involved within the

plasma channel in an ET plasma discharge. The model is also able to capture the effects of inter-species interactions.

This work focuses on the development of the THOR model. The model has been implemented using C++ and takes advantage of modern supercomputing resources. The THOR model couples the 2D hydrodynamics and the interactions of the plasma species through joule heating, ionization, recombination, and elastic collisions. The analysis of simulation results focuses on emergent internal flow characteristics, direct simulation of the vapor shield layer, and the investigation of source geometry effects on simulated plasma parameters. The effect of elastic collisions between electrons and heavy species are shown to affect internal flow characteristics and cause the development of back-flow inside the ET plasma source. The development of the vapor shield layer has been captured using the diffusion approximation for radiation heat transfer within the ET plasma source with simulated results matching experimental measurements. The relationship between source radius and peak current density inside ET plasma discharges has also been explored, and the transition away from the ablation-controlled operation of ET plasma discharges has been observed.

This work is made possible by the Virginia Tech Nuclear Engineering Program.

Two-dimensional, Hydrodynamic Modeling of Electrothermal Plasma Discharges

Micah J. Esmond

GENERAL AUDIENCE ABSTRACT

Electrothermal (ET) plasma discharges are created by passing large amounts of electrical current down the axis of a narrow cylindrical channel. This process deposits significant amounts of energy into the channel and the temperature of the gas in the channel becomes very high. The temperatures are so high that the gas in the channel becomes ionized and forms a plasma. At these very high temperatures, the channel wall material melts and evaporates. The temperatures inside these devices can be so high that the channel wall material can also change directly from a solid into a vapor, a process called sublimation. The melting, evaporation, and sublimation of the channel wall material is called ablation. The addition of ablated material into the channel causes an increase in the density and pressure of the plasma inside the channel. Typically, the channel is opened on one end and plasma is ejected out.

This ejected plasma from an ET plasma discharge can be used in a variety of applications. These applications include propulsion, solid fuel ignition, and mass acceleration. In order to understand the operation of these types of discharges, simulation models have been used. Simulation models are mathematical models that break down a large, complex problem into many smaller, simpler problems. These smaller problems are simple enough so that a computer can be used to solve many of them very quickly. By accumulating the solutions offered by a computer, a researcher is able to estimate a solution to the larger, complex problem.

With the steady advancement in computing power over recent years, there is a need to advance simulation models in order to efficiently leverage available computing power.

By advancing simulation models for ET plasma discharges in this way, additional insight and understanding regarding their operation may be obtained. This new information can aid in the design and implementation of these devices for specific purposes. In addition, this new information may expand the applicability of these devices to different uses. The advancement of the simulation capabilities for ET plasma discharges is the focus of this work. The development of a new simulation model that utilizes modern computing power is presented. Several observations made using this new simulation model are presented and discussed.

This work is made possible by the Virginia Tech Nuclear Engineering Program.

Acknowledgments

This work is made possible by the Virginia Tech Nuclear Engineering Program. I am deeply grateful for the commitment, attention, and support from my advisor, Dr. Leigh Winfrey. She has made this work possible with her positivity and encouragement and has indeed made this experience an enjoyable one. I am also very thankful to my committee members — Dr. Battaglia, Dr. Liu, Dr. Scales, and Dr. Vick — for their guidance and advice. Many others are to be thanked as well including Dr. Bourham at North Carolina State University for his never-ending enthusiasm and helpful discussion. I also want to acknowledge the use of experimental measurements taken using the Plasma Interaction with Propellant Experiment (PIPE) located at North Carolina State University. In addition, Advanced Research Computing (ARC) has provided the computational resources that have contributed greatly to the results reported in this work. Specifically, I want to mention that this work was supported in part by NSF grant CNS-0960081 and the HokieSpeed supercomputer at Virginia Tech. ARC has provided excellent resources and user support and I thank and commend them for the work in which they are engaged. Lastly, I am very grateful for the many useful discussions

shared with members of the **B** and **E** Applied Research and Science (BEARS) Laboratory at Virginia Tech and the University of Florida.

Contents

List of Figures

List of Tables

Attribution

The manuscripts included in Chapters 4, 5, 6, and 7 are co-authored by my advisor, Leigh Winfrey. I am indebted to her for her commitment, support, and advice as I've prepared these manuscripts.

Chapter 1

Introduction

1.1 Introduction to Plasma

Plasmas have captured the interest of scientists, researchers, and engineers from around the world due to their versatility, diversity, and beauty. Plasmas have provided the means necessary to develop breakthrough technology in the areas of materials processing, combustion processes, and nuclear energy. Plasmas exist in a wide range of length scales, time scales, temperatures, and densities. Many individuals have enjoyed the captivating sights of plasmas as they've peered into camp fires, witnessed a lightning flash, or gazed into a clear night sky.

Introductions to plasmas have been developed and exist in many shapes, sizes, and depths. A detailed and thorough introduction to plasma with a focus on the fundamental

theory of plasma interactions is offered by Mitchner and Kruger [1]. A more contemporary and general introduction to plasmas is offered by Bittencourt [2]. An introduction to fundamental plasma parameters and processes from the perspective of detailed plasma-fluid modeling has recently been offered by Thompson [3]. The introduction to plasmas contained in this work will focus on a basic qualitative overview of plasmas and introduce definitions and background important to the content of this work.

1.1.1 Plasma Overview

Plasmas are gases that have been invested with sufficient amounts of energy so that a portion of the atoms that make up the gas have been stripped of one or more of their orbiting electrons. The process of removing these electrons is called ionization. The ionization process is illustrated in Fig. 1.1. The ionization process requires energy input which is often provided by an energized particle such as an electron, photon (i.e. packet of light), or even another atom. The amount of energy required to remove an electron from an atom varies depending on the type of atom. Table 1.1 shows the amount of energy required to remove a single electron from a neutral atom of selected elements. An electron volt (or eV) is the amount of energy gained by an electron as it is accelerated through one volt of an electric field. One eV is equal to about 10^{-19} joules. A joule is roughly the amount of energy an apple gains as it is accelerated through a distance of one meter by the gravitational field of the earth. An electron with a kinetic energy of 1 eV travels at a velocity of 5.9×10^5 m/s. By comparison, a proton with a single eV of kinetic energy travels at 1.4×10^4 m/s.

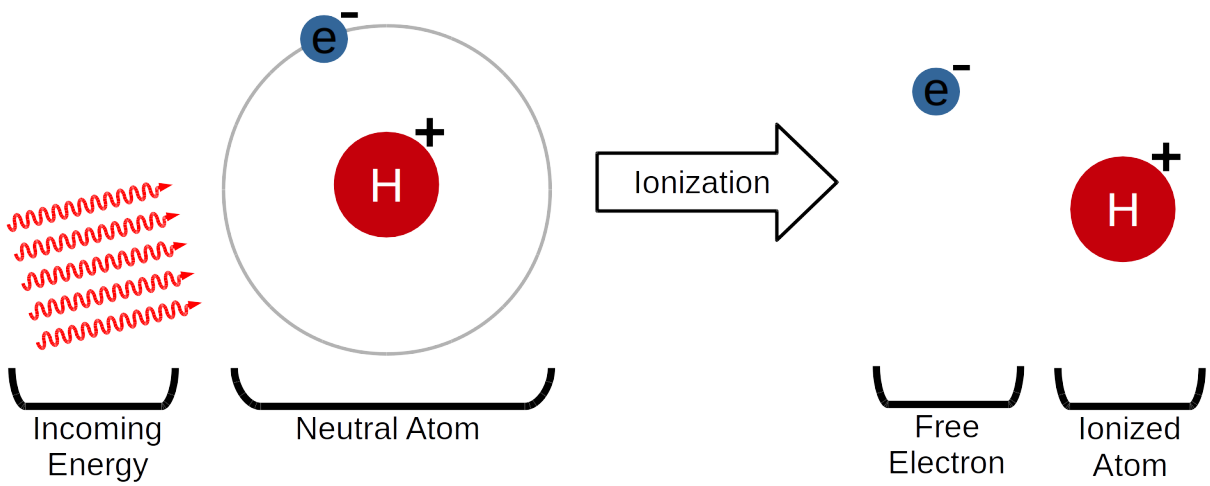

Figure 1.1: Ionization is the process of removal of a negatively charged electron from the positively charged nucleus of an atom. This process requires energy which is delivered to an atom by various means. The result is an ionized atom and a free electron.

Table 1.1: Required ionization energy for neutral atoms of select elements.

Element	Ionization energy (eV)
Hydrogen	13.6
Carbon	11.3
Oxygen	13.6
Iron	7.9
Argon	15.8

The opposite of the ionization process is a process called recombination. This is the process where an electron reattaches to an atom. During this process, a phenomenon called photoluminescence can occur. Photoluminescence is the process in which a photon with a particular wavelength (i.e. color) is released from the atom in order to carry away excess energy contained in the recombining electron. Different elements will give off different colors during this process depending on the configuration of their electrons. This phenomenon is a large part of why plasmas can exhibit such visually interesting behavior.

Plasmas can exist in a variety of forms. Plasmas can be partially ionized or fully ionized depending on how much energy is available. The percent ionization of a plasma is defined as:

$$\text{percent} \quad \text{ionization} = \frac{n_i}{n_n + n_i} 100\% \tag{1.1}$$

where n_i is the number density of ionized atoms (i.e. ions), and n_n is the number density of neutral atoms. A plasma with only 0.1% ionization can exhibit plasma-like behavior. Plasmas can exist in a wide range of temperatures. Fire, or flame, is an example of a low-temperature plasma. Flames have a sufficient amount of charged particles to exhibit plasma-like behavior. Flames typically have a temperature of about 2000 K (0.2 eV). High temperature plasmas exist in the solar corona where plasma temperatures can exceed 1,000,000 K (86 eV). The solar core has a very high temperature of approximately 15,000,000 K (1.3 keV). Plasmas can also be classified by their density. Flames and solar corona tend to have plasma densities of approximately 10^{15} charged particles/m^3. The solar core boasts a plasma density of approximately 10^{30} charged particles/m^3. As matter becomes cooler and

more dense, plasmas are eventually impossible to form and matter takes on the more familiar forms of gases, liquids, and solids.

1.1.2 Fundamental Plasma Concepts

Electric and Magnetic Fields

The versatility of plasmas is due primarily to their ability to be controlled by electric and magnetic fields. However, it is often the electromagnetic nature of plasmas that drives their complexity and gives rise to unpredictable and unexpected behavior. An introduction to electromagnetism is beyond the scope of this work, but excellent work on this subject has been produced by Griffiths [4]. An electric field applies a force on charged particles that acts parallel to the electric field lines. When the particles are not constrained, they will accelerate along these field lines, and oppositely charged particles are accelerated in opposite directions. Magnetic fields cause charged particles to move perpendicular to the direction of the field lines. This often causes charged particles to gyrate about magnetic field lines. The motion induced on charged particles by electric and magnetic field lines is illustrated in Fig. 1.2. The resulting force on charged particles in the presence of electric and magnetic fields is called the Lorentz force and it is given by:

$$\mathbf{F} = q(\mathbf{E} + \mathbf{v} \times \mathbf{B}) \tag{1.2}$$

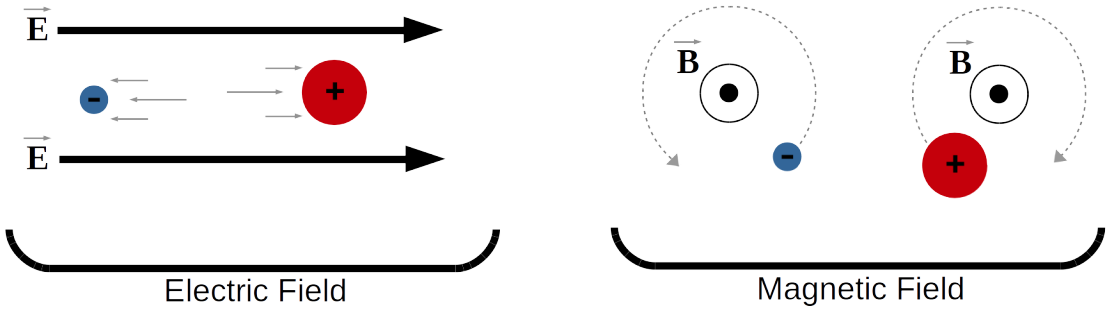

Figure 1.2: Motion induced by electric and magnetic fields on charged particles. The magnetic field lines are directed out of the page.

where q is the charge on the particle, $\mathbf{E}$ is the electric field, $\mathbf{v}$ is the particle velocity, and $\mathbf{B}$ is the magnetic field.

The behavior of electric and magnetic fields is governed by Maxwell's equations for electromagnetics. Maxwell (1831-1879) developed the theory of electromagnetism which is now represented by the set of equations bearing his name. His work has been widely studied in great detail. Maxwell's equations reveal that the electric and magnetic fields are tightly coupled such that changes in either field affects the other. This gives rise to mathematical complexity and the physical complexity of plasma behavior.

Debye Shielding

As Maxwell's equations indicate, the presence of charged particles induces electric fields, and oppositely charged particles affect each other due to these induced fields. The interactions between charged particles due to these induced electric fields are called Coulombic interactions. The sphere of influence about a charged particle in which its Coulombic in-

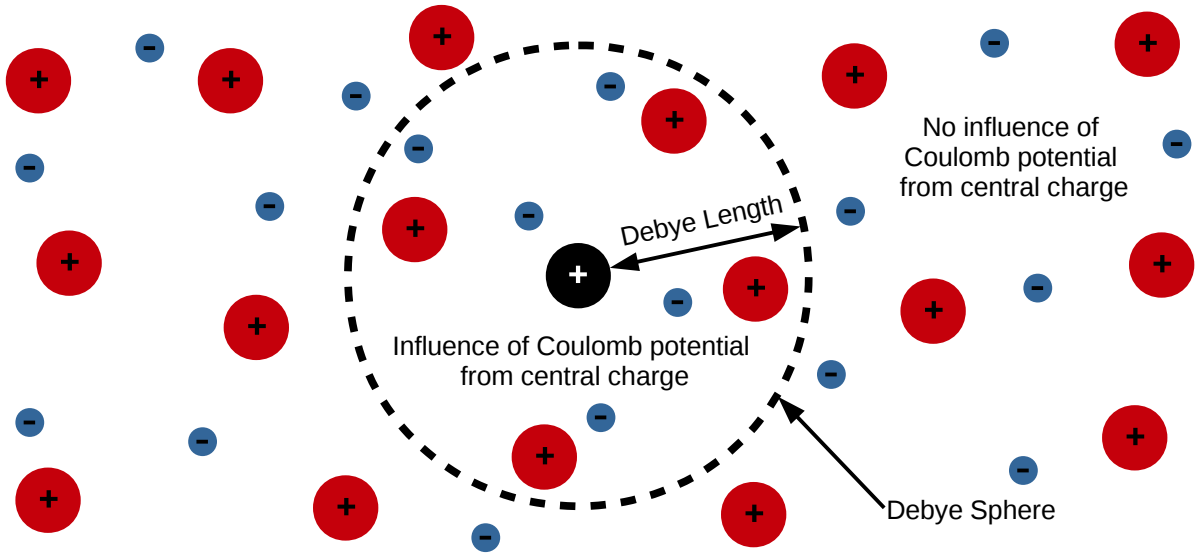

Figure 1.3: A 2D representation of the Debye sphere in an ideal plasma. The surrounding cloud of charged particles within the Debye sphere blocks the influence of the central charged particle on particles farther away than the Debye length.

teractions play an important role is characterized by the Debye length. In other words, the Debye length (λ_D) is a measure of how far from a charged particle its induced electric field influences other charged particles around it. Debye shielding is the concept of shielding of the Coulombic effects arising from the presence of a charged particle. The Debye sphere is illustrated in Fig. 1.3. For an ideal plasma, the Debye length is given by [1]:

$$\lambda_D = \sqrt{\frac{\varepsilon_0 k_B T}{n_e e^2}} \tag{1.3}$$

where ε_0 is the permittivity of free space, k_B is Boltzmann's constant, T is the plasma temperature, n_e is the electron number density, and e is the elementary charge.

Ideal plasmas are plasmas where the ratio of the electric potential energy to the kinetic (thermal) energy of interacting plasma particles is much less than one [5]. In ideal plasmas, Debye shielding is "complete" meaning that the Coulombic interaction potential is completely encapsulated within the Debye sphere. Plasma non-ideality becomes important at relatively low plasma temperatures and high plasma densities. A non-ideal plasma involves the phenomenon of "incomplete" shielding where Coulombic interactions can be important beyond the limits of the Debye sphere. An investigation of plasma ideality as it relates to the topic of this work has been presented by Winfrey [6]. For non-ideal plasmas, additional steps must be taken in order to determine the cross-section for electron-ion collisions, and thus the electron-ion resistivity.

Collisions

Particle collisions within a plasma (or any fluid) play a key role in the thermal properties of the plasma. For plasmas in particular, particle collisions can drive the transfer of momentum and internal energy between the plasma species of electrons, ions, and neutrals. Important collision parameters include the collision speed and the collision cross-section, or probability of collision. The reader is directed to the work of Mitchner and Kruger for an excellent detailed description of collision processes in plasmas [1].

In this work, the collision speed, or the relative speed of the colliding particles, is determined based on a Maxwellian distribution. The Maxwellian distribution specifies the most probable random velocity distribution of a collection of particles at a particular tempera-

ture. A detailed description and derivation of the Maxwellian distribution has been presented elsewhere [7,8]. The Maxwellian velocity distribution is given by:

$$f(\mathbf{v}) = \left(\frac{m}{2\pi k_B T}\right)^{3/2} \exp\left(-\frac{mv^2}{2k_B T}\right) \tag{1.4}$$

where $\mathbf{v}$ is the random velocity of a particle, m is the particle mass, T is the temperature, k_B is Boltzmann's constant, and $f(\mathbf{v})$ is the probability distribution for random velocities $\mathbf{v}$. Equation (1.4) represents a probability distribution in 3D velocity space, and the distribution must be integrated over this space to determine the probability of particles having random velocities within the integrated range. A more useful form of the Maxwellian distribution is the Maxwellian speed distribution. This distribution provides the probability of finding a particle with a specified range of random speeds. It is given by:

$$f(v) = \left(\frac{m}{2\pi k_B T}\right)^{3/2} 4\pi v^2 \exp\left(-\frac{mv^2}{2k_B T}\right) \tag{1.5}$$

Equation (1.5) is plotted for various temperatures and particle masses in Fig. 1.4. From the Maxwellian speed distribution, the likely speeds involved in the collisions of different plasma species are estimated. Three different characteristic thermal speeds are often used depending on the context. These speeds include the most probable speed, v_{th}, the average speed, v_{avg}, and the RMS speed, v_{rms}. Each of these speeds is represented on a Maxwellian speed distribution in Fig. 1.5. Using the Maxwellian speed distribution, one can derive the

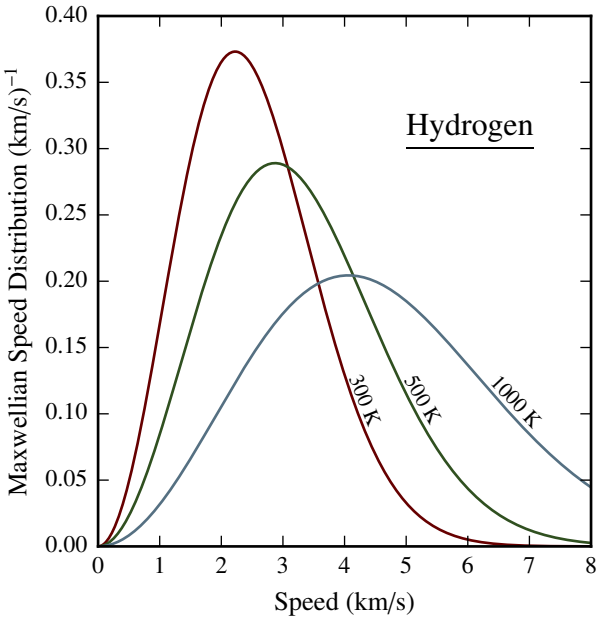

(a) The Maxwellian speed distribution for hydrogen atoms at various temperatures.

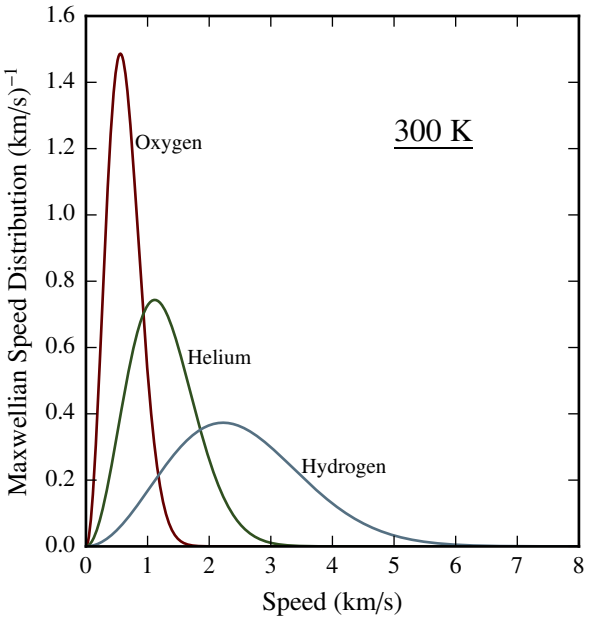

(b) The Maxwellian speed distribution for various atoms at a temperature of 300 K.

Figure 1.4: The Maxwellian speed distribution given various parameters.

expressions for each of these thermal speeds.

$$v_{th} = \sqrt{\frac{2k_B T}{m}} \tag{1.6}$$

$$v_{avg} = \sqrt{\frac{8k_B T}{\pi m}} \tag{1.7}$$

$$v_{rms} = \sqrt{\frac{3k_B T}{m}} \tag{1.8}$$

where T is the temperature of the substance, k_B is Boltzmann's constant, and m is the particle mass.

The collision cross-section for particles within a plasma can be interpreted as "the effective geometrical blocking area" which a group of particles presents to another group of

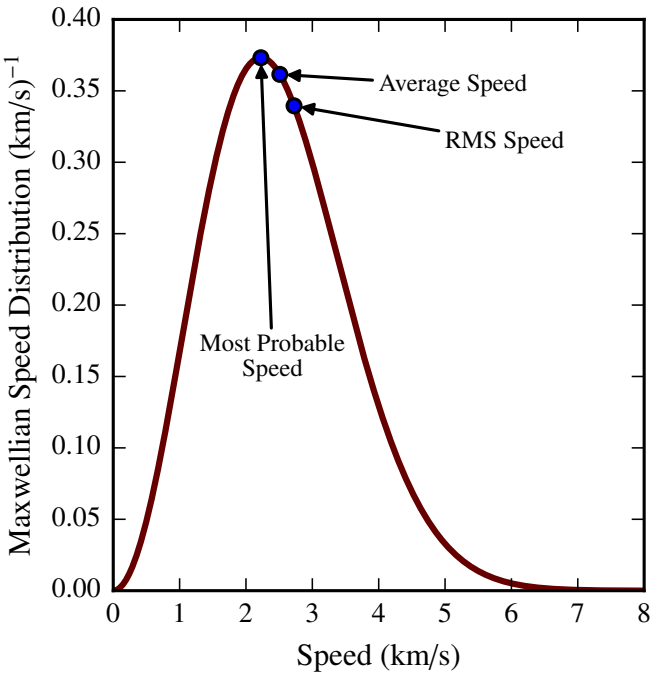

Figure 1.5: Most probable, average, and RMS speeds for a Maxwellian speed distribution.

particles [1]. When precise knowledge of collision cross-sections are needed, they can sometimes be determined experimentally. In addition, collision cross-sections are usually dependent on particle speeds, and therefore, a Maxwellian-averaged collision cross-section, $\bar{Q}$, is often sought. When only estimates of the collision cross-section are required, a hard-sphere approximation is appropriate. This approximation deduces the geometric blocking area from the particles' atomic radii. This concept is illustrated in Fig. 1.6. As indicated in Fig. 1.6, the geometric blocking area based on the hard-sphere approximation is given by:

$$\bar{Q}_{12} = \pi(r_1 + r_2)^2 \tag{1.9}$$

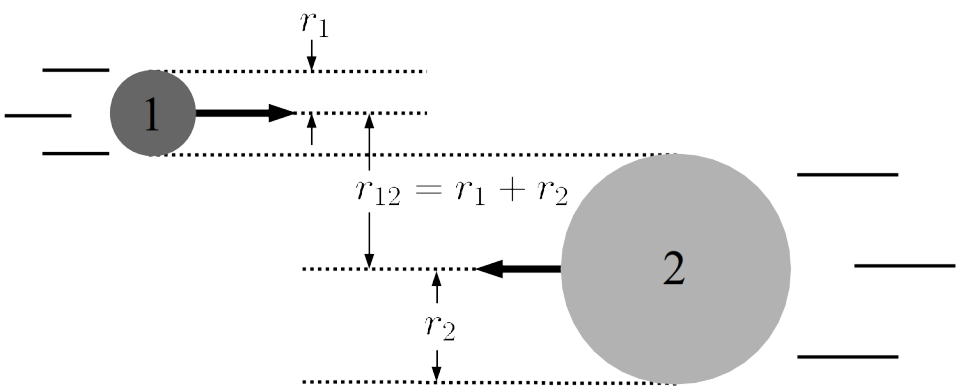

Figure 1.6: Determination of the collision cross-section based on a hard-sphere approximation.

where $\bar{Q}_{12}$ is the approximation of the Maxwellian-averaged collision cross-section for collisions between particles of types 1 and 2, r_1 is the atomic radius of particles of type 1, and r_2 is the atomic radius of particles of type 2.

The hard-sphere approximation is valid if Coulomb interactions are not involved. Naturally, Coulombic interactions can alter the collision cross-section substantially from a hard-sphere approximation. The determination of the collision cross-section for collisions involving Coulomb interactions has been studied in much detail due to its relevance to estimating the electrical conductivity of a plasma. Early investigations include the works of Cohen, Spitzer, Routly, and Harm [9, 10]. These researchers focused on the estimation of the electrical conductivity for an ideal plasma. Their approximations were widely used but were eventually challenged because of their inability to correctly predict the electrical conductivity of non-ideal plasmas. Zollweg and Liebermann [11] altered Spitzer's form for the plasma electrical conductivity in order to provide better estimates for non-ideal plasmas. Their work was later improved upon by Zaghloul et al. [5] who conducted a more thorough analytical treatment

of the underlying mathematics. The result is an expression for the collision cross-section for electron-ion collisions for both ideal and non-ideal plasmas.

The Maxwellian-averaged collision frequencies for collisions between plasma species are computed from the species densities, collision speeds, and collision cross-sections. For electron-ion collisions, the collision frequency is given by:

$$\bar{\nu}_{ei} = n_i v_{avg,e} \bar{Q}_{ei} \tag{1.10}$$

where $v_{avg,e}$ is the average thermal velocity of the electrons, n_i is the ion number density, and $\bar{Q}_{ei}$ is the Maxwellian-averaged, electron-ion collision cross-section. Similarly, the Maxwellian-averaged, electron-neutral collision frequency is given by:

$$\bar{\nu}_{en} = n_n v_{avg,e} \bar{Q}_{en} \tag{1.11}$$

where n_n is the neutral species number density, and $\bar{Q}_{en}$ is the Maxwellian-averaged collision cross-section which can be determined from a hard-sphere approximation.

Electrical Conductivity

The electrical conductivity of a partially ionized plasma is given by [1]

$$\sigma = \frac{n_e e^2}{m_e \bar{\nu}_{eh}} = \frac{n_e e^2}{m_e(\bar{\nu}_{en} + \bar{\nu}_{ei})} = \left(\frac{m_e(\bar{\nu}_{en} + \bar{\nu}_{ei})}{n_e e^2}\right)^{-1}$$
$$= \left(\frac{m_e \bar{\nu}_{en}}{n_e e^2} + \frac{m_e \bar{\nu}_{ei}}{n_e e^2}\right)^{-1} = \left(\frac{1}{\sigma_{en}} + \frac{1}{\sigma_{ei}}\right)^{-1} \quad (1.12)$$

where e is the elementary charge, n_e is the electron number density, m_e is the electron mass, $\bar{\nu}_{eh}$ is the collision frequency between electrons and heavy particles, $\bar{\nu}_{ei}$ is the electron-ion collision frequency, $\bar{\nu}_{en}$ is the electron-neutral collision frequency, σ_{ei} is the electrical conductivity due to electron-ion collisions, and σ_{en} is the electrical conductivity due to electron-neutral collisions. Refinements to this approach of calculating the plasma's electrical conductivity have been presented by Woods [7]. Woods recommends that the plasma electrical conductivity due to electron-ion collisions be adjusted as follows. For an unmagnetized plasma with $Z = 1$ (i.e. singly ionized):

$$\sigma_{ei} = 1.98 \frac{n_e e^2}{m_e \bar{\nu}_{ei}} \quad (1.13)$$

This correction is recommended based on Chapman-Enskog approximations. The Chapman-Enskog approximations focus on the estimations of transport properties for a gaseous substance in which the speed distribution of the individual particles deviates slightly from a Maxwellian distribution. Chapman-Enskog theory is thoroughly explained by Chapman [12].

1.2 Introduction to Nuclear Fusion

As discussed in Sec. 1.1, plasmas are formed when the electrons orbiting an atom's nucleus are removed after the addition of energy. Atomic nuclei are made up of protons and neutrons. These protons and neutrons are bound together by what is known as the nuclear force. This nuclear force is strong enough to keep individual protons and neutrons in a tight packet at an atom's nucleus.

Nuclear interactions fall into three basic categories: fusion, fission, and radioactive decay. Radioactive decay occurs as atomic nuclei change forms by releasing electrons, neutrons, protons, photons, or other whole nuclei. Nuclear fission is a type of radioactive decay in which a relatively large or heavy nucleus divides into similarly sized fission products. Nuclear fusion is the process of combining smaller or lighter nuclei into at least one heavier nucleus. The nuclear fission and fusion processes are illustrated in Fig. 1.7. Many nuclear interactions involve the release of energy that can be harnessed to provide heat for the generation of electricity. A thorough discussion of the physical details involved in these processes is offered by Lamarsh [13].

The concept of leveraging nuclear interactions in order to produce electrical energy was first demonstrated at Argonne National Lab with the Experimental Breeder Reactor (EBR-1) in 1951 [14]. EBR-1 harvested the energy released from nuclear fission reactions. This type of nuclear energy harvesting is used throughout the world, and in 2014, the United States generated 19.5% of its electricity using nuclear power [15].

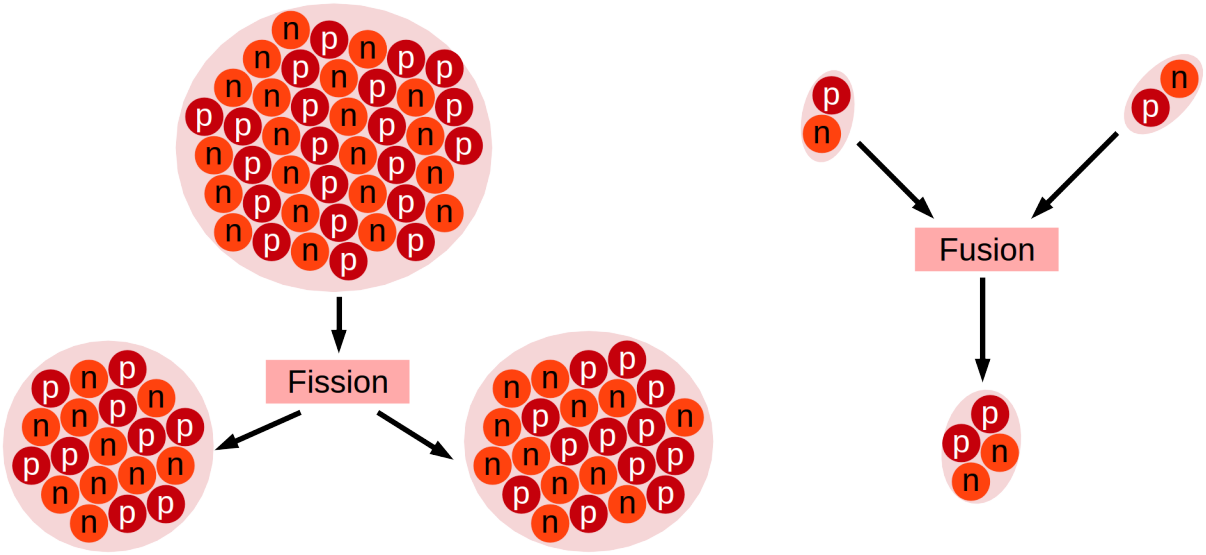

Figure 1.7: The nuclear fission and fusion processes. Protons (p) and neutrons (n) form nuclei.

Nuclear fusion presents an alternative way to harvest nuclear energy. It is an attractive alternative due to the greater energy yields from nuclear fusion reactions compared with nuclear fission. The development of nuclear fusion technology has focused on the fusion of hydrogen nuclei to form a helium nucleus and release substantial amounts of energy. In order for this fusion reaction to occur, very specific and often extreme environments must be produced and sustained. These environments are characterized by very high temperatures. At these high temperatures, the gaseous particles involved are essentially fully ionized and so the fusion reaction occurs in a fusion plasma. High temperatures are required for the fusion reaction so that hydrogen nuclei collide at sufficient velocities to overcome the Coulomb barrier (or electrostatic repulsion). Once the Coulomb barrier is overcome, the nuclear force binds the hydrogen nuclei together to form a helium nucleus. In the aftermath, an energetic neutron is also released. This process is illustrated in Fig. 1.8. Due to the high temperatures

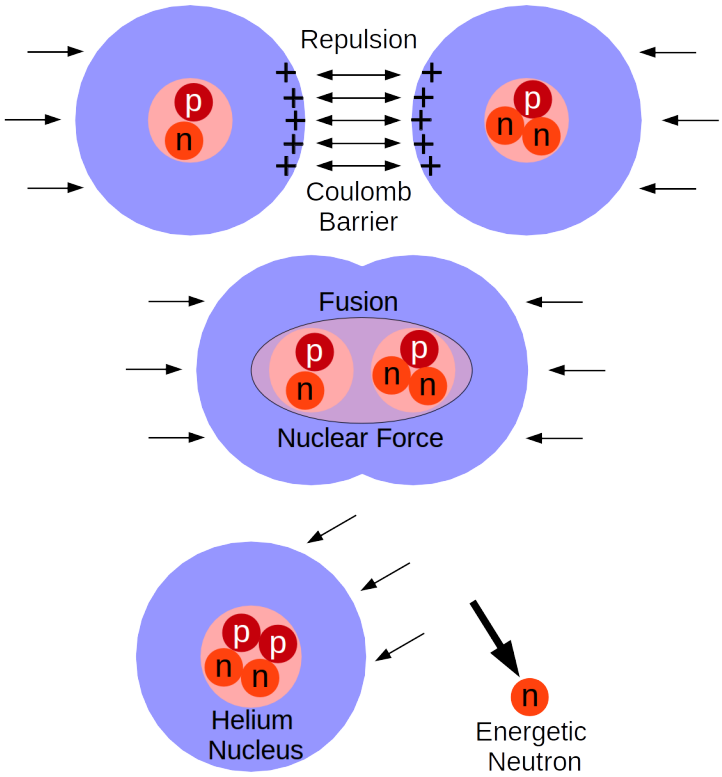

Figure 1.8: The fusion of hydrogen nuclei (deuterium and tritium) to form a single helium nucleus and an energetic neutron. The temperature (i.e. speed) of the colliding nuclei must be high enough to enable the nuclei to overcome the Coulomb barrier in order for fusion to occur.

of the fusion plasma, it cannot be confined by any known material without the material becoming damaged through melting and ablation. As a result, unique confinement methods are required.

There are three primary methods for fusion plasma confinement. The first confinement method is gravitational confinement. As indicated by its name, gravitational confinement relies on the gravitational field produced by a massive object to confine the fusion plasma. This type of confinement is used to facilitate nuclear fusion in stars and is the most common form of confinement in the universe. It is not practical for nuclear energy production on earth

because earth's gravitational field is not strong enough. The second type of confinement is inertial confinement. Inertial confinement relies on accelerating hydrogen nuclei together in such a way that their momentum is sufficient to overcome the Coulomb barrier. This type of confinement is common in small laboratory fusion devices that use electric fields to accelerate the hydrogen nuclei. This is called inertial electrostatic confinement. Inertial confinement is also accomplished using focused laser beams to compress and accelerate hydrogen nuclei together in order to overcome the Coulomb barrier. This type of fusion confinement is performed at the National Ignition Facility (NIF). At NIF, focused laser beams are fired at a hydrogen fuel capsule which implodes causing hydrogen nuclei to accelerate towards one another and fuse together. The third type of plasma confinement is called magnetic confinement. Magnetic confinement fusion (MCF) uses electric and magnetic fields to direct and control the motion of charged particles inside a fusion plasma.

MCF devices have received significant attention in the past decade. These devices show great promise for use as net power producers from the fusion reaction. As of 2016, most magnetically confined fusion plasmas are produced inside tokamaks. Tokamaks confine the fusion plasma in a torus shape as illustrated in Fig. 1.9. Toroidal magnetic fields point along the torus' axis while poloidal magnetic fields point perpendicular to the axis. These magnetic fields confine the plasma and facilitate the fusion reaction.

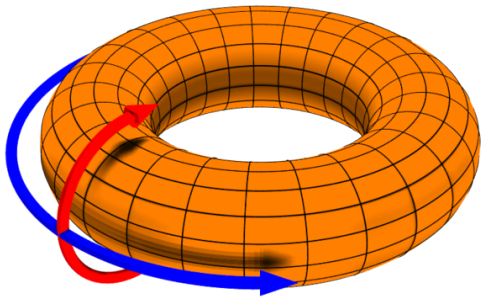

Figure 1.9: A torus shape representing the overall shape of the fusion plasma within a tokamak. Electric current flows in a loop along the axis of the torus. Toroidal and poloidal magnetic fields are used to confine the fusion plasma. Toroidal fields points parallel to the axis of the torus, and poloidal fields point perpendicular to the axis. Image used under fair use [16].

1.3 Introduction to Plasmas and CFD

Computational fluid dynamics (CFD) has enhanced the engineering design process in a wide array of disciplines. The ability to predict the effects and behavior of moving fluids under complex conditions is a tremendous aid especially in iterative design processes. CFD allows for designs to be enhanced and refined before the assembly of design prototypes saving a wealth of manufacturing resources. CFD has been used effectively in biomedical, mechanical, nuclear, and aerospace engineering.

1.3.1 The Fluid Description of Plasmas

Mathematical descriptions of plasmas have their roots in the Boltzmann equation. The Boltzmann equation governs the motion of individual particles within a substance and captures their interactions through collisions, reactions, and the Lorentz force. The Boltzmann equation is useful for describing very diffuse plasmas where the number of particles is low enough so that each one can be tracked and its motion adjusted accordingly. However, as particle densities increase, it becomes extremely difficult to model a plasma using the Boltzmann equation. An alternative to using the Boltzmann equation to model plasmas is to use particle-in-cell (PIC) methods. PIC methods use super-particles that group together individual particles and ease the computational burden of the plasma simulations. At still higher plasma densities, PIC methods become more difficult computationally and alternate methods are sought.

In very dense plasmas, the plasma can be considered a continuum and treated as a fluid. In a continuum, the distances between individual particles are very small compared with the macroscopic length scales of the system of interest. In these conditions, inter-particle collisions dominate the motion of individual particles and the substance as a whole behaves like a fluid. The equations governing the fluid behavior are derived from the Boltzmann equation and are often referred to as the equations of mass, momentum, and energy conservation. A derivation of these governing equations is offered by Meier and Shumlak [17]. By adopting a fluid description of plasmas, CFD methods can be applied and used for plasma simulation.

1.3.2 Application of CFD to Plasmas

As the industrial applications of plasmas and the availability of computational resources increases, the simulation and modeling of plasma flows has become increasingly prevalent. Some of the specific applications of CFD to plasmas include the simulation of plasma torches [18], plasma thrusters [19], cold plasma jets for biomedical applications [20], and plasma actuators for high-speed flow control [21]. Different authors have focused on different aspects of the plasma flow including detailed plasma chemistry [20–22] and non-equilibrium effects [18]. Several derivations of plasma models have also been presented. A succinct derivation and presentation of different models used for plasma simulation, including two-fluid (electron-ion), single-fluid, and magnetohydrodynamic (MHD) models, has been offered by Thompson [3]. Meier and Shumlak presented derivations for fluid models for plasma-neutral mixtures including a three-fluid (electron-ion-neutral) model and a two-fluid (plasma-neutral) model [17]. Some interesting techniques in plasma modeling have been offered in the past. An approximate Riemann solver for a two-fluid (electron-ion) plasma model has been developed and presented by Shumlak and Loverich [23]. Thompson presented a finite volume framework for the simulation of plasmas that focused on preserving the coupling of the fluid-dynamics with the full Maxwell's equations [3]. In addition Thompson was able to manipulate the governing equations in a two-fluid (electron-ion) plasma model so that the fluid equations mirrored the full Maxwell equations.

1.4 Introduction to Electrothermal Plasma Discharges

1.4.1 Physical Description

Electrothermal (ET) plasma discharges are capillary plasma discharges. A hollow capillary formed from a straight bore in a liner material forms the source of an ET plasma discharge. The dimensions of these capillaries are on the order of cm in length, and mm in internal diameter. ET discharges are produced by driving current pulses through the capillary source. Current pulses are produced via a pulse forming electrical network. Current pulses used in ET plasma devices typically have peak values on the order of tens of kA and typically have pulse lengths on the order of hundreds of µs. The current flows through the capillary heating and ionizing the plasma. The plasmas that are formed are partially ionized. Typical plasma temperatures reached in these devices range from 5,500 to 35,000 K (0.5-3 eV). Typical electron densities that develop in ET plasma discharges range from 10^{23} to 10^{25} electrons/m^3. The plasma radiates heat to the source liner material (i.e. capillary wall) which ablates adding gaseous vapor to the plasma. As the pressure, temperature, and density inside the source increase, the plasma is ejected out the open end of the source. An ET plasma source is illustrated in Fig. 1.10.

The Plasma Interaction with Propellant Experiment (PIPE) facility has been used to perform experiments on ET plasma discharges [24–27]. Some experimental current pulses generated at this facility are shown in Fig. 1.11. The PIPE experimental system is shown in Fig. 1.12. As observed in Fig. 1.12, the PIPE device is a table-top device. PIPE typically

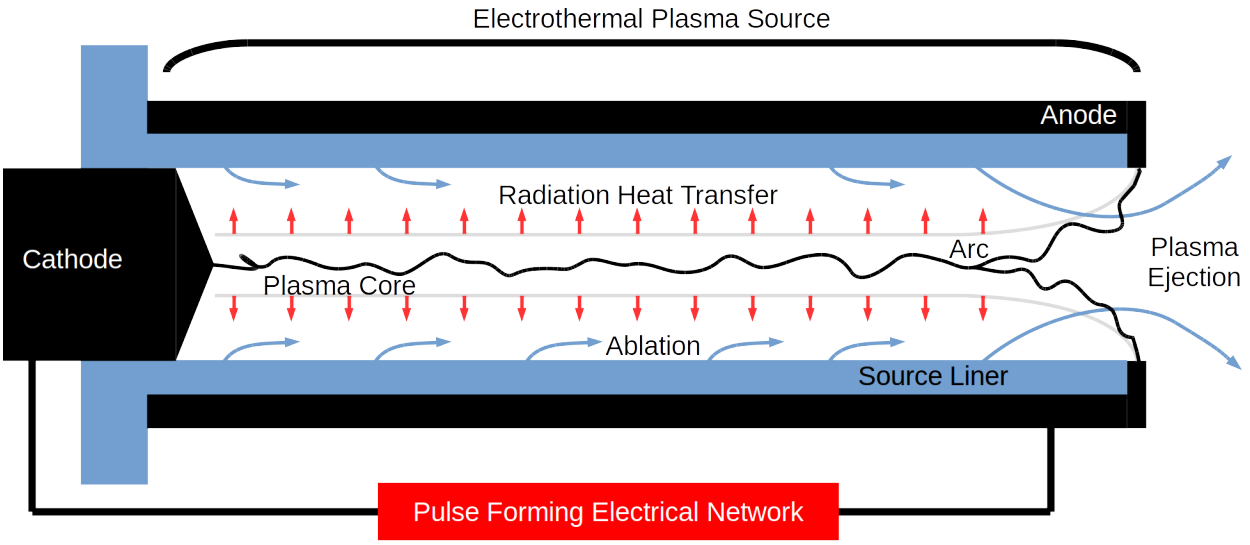

Figure 1.10: Schematic of an ET plasma source. Current flows through the capillary source and material is ablated from the source liner. The source length is on the order of centimeters and the source radius on the order of millimeters. The figure is not drawn to scale. The exit chamber is not shown.

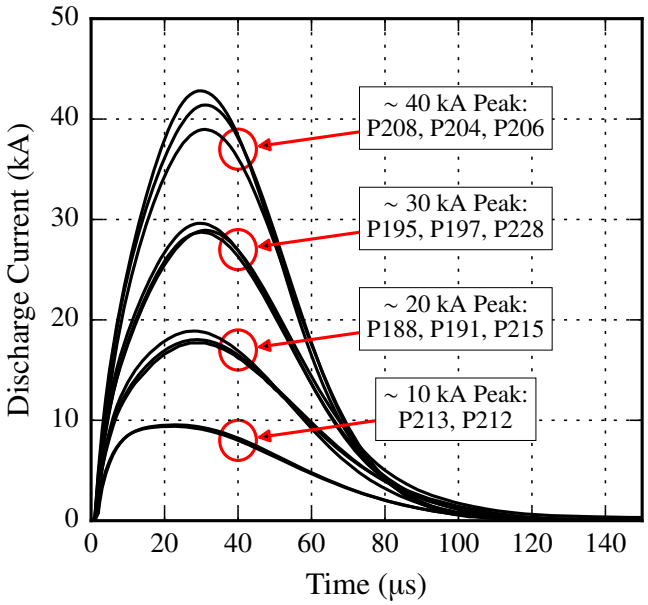

Figure 1.11: Current pulses experimentally generated at the Plasma Interaction with Propellant Experiment (PIPE). PIPE shot identifiers are specified with nominal peak current for each group of shots. These experimental current pulses are reported by Winfrey et al. [26].

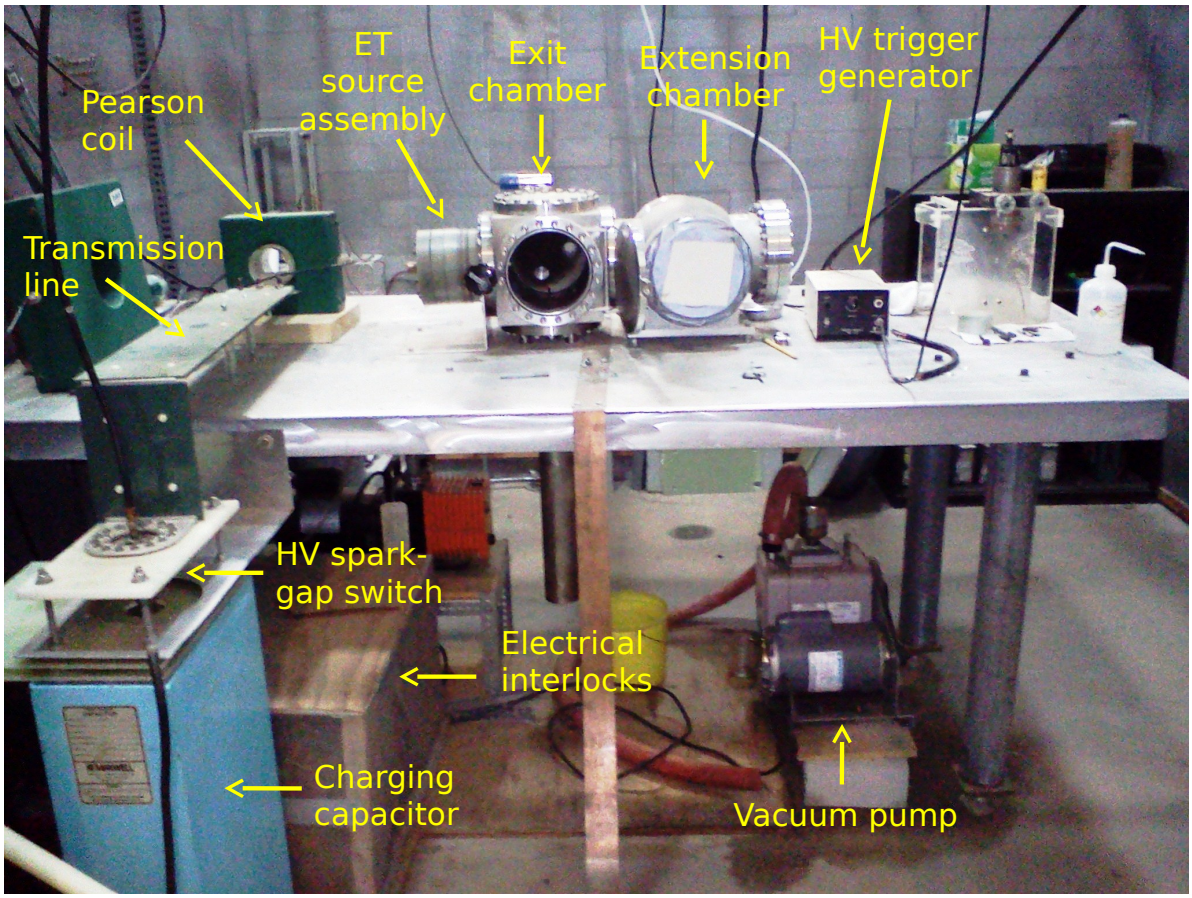

Figure 1.12: The Plasma Interaction with Propellant Experiment (PIPE) system. Important components are labeled. Image adapted from the work of Hamer [28], used with permission.

utilizes an ET source with a length of 9 cm and internal radius of 2 mm. The source liner material used in PIPE is typically Lexan polycarbonate, or $(C_{16}H_{14}O_3)_n$. In previous experimental investigation of ET plasma discharges, different liner materials have been used including polymethylmethacrylate (Acrylic) [29, 30], polytetrafluoroethylene (PTFE) [31], polyacetal [32], alumina [30], and polyethylene (PE) [33]. Niemeyer performed a range of experiments using metals, ceramics, and polymers as source liner materials [32].

1.4.2 Motivation for Study

Early Uses

Capillary plasma discharges have been investigated since the 1970s. They were referred to by several different names including evaporation-dominated, ablation-dominated, ablation-stabilized, and ablation-controlled arcs. These types of discharges were of interest due to their applications to flash lamps and switchgear technology [29, 31, 32, 34]. The studies that were conducted during this time focused on the theoretical and empirical characterization of the discharge operation in steady state. Experimental apparati consisted of open ended capillaries that were millimeters in diameter. Electrodes were placed some distance from the capillary ends. Electric current was then driven through the tube and the resulting plasma was allowed to exit in both axial directions. The work performed during this era provided the foundation for the study of ET plasma discharges in regard to other applications.

Electric Propulsion

Electric propulsion for space applications has been a motivation for the study of ablative arc discharges similar in concept to ET plasma discharges. A pulsed plasma thruster (PPT) uses these discharges in order to ablate liner materials. The ablated material is accelerated and provides the impetus for propulsion. The advantages of using PPTs include a solid propellant system, variable thrust level, thrust control, and much more [35]. The solid propellant of choice is usually Teflon, or $(C_2F_4)_n$. PPTs have been studied in significant detail with zero

and one-dimensional models [36–39]. PPTs exist in many shapes and configurations. Slab capillaries have been studied in detail by L. Pekker and O. Pekker [38, 39]. Coaxial PPTs, most similar to a capillary ET plasma discharge, have been studied by Keidar et al. [36, 37].

Mass Acceleration

Mass acceleration using ET plasma discharges has been a central focus of a significant amount of research [40–45]. At least four types of mass acceleration concepts using ET plasma discharges exist: electromagnetic-electrothermal (EMET), electrothermal-chemical (ETC), pure electrothermal (ET), and electrothermal energetic plasma sources (ETEPS). Each of these concepts is discussed briefly in this section.

Electromagnetic-electrothermal (EMET) guns utilize an ET plasma source to inject a plasma armature into a magnetic rail gun [46–48]. The injection of a plasma armature allows for more direct control of the armature properties. This control allows for the mitigation of gun bore ablation in the rail gun [46].

Electrothermal-chemical (ETC) guns utilize ET plasma discharges in order to ignite a bed of solid propellant. The ignition of the solid propellant then provides the impetus for the acceleration of a projectile. There are many advantages of using ET plasma sources as ignition mechanisms, and this concept has been studied in significant detail [40, 41, 49–53]. The use of an ET plasma discharge for this type of ignition has been shown to provide decreased ignition delay times. Decreased ignition delay times aids in the reliability and

accuracy of military ballistic devices especially in certain fire-on-the-move scenarios [51]. ETC guns also provide better burn rate control of the solid propellant and therefore offer the means to enhance muzzle velocity [40].

Pure electrothermal guns have been explored by several researchers [42, 43, 54]. The pure ET gun concept relies on the ablation and joule heating processes to create a pressure surge inside of a cylindrical capillary. This pressure surge provides the impetus to drive a projectile in an acceleration barrel. ET guns have been studied in relation to military ballistics [43], and further, a significant amount of study has been focused on the application of ET plasma launchers to fusion reactor fuelling [42, 54–57]. Pure ET guns have several advantages including a simple design, a solid propellant that can be used for multiple shots, externally adjustable muzzle energies, and much more.

Electrothermal Energetic Plasma Sources (ETEPS) represent a new concept in mass acceleration using ET plasma discharges. ETEPS sources utilize an arc discharge inside a cylindrical capillary to ablate and ignite an energetic material (e.g. a solid propellant such as JA-2). As the discharge progresses, erosive burn of the energetic material adds to the density and internal energy of the plasma inside the capillary. An energetic plasma plume then exits the capillary and can be used to drive a projectile [58, 59].

Application to Fusion Energy

The fusion of hydrogen isotopes of deuterium and tritium is a process that releases impressive amounts of energy. Magnetic confinement fusion (MCF) reactors of the future will facilitate this fusion reaction inside a fusion plasma where the temperature reaches 150,000,000 K. Pellet injection plays a central role in the operation of these types of fusion reactors. Pellet injection can be used to accomplish plasma core fuelling, edge localized mode (ELM) control, and thermal quench of the fusion plasma. Plasma core fuelling requires high-velocity ($\sim$ 1000 m/s) deuterium-tritium ice pellets to be launched into the fusion plasma [60]. The pellet velocity must be high enough so that pellets do not disintegrate before reaching the plasma core. ELMs arise due to kinks in the magnetic field lines and can produce large instabilities that damage reactor components. ELMs can be controlled by launching pellets at sufficiently high frequencies into the areas of these instabilities [61]. Fusion disruptions [62] involve the loss of high-energy particles from the fusion plasma which are then deposited on the vessel walls. The injection of pellets made out of high-Z materials (e.g. Argon) can be used to quench these types of disruptions and reduce the damage they cause [63].

The high-heat fluxes to vessel walls and components during disruption events raise concerns about the ability of first-wall materials to withstand these events. The ability to produce these high heat fluxes outside of a fusion reactor vessel will allow the rapid evaluation of materials for use in these reactors.

ET plasma discharges have captured much interest due to their potential to address these issues of pellet injection a heat flux production. ET plasma discharges exemplify promising attributes that would make them excellent candidates for fusion fuel pellet injector systems [42, 55, 56]. These discharge devices have been shown to not only provide sufficient pellet velocities, but are also capable of launching pellets at sufficient frequencies for ELM control [57]. ET plasma discharges can also be used as experimental sources of the high heat fluxes expected during fusion disruption events [27, 64–68]. ET plasma discharges have already been used to investigate the performance of Tungsten under these high heat flux conditions [68].

1.5 Objectives of Study

In order to advance the simulation capabilities of ET plasma discharges and to gain a more detailed understanding of the underlying physics involved in these devices, a number of objectives have been formulated:

- Develop a mathematical model for 2D, axisymmetric simulation of ET plasma discharges within the entire geometry of an ET plasma source.
- Implement the model in a computer code and leverage modern high performance computing resources to enhance computational efficiency.
- Investigate simulation results and report on uniquely 2D characteristics.

- Lay groundwork for further development of simulation and modeling capabilities.

Chapter 2

Literature Review

2.1 Development of Theory and Models

2.1.1 Early Investigations

Ogurtsova et al. [34], Niemeyer [32], and Ibrahim [29] conducted foundational studies of ablation-controlled arcs. They developed theoretical scaling laws and semi-empirical models and performed an array of experiments. Their theory was based on a two-zone structure of the discharge region. The region was supposed to consist of a hot plasma core surrounded by a layer of cold ablated vapor. This two-zone structure is illustrated in Fig. 2.1. This two-zone structure of the discharge was captured photographically [31, 32].

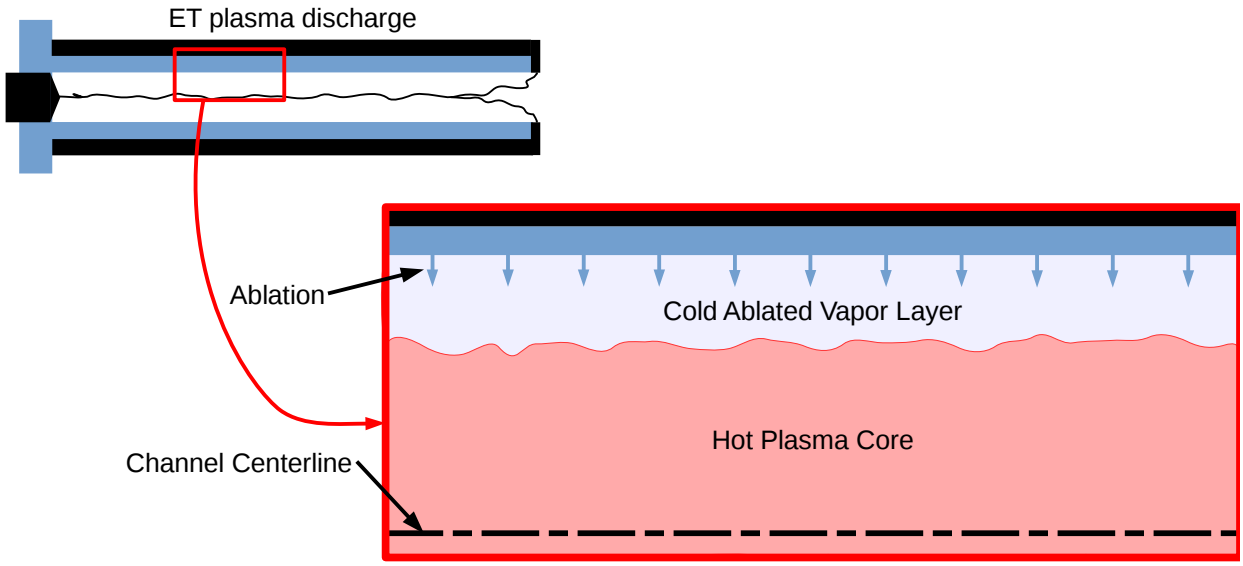

Figure 2.1: The ET plasma channel divided into two zones: a hot plasma core, and a vapor layer formed from ablating material.

Ruchti and Niemeyer [31] developed scaling laws for the arc stagnation pressure, electric field strength, and mass ablation rates in capillary plasma discharges. Their theoretical description was based on an isothermal arc. For a liner material of PTFE, they estimated the arc temperature to be 19000 ± 2000 K and a vapor layer temperature of 3400 ± 200 K. One of the key parameters in the development of their theory was the vapor transparency factor which represents the ratio of the rate of energy radiated to the ablating surface to the ohmic heating rate in the discharge. For a PTFE liner material, they estimated the value of the vapor transparency factor to be 0.32 ± 0.03.

Kovitya and Lowke [30] advanced the theory of these capillary discharges by developing a 1D, steady-state model of these devices. These authors also developed a transparency factor to account for the vapor layer in the two-zone structure of the discharge. Kovitya and Lowke employed two different radiation approximations in their 1D model: the net emission

approximation and the black-body approximation. Their results suggested that the net emission approximation was well-suited for discharge currents < 4 kA. The black-body approximation was more appropriate for discharge currents > 4 kA and plasma pressures > 50 atm (> 5 MPa). It is interesting to note the relationship between the results obtained by Kovitya and Lowke in 1984 [30] and the results obtained by Pekker in 2009 [38]. Pekker used a commercially available database in order to estimate the radiation emission from a plasma discharge in a slab capillary. He also noted a similar transition between "super-high pressure" (SHP) plasma discharges and "moderately high pressure" (MHP) plasma discharges. In SHP plasma discharges, the radiation from the plasma approaches the black-body approximation. For MHP plasma discharges, the radiation mean free path is larger than the domain length scale and more sophisticated methods are required for the correct determination of the plasma radiation heat transfer. Pekker was able to estimate that the transition between these two regimes occurs between ~ 0.2 MPa and ~ 5 MPa. This transition region is close to the transition noted by Kovitya and Lowke.

2.1.2 Time-Dependent Modeling

Zero-dimensional, time-dependent models emerged for ET plasma discharges in the 1990s [69, 70]. Gilligan and Mohanti introduced the ZEUS code in 1990 [69]. These authors compared their simulation results for steady-state operation with the work of Ruchti and Niemeyer [31]. Gilligan and Mohanti compared time-dependent simulation results with pulsed experiments being performed by Bourham et al. using the SIRENS experimental facility [71]. SIRENS

was designed as a high-heat flux experiment after the same principles as an electrothermal mass accelerator. Gilligan and Mohanti incorporated a correction factor into their zero-dimensional model similar to the transparency factors employed by Kovitya and Lowke [30] and Ruchti and Niemeyer [31]. Gilligan and Mohanti called their correction factor the vapor transmission factor, and it represented the ratio of the ablating heat flux from the plasma to black-body radiation flux from the plasma. Gilligan and Mohanti estimated that the vapor transmission factor was approximately 10%.

One-dimensional models quickly emerged [44, 45, 72]. Powell and Zielinski [44, 72] presented a 1D, time-dependent model of an ET discharge. They modeled the ablating heat flux as pure black-body radiation from the plasma. The amount of mass ablated per time per volume was modeled by the equation:

$$\dot{\rho}_a = \rho \frac{\sigma_{SB} T^4 (2/R)}{P + \rho U} \tag{2.1}$$

where $\dot{\rho}_a$ is the mass ablation rate, ρ is the plasma density, σ_{SB} is the Stefan-Boltzmann constant, T is the plasma temperature, R is the capillary radius, P is the plasma pressure, and U is the plasma internal energy. Naturally, the factor $(2/R)$ in the numerator in Eq. (2.1) converts the black-body heat flux, $\sigma_{SB} T^4$, into units of energy radiated per volume per time. The denominator of Eq. (2.1) requires that the ablating material enter the domain with the same stagnation enthalpy as the bulk plasma. Hurley et al. [45], who also developed a 1D, time-dependent model, used a similar approach but recast the ablation term to use an

adaptive vapor transmission factor, f. Hurley et al. presented the following form for the ablation rate.

$$\dot{\rho}_a = \frac{f\sigma_{SB}T^4(2/R)}{H_{sub}} \tag{2.2}$$

where H_{sub} is the energy per mass required to sublimate the ablating material, and:

$$f = \frac{\rho H_{sub}}{P + \rho U + \rho H_{sub}} \tag{2.3}$$

The resulting form for the ablation rate is therefore given by:

$$\dot{\rho}_a = \rho\frac{\sigma_{SB}T^4(2/R)}{P + \rho U + \rho H_{sub}} \tag{2.4}$$

A comparison of Equations (2.1) and (2.4) reveals that Hurley et al. in Eq. (2.4) accounted for the sublimation energy of the material while Powell and Zielinski in Eq. (2.1) did not. Simulation results from the model of Powell and Zielinski lacked agreement with experimental measurements while the model of Hurley et al. enjoyed favorable agreement with experiment. Powell and Zielinski speculated that their assumption of a negligible vapor layer thickness could have caused their results to differ from experiment. They also point out that the development of two-zone models, where the effects of the vapor layer are included, require assumptions that are "difficult to justify" [44].

The adaptive form of the vapor transmission factor used by Hurley et al. was later questioned in the work of Zaghloul [24]. Zaghloul's analysis involved the measurement of the

electrical conductivity during a pulsed ET plasma discharge generated using the PIPE device [73]. Zaghloul utilized the measured electrical conductivity (and resultant ohmic heating) as the input to a 1D, time-dependent simulation model for ET plasma discharges [24]. Using the measured electrical conductivity in the simulation model improved its accuracy. Using this model, Zaghloul compared the use of the ablation model presented by Hurley et al. [45] with an ablation model that used an average constant value for the vapor transmission factor. The average constant value was tuned in order to match simulation results for the total ablated mass with measured ablated mass. Zaghloul argued that the use of an average constant vapor transmission factor produced better agreement with experimental results and more appropriately captured the underlying physics at play [24].

A semi-2D simulation model for ET plasma discharges has been proposed by Ngo et al. [74]. This semi-2D model relied on a 1D solution for the plasma bulk properties but also included a radial energy equation to estimate the radial gradients that developed inside the ET plasma discharge. Ngo's model incorporated the radiation heat transfer using the diffusion approximation that was based on relations given by Zel'dovich and Raizer [75]. Ngo's work was later advanced by Winfrey [6] who added conduction heat transfer to the capillary wall.

The models discussed in this section have treated the ET plasma as a homogeneous fluid with all species in local thermodynamic equilibrium (LTE). The plasma number densities are typically evaluated using some form of the Saha equation [76]. The Saha equation relates the electron density with the plasma temperature for a plasma in LTE. For a singly ionized

plasma species, n_i, the Saha equation is given by [1]:

$$\frac{n_e n_i}{n_n} = 2\frac{g_i}{g_n}\left(\frac{2\pi m_e k_B T}{h^2}\right)^{3/2} e^{-\Delta E/k_B T} \tag{2.5}$$

where n_e is the electron number density, n_i is the ion number density, n_n is the neutral number density, g_i is the degeneracy of the ground energy level of the ion species, g_n is the degeneracy of the ground energy level of the neutral species, m_e is the electron mass, k_B is Boltzmann's constant, T is the plasma temperature, h is Planck's constant, and ΔE is the ionization energy for the ion species. The Saha equation can also be applied to multiply ionized plasmas.

The plasma models discussed in this section incorporate the governing equations of the conservation of mass, momentum, and internal energy. A wealth of research has been conducted in order to determine the best means by which to include the effects of the vapor layer in the simulation of these devices. The need for accurate and realistic approximations for the effects of the vapor layer in these devices has led many researchers to study the plasma-wall interaction in significant detail.

2.2 The Plasma-Wall Boundary Layer

2.2.1 One-dimensional Analyses

Gilligan et al. [77] and Hahn [78] developed a 1D model that simulated the radiation transport through the boundary layer that develops at an ablating surface experiencing intense incident heat flux. These authors used a multi-group, flux-limited diffusion model in order to capture the radiation heat transfer. Using this model, the authors were able to estimate the dependence of the vapor transmission factor on the radiation heat fluence incident on ablating surfaces of iron, carbon, and copper. These authors observed that the vapor layer could block up to 90% or higher of the radiation fluence. This corresponds to a vapor transmission factor of 10%.

Hahn and Gilligan [79] used the same flux-limited diffusion model to analyze radiation transport through the plasma boundary layer that develops in devices similar to the ET plasma discharge. Based on the anisotropy of the radiation field near the plasma-wall interface (since the wall itself does not provide photons), these authors used a boundary condition for this interface that is given by:

$$S_g = \frac{c}{2} U_g \tag{2.6}$$

where S_g is the radiation flux for frequency group g at the plasma-wall interface, c is the speed of light, and U_g is the radiant energy of group g. Based on a comparison of their model with an analytical solution, Hahn and Gilligan also established an appropriate flux-limiter

for the types of plasmas generated inside ET plasma discharges. The flux limit is the same as that given in Eq. (2.6).

2.2.2 Two-dimensional Analyses

Two-dimensional, steady-state investigations of the plasma boundary layer that develops at an ablating surface have been performed by Eapen [80] and Orton [81]. These authors simulated hot plasma flow over a flat plate and observed the effects of ablation on the boundary layer. Eapen established the foundations for hydrodynamic analysis of the plasma boundary layer flow. Orton extended Eapen's work to include radiation transport and turbulence. Orton was only able to model a small range of ablation cases due the onset of flow separation at higher ablation rates. Orton and Eapen found that ablation had the effect of widening the plasma boundary layer and decreasing thermal gradients at the wall and thus decreasing the heat flux to the wall. Eapen referred to this effect as "hydrodynamic thermal shielding." These studies coupled the hydrodynamics with the heat transfer and advanced the understanding of the relationship between ablation and heat flux inside ET plasma discharges.

2.2.3 Kinetic Ablation Models

Keidar et al. [33, 37] developed a 1D, time-dependent model of an ET plasma discharge for investigating their use as plasma thrusters and ETC guns. The authors sought to capture the ablation phenomenon by incorporating an electrostatic sheath, a kinetic non-equilibrium

Knudsen layer, and a non-equilibrium, hydrodynamic layer between the ablating surface and the plasma bulk. Using this approach, the authors were able to estimate the material velocity perpendicular to the ablating surface and avoid the use of a vapor transmission factor. However, the kinetic ablation model used by Keidar et al. [82, 83] has been contested by Zaghloul who offers a revised kinetic model for the ablation [84]. The kinetic ablation model offered by Zaghloul has been revised further to include a pressure dependence term [85]. This pressure-dependent kinetic ablation model has been implemented in a 2D, steady-state model of an ET plasma discharge [86]. An in-depth investigation of these kinetic ablation models is beyond the scope of this study, but may be an important consideration in future works.

2.3 State of the Art

2.3.1 Improved Estimations of Plasma Radiation

Recently, Zaghloul applied detailed photon absorption calculations for a Lexan plasma to a 1D, time-dependent simulation model of an ET plasma discharge with Lexan used as the liner material [25, 87]. Using this approach, Zaghloul estimated a grey-body factor to adjust the radiation heat flux coming from the ET plasma. Zaghloul considered that the detailed determination of the grey-body factor also accounted for the vapor shield layer and obviated the need for a tunable vapor transmission factor. Instead, Zaghloul tuned the heat

of ablation for the Lexan liner material in order to match simulation results with experiment. Since Zaghloul was limited to a 1D model of an ET plasma discharge, he was not able to take into account the radial gradients that develop during the discharge.

L. Pekker and O. Pekker developed a model for a slab capillary ET plasma discharge in order to study the use of these devices as plasma thrusters [38,39]. The model these authors developed was 0D and time dependent. These authors used PrismSPECT, a commercially available software package, in order to compute the radiation spectrum for the plasma. As explained by L. Pekker [38], PrismSPECT calculates the plasma composition from the number density, plasma temperature, and element composition ratios. The radiation spectrum is then computed from the plasma composition and includes the effects of free-bound and bound-bound electron transitions. By integrating over the radiation spectrum, L. Pekker was able to approximate the total radiation coming from the plasma. Using this approach, the authors were able to make a variety of observations concerning the plasma. For example, the authors identified two different plasma regimes, super-high pressure (SHP) and moderately-high pressure (MHP) that can exist in these types of devices. In the SHP regime, plasma pressures are greater than 1 MPa, and the plasma radiation spectrum tends towards a black-body spectrum. However, in the MHP regime, plasma pressures are less than 1 MPa, and the plasma radiation spectrum is far from a black-body spectrum. While several interesting details about the plasmas that can develop inside ET plasma discharges were observed in the work of these authors, their model was still 0D and therefore unable to capture multidimensional effects that arise especially near the ablating surface.

2.3.2 The ETFLOW Code

The ETFLOW simulation code [6] has become a standard as an ET plasma discharge simulation tool [26, 55–58, 66, 67, 88–91]. ETFLOW includes the ability to switch between ideal and non-ideal electrical conductivity models. This code is also equipped with a materials library which enables users to simulate several different materials in an ET discharge. The output of the code is written in a format that can be easily read by Microsoft Excel and processed easily by users familiar with this software. ETFLOW can be used to simulate the development of the ET plasma in an acceleration barrel and models the acceleration of a pellet in the barrel. ETFLOW also includes a module to compute the radial gradients in ET plasma launchers using a semi-2D approach.

The ETFLOW code has been used to show that ET plasmas tend toward weak non-ideality at higher discharge current pulses ($\gtrsim 30-40$ kA) [26]. ETFLOW has also been used to show the increasing importance of the vapor shield layer as discharge current increases [88]. A thorough computational investigation of the use of an ET plasma discharge as a pellet injector for a magnetic confinement fusion reactor has been performed using ETFLOW [57].

ETFLOW has driven much improvement and development in the knowledge and understanding of ET plasma discharges. However, the 1D nature of this simulation code prevents it from capturing the radial gradients that may prove to play an important role in the operation of these devices. For example, the treatment of the ablation as a volumetric source term in ETFLOW ignores the development of a vapor shield layer caused by ablating particles

separating the plasma core from the ablating surface. In order to capture these important details, a fully-2D model and simulation code must be employed.

2.3.3 Recent Experimental Investigations

Echols [27, 68] investigated the surface erosion of a tungsten substrate exposed to an ET plasma discharge. The tungsten was part of the source liner material inside the discharge. As a result, the particle flux to the tungsten was at a low incident angle. Echols used Scanning Electron Microscopy (SEM) and Energy Dispersive Spectroscopy (EDS) to investigate the eroded tungsten surface. He was able to estimate the melt layer thickness and also observed the formation of voids within the tungsten material.

Hamer [28] performed spectroscopic measurements on ET plasma discharges generated with the PIPE system. His diagnostics focused on the plasma plume that exits the source during the discharge. Hamer's experiments used Lexan as the ablating liner material. His measurements confirmed the assumption of full dissociation of ablated material, which is typically made in simulation models of ET plasma discharges. Hamer also used high-speed videography on the plasma plume and estimated bulk plasma velocity exiting the ET plasma source.

New ET plasma systems are currently under construction at Oak Ridge National Laboratory (ORNL) and the University of Florida. These ET plasma systems will utilize state-

of-the-art diagnostic systems. This advancement in diagnostics will significantly aid the simulation and modeling efforts for ET plasma discharges.

Chapter 3

Two-Dimensional Model Development

The simulation capabilities of pulsed ET plasma discharges have been limited to 1D and semi-2D models. As discussed previously, the 1D approximation of these devices leaves out details of the ablating surface effects that can play an important role in the correct determination of the heat flux from the plasma core to the ablating surface. In addition, simulations of ET plasmas have focused on the treatment of the plasma as a homogeneous fluid. This approach ignores some of the effects arising from inter-species interactions like elastic collisions.

In order to advance previous studies and gain more insight into the physics occurring in ET plasma discharges, the Three-Fluid, 2D ET Plasma Flow Simulator (THOR) has been developed. THOR simulates the time evolution of the electron, ion, and neutral species in the partially ionized ET plasma. The governing equations of the THOR code are discretized on

a 2D, axisymmetric, structured grid. THOR takes advantage of modern high performance computing platforms and is parallelized using both open MPI (distributed memory) and OpenMP® (shared memory). For MPI, the computational domain is decomposed into smaller segments each commanded by an MPI process. Each MPI process is then executed using multiple OpenMP® threads.

The equations used in this work are derived from the Boltzmann equation. Meier and Shumlak [17] present an excellent derivation of a three-component plasma model. Their equations for the ion and neutral species are presented here with only a few alterations and exhibit the main features of the Euler gas-dynamic equations. The electron governing equations are based on the drift-diffusion approximation. After presentation of the model's governing equations, code verification and validation are discussed.

Nomenclature

Species Specific Quantities:

e (subscript)	electron species
i (subscript)	ion species
n (subscript)	neutral species
m	particle mass
n	number density
$\mathbf{u}$	directed velocity
T	temperature
P	pressure
ε	total energy
C_v	specific heat at constant volume
$\mathbf{R}$	collisional drag force on the species due to elastic collisions with other species
Q	energy transfer to the species due to elastic collisions with other species
v_{th}	thermal velocity based on a Maxwellian distribution

$\mathbf{q}$	heat flow vector

Constants:

k_B	Boltzmann's constant
e	elementary charge
σ_{SB}	Stefan-Boltzmann constant
ε_0	permittivity of free space
h	Planck's constant
k_e	Coulomb's constant

Other Quantities:

Γ_{ion}	ionization rate
Γ_{rec}	recombination rate
$\mathbf{E}$	electric field
$\bar{\nu}_{ei}$	electron-ion collision frequency
$\bar{\nu}_{en}$	electron-neutral collision frequency
$\bar{\nu}_{eh} = \bar{\nu}_{ei} + \bar{\nu}_{en}$	electron-heavy particle collision frequency
$\mathbf{J}$	current density
μ_e	electron mobility
$\bar{Q}_{en}$	electron-neutral averaged momentum transfer cross-section
$\bar{Q}_{ei}$	electron-ion averaged momentum transfer cross-section
σ	plasma electrical conductivity
σ_{en}	electrical conductivity due to electron-neutral collisions
σ_{ei}	electrical conductivity due to electron-ion collisions
q''_{rad}	radiation heat flux incident on ablating surface
q'''_{rad}	radiation heat loss per volume due to radiation
Φ_{abl}	flux of ablated neutral particles at the ablating surface
H_{sub}	sublimation energy of ablating material
l_{rad}	radiation mean free path
Z	charge state

3.1 Governing Equations

3.1.1 Electrons

The electrons are simulated using the drift-diffusion approximation. The continuity equation used for the electrons is:

$$\frac{\partial n_e}{\partial t} + \nabla \cdot (n_e \mathbf{u}_e) = \Gamma_{ion} - \Gamma_{rec} \tag{3.1}$$

where n_e is the electron number density, $\mathbf{u}_e$ is the electron directed velocity, Γ_{ion} is the ionization rate, and Γ_{rec} is the recombination rate. The first term in Eq. (3.1) represents the time rate of change of the electron number density, the second term represents the convective flow of electrons in and out of a particular computational cell, the third term represents the addition of electrons through ionization, and the fourth term represents the loss of electrons due to recombination. The electron momentum equation, by the drift-diffusion approximation, reduces to an equation of state for the electron velocity.

$$\mathbf{u}_e = -\frac{e\mathbf{E}}{m_e \bar{\nu}_{eh}} - \frac{\nabla P_e}{n_e m_e \bar{\nu}_{eh}} \tag{3.2}$$

where e is the elementary charge, m_e is the electron mass, $\mathbf{E}$ is the electric field, $\bar{\nu}_{eh} = \bar{\nu}_{ei} + \bar{\nu}_{en}$ is the momentum transfer collision frequency for electron collisions with heavy particles, and P_e is the electron pressure. The first term on the right hand side of Eq. (3.2) is the drift component of the electron velocity due to the electric field, and the second term on the right hand side is the diffusion component of the electron velocity. The electron energy equation

is written in terms of internal energy, and is given by:

$$\frac{\partial}{\partial t}(n_e C_{v,e} T_e) + \nabla \cdot (\mathbf{u}_e n_e C_{v,e} T_e) = -\nabla \cdot \mathbf{q}_e + \frac{1}{\sigma} j^2 + Q_e \tag{3.3}$$

where T_e is the electron temperature, $C_{v,e}$ is the specific heat at constant volume of the electron fluid, σ is the plasma electrical conductivity, j is the local current density, Q_e is the heat transferred to the electrons due to elastic collisions with other species. On the right hand side of Eq. (3.3) the first term is the energy transferred by conduction heat transfer, the second term is the joule heating of the electron species, the third term is the exchange of energy with other species due to elastic collisions.

The electron fluid is assumed to behave as a perfect gas, and thus $P_e = n_e k_B T_e$. The electrons are always monatomic with $\gamma = 5/3$, and therefore $C_{v,e} = k_B/(\gamma - 1) = (3/2)k_B$. The electron governing equations are evolved using an alternating direction implicit (ADI) method. This is similar to the approach used by Bowkouski et al. [22].

3.1.2 Ions

The continuity equation used for the ion species is similar to Eq. (3.1) and is given by:

$$\frac{\partial n_i}{\partial t} + \nabla \cdot (n_i \mathbf{u}_i) = \Gamma_{ion} - \Gamma_{rec} \tag{3.4}$$

where n_i is the ion number density, and $\mathbf{u}_i$ is the ion directed velocity. The interpretations of the terms in Eq. (3.4) are similar to the interpretation for terms in Eq. (3.1).

The momentum equation for the ion species is given by:

$$\frac{\partial}{\partial t}(m_i n_i \mathbf{u}_i) + \nabla \cdot (m_i n_i \mathbf{u}_i \mathbf{u}_i) = -\nabla P_i + q_i n_i \mathbf{E} + \mathbf{R}_i + \Gamma_{ion} m_i \mathbf{u}_n - \Gamma_{rec} m_i \mathbf{u}_i \tag{3.5}$$

where m_i is the ion mass, P_i is the ion pressure, q_i is the ion charge, $\mathbf{E}$ is the electric field, $\mathbf{u}_n$ is the directed velocity of the neutral species, and $\mathbf{R}_i$ is the collisional drag force acting on the ion species due to elastic collisions with other species. The first term in Eq. (3.5) represents the time rate of change in ion momentum, the second term represents the convective flow of ion momentum in and out of a computational cell, the third represents the pressure force on the ion species, the fourth term represents the force on the ion species due to the electric field, the fifth term accounts for collisional drag forces induced on the ion species due to elastic collisions with other species, and the sixth and seventh terms represent the exchange of momentum between the neutral and ion species due to ionization and recombination reactions.

The energy equation used for the ion species is given in terms of total energy.

$$\frac{\partial \varepsilon_i}{\partial t} + \nabla \cdot (\varepsilon_i \mathbf{u}_i) = -\nabla \cdot \mathbf{q}_i - q'''_{rad,i} - \nabla \cdot (\mathbf{u}_i P_i) + \mathbf{u}_i \cdot (q_i n_i \mathbf{E} + \mathbf{R}_i) + Q_i + \Gamma_{ion} \frac{\varepsilon_n}{n_n} - \Gamma_{rec} \frac{\varepsilon_i}{n_i} \tag{3.6}$$

where $\varepsilon_i = n_i C_{v,i} T_i + m_i n_i u_i^2/2$ is the total energy of the ion species, $\mathbf{q}_i$ is the conduction heat flow vector for the ion species, $q'''_{rad,i}$ is the radiation loss term for the ion species, Q_i is the internal energy transferred to the ion species due to inter-species elastic collisions, $C_{v,i}$ is the ion specific heat, and T_i is the ion temperature. On the right hand side of Eq. (3.6), the first term represents the heat conduction for the ion species, the second term represents the heat loss from the ions due to radiation heat transfer, the third term is the work done on the ions species due to the pressure, the fourth term is the work done on the ion species by the electric field and the elastic collision forces, the fifth term is the transfer of energy to the ion species due to inter-species elastic collisions, and the sixth and seventh terms represent the exchange of total energy between the ion and neutral species due to ionization and recombination reactions.

The ion species is assumed to behave as a perfect gas with:

$$P_i = n_i k_B T_i \tag{3.7}$$

where k_B is Boltzmann's constant. The ion species specific heat is constant and given by:

$$C_{v,i} = k_B/(\gamma - 1) \tag{3.8}$$

where γ is the ratio of specific heats. The ions that are present in an ET plasma discharge are assumed to be fully dissociated, therefore $\gamma = 5/3$. It is important to note that the specific heat as given by Eq. (3.8) has units of J/K. Therefore, in this presentation, the total

energy of the ions species is given by:

$$\varepsilon_i = n_i C_{v,i} T_i + m_i n_i u_i^2/2 \tag{3.9}$$

where no mass density is required in the first term of on the right hand side of Eq. (3.9). In the implementation of the governing equations for the ions, the convective flux terms in Eqs.(3.4)–(3.6) are computed according to a first-order upwind scheme as presented by Tatsumi et al. [92].

3.1.3 Neutrals

The continuity equation for the neutral species is given by:

$$\frac{\partial n_n}{\partial t} + \nabla \cdot (n_n \mathbf{u}_n) = \Gamma_{rec} - \Gamma_{ion} \tag{3.10}$$

This equation is very similar to both Eq. (3.1) and Eq. (3.4) with the right hand side of Eq. (3.10) being opposite from Eq. (3.1) and Eq. (3.4).

The momentum equation for the neutral species is given by:

$$\frac{\partial}{\partial t}(m_n n_n \mathbf{u}_n) + \nabla \cdot (m_n n_n \mathbf{u}_n \mathbf{u}_n) = -\nabla P_n + \mathbf{R}_n - \Gamma_{ion} m_n \mathbf{u}_n + \Gamma_{rec} m_n \mathbf{u}_i \tag{3.11}$$

The terms in Eq. (3.11) have very similar interpretations as those in Eq. (3.5). The differences of note include the disappearance of the electric field term in Eq. (3.11) due to zero charge on a neutral particle.

The energy equation for the neutral species is given in terms of total energy.

$$\frac{\partial \varepsilon_n}{\partial t} + \nabla \cdot (\varepsilon_n \mathbf{u}_n) = -\nabla \cdot \mathbf{q}_n - q'''_{rad,n} + \nabla \cdot (\mathbf{u}_n P_n) + \mathbf{u}_n \cdot \mathbf{R}_n + Q_n - \Gamma_{ion} \frac{\varepsilon_n}{n_n} + \Gamma_{rec} \frac{\varepsilon_i}{n_i} \quad (3.12)$$

The terms in Eq. (3.12) include very similar terms to those included in Eq. (3.6). The interpretations of each term is also similar.

As in the case of the ions, the neutral species is assumed to behave as a perfect gas.

$$P_n = n_n k_B T_n \quad (3.13)$$

$$C_{v,n} = k_B/(\gamma - 1) \quad (3.14)$$

The neutral species is assumed to be fully dissociated and γ is taken to be $\gamma = 5/3$. The total energy for the neutral species is given by:

$$\varepsilon_n = n_n C_{v,n} T_n + m_n n_n u_n^2/2 \quad (3.15)$$

where $C_{v,n}$ is in units of [J/K]. Similar to the ion species, the neutral species convective flux terms in Eqs. (3.10)–(3.12) are computed using to a first-order upwind scheme [92].

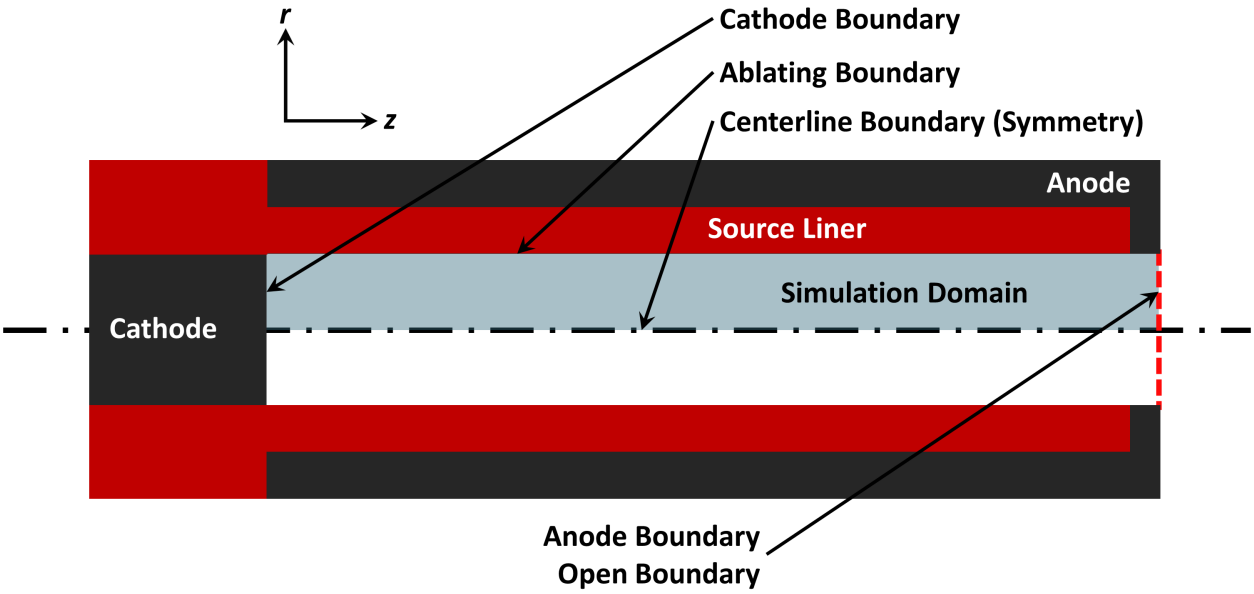

Figure 3.1: A schematic of an ET plasma discharge with the simulation domain of used by the THOR model and code illustrated. The different boundaries of the domain are named and located.

3.1.4 Boundary Conditions

The THOR model includes a set of boundary conditions for the electron, ion, and neutral species. Figure 3.1 illustrates the simulation domain with boundaries specified. The details of the species boundary conditions are shown in Tables 3.2, 3.3, and 3.4. In these tables, the normal vector, $\hat{\mathbf{n}}$, points into the simulation domain by convention.

The electron boundary conditions in Table 3.2 show that the cathode and ablating surface boundaries are treated as adiabatic boundaries in the electron temperature. This approach is used because the electron temperature at the boundary is not always known, and estimates of this temperature would only be available by rough approximations. The electron flux at

Table 3.2: Electron boundary conditions used in the THOR simulation code.

Cathode Boundary	Ablating Boundary	Anode/Open Boundary
$\nabla n_e \cdot \hat{\mathbf{n}} = 0$	$\nabla n_e \cdot \hat{\mathbf{n}} = 0$	$\nabla n_e \cdot \hat{\mathbf{n}} = 0$
$\nabla P_e \cdot \hat{\mathbf{n}} = 0$	$\nabla P_e \cdot \hat{\mathbf{n}} = 0$	$\partial^2 T_e / \partial z^2 = 0$
$\nabla T_e \cdot \hat{\mathbf{n}} = 0$	$\nabla T_e \cdot \hat{\mathbf{n}} = 0$	$P_e = n_e k_B T_e \vert_{boundary}$
$\Phi_e = -n_e \mu_e \mathbf{E}$	$\Phi_e = 0$	$\Phi_e = \frac{1}{A} \int \Phi_e \vert_{cathode} dA - \frac{\nabla P_e}{m_e \bar{\nu}_{eh}}$
Φ_e: Electron flux		

the cathode is directed out of the domain and depends on the electron density, electric field strength, and the electron mobility — $\mu_e = e/(m_e \bar{\nu}_{eh})$. This flux is matched at the anode boundary as electrons enter the domain. The anode electron flux is adjusted so that the electron diffusion out of the domain occurs. No electron flux is simulated across the ablating boundary. This boundary is assumed to have zero normal electric field component.

The ion and neutral species have similar sets of boundary conditions. This is due to the similarity in the sets of governing equations used for the ion and neutral species. The anode/open boundary conditions for these two species are the same and summarized in Table 3.3. These boundary conditions utilize an extrapolation technique which estimates the required exterior conditions based on interior conditions in order to formulate the open boundary. A more detailed discussion on open boundary conditions for fluid simulations is offered by Laney [93].

For the cathode boundary, the neutral and ion boundary conditions are again very similar. The ion and neutral densities, pressures, and temperatures are treated as adiabatic boundaries at the cathode. In addition, the ion and neutral velocities are fixed at zero at

Table 3.3: Anode (Open) boundary conditions for ion and neutral species in the THOR simulation code.

Subsonic Inflow	Subsonic Outflow	Supersonic Outflow
$M_{exit} < 1,\ u_{\alpha,z} < 0$	$M_{exit} < 1,\ u_{\alpha,z} \geq 0$	$M_{exit} \geq 1,\ u_{\alpha,z} > 0$
$P_\alpha = P_{\alpha,init}$	$P_\alpha = P_{\alpha,init}$	$\partial^2 n_\alpha/\partial z^2 = 0$
$\partial^2 n_\alpha/\partial z^2 = 0$	$\partial^2 \mathbf{u}_\alpha/\partial z^2 = 0$	$\partial^2(m_\alpha n_\alpha \mathbf{u}_\alpha)/\partial z^2 = 0$
$T_\alpha = \frac{P_\alpha}{n_\alpha k_B}\Big\vert_{boundary}$	$\partial^2 T_\alpha/\partial z^2 = 0$	$\partial^2 \varepsilon_\alpha/\partial z^2 = 0$
$\partial^2(m_\alpha n_\alpha \mathbf{u}_\alpha)/\partial z^2 = 0$	$n_\alpha = \frac{P_\alpha}{k_B T_\alpha}\Big\vert_{boundary}$	$P_\alpha = n_\alpha k_B T_\alpha\vert_{boundary}$
$M_{exit} = \vert u_{\alpha,z}\vert/c_s$: Exit Mach number c_s: Local sound speed α: i (ions) or n (neutrals)		

this boundary. It is assumed that the ion flux at the cathode is negligible due to its large size compared with the electrons.

The ablating surface boundary involves different boundary conditions for the ion and neutral species. These boundary conditions are specified in Table 3.4. Again, zero ion flux into or out of the ablating surface is assumed. The ablation process occurs through the deposition of a radiation heat flux, q''_{rad}, on the ablating surface. The ablating process is assumed to deliver only neutral species to the plasma flow.

Table 3.4: Ion and neutral boundary conditions at the ablating surface.

Ablating Surface Boundary Conditions	
Ions	Neutrals
$\nabla n_i \cdot \hat{\mathbf{n}} = 0$	$n_n = P_n/k_B T_{boil}$
$\nabla P_i \cdot \hat{\mathbf{n}} = 0$	$\nabla P_n \cdot \hat{\mathbf{n}} = 0$
$\nabla T_i \cdot \hat{\mathbf{n}} = 0$	$\nabla T_n \cdot \hat{\mathbf{n}} = 0$
$u_{i,r} = 0$	$u_{n,r} = -q''_{rad}/(H_{sub} n_n)$
$u_{i,z} = 0$	$u_{n,z} = 0$
q''_{rad}: Ablating heat flux H_{sub}: Liner sublimation energy	

3.1.5 Collisions and Reactions

Collision Frequencies

The effects of elastic collisions between species are characterized by the elastic collision frequencies between species. These collision frequencies depend on the relative thermal speeds of the colliding particles, particle density, and cross-section for particle collisions. For electron-neutral collisions, the collision frequency can be approximated by:

$$\bar{\nu}_{en} = n_n v_{avg,e} \bar{Q}_{en} \tag{3.16}$$

where n_n is the neutral number density, $v_{avg,e} = \sqrt{8 k_B T_e/(\pi m_e)}$ is the Maxwellian averaged thermal velocity of the electrons, and $\bar{Q}_{en}$ is the cross-section for electron-neutral collisions. The cross-section for electron-neutral collisions can be approximated using a hard-sphere approximation based on the neutral particle's atomic radius. For electron-ion collisions, the

collision frequency can be approximated similarly as:

$$\bar{\nu}_{ei} = n_i v_{avg,e} \bar{Q}_{ei} \tag{3.17}$$

where n_i is the ion number density, and $\bar{Q}_{ei}$ is the cross section for electron-ion collisions. Since electron-ion collisions involve coulomb interactions, the estimation of the cross-section for these collisions is quite complex. Currently, the THOR code utilizes the approximation for the electron-ion collision cross-section recommended by Zaghloul [5]. Zaghloul's approximation to the electron-ion collision cross-section is theoretically accurate for ideal and non-ideal plasmas. The electron-heavy particle collision frequency is given by:

$$\bar{\nu}_{eh} = \bar{\nu}_{en} + \bar{\nu}_{ei} \tag{3.18}$$

For elastic collisions between ion and neutral species, the collision frequency is approximated by:

$$\bar{\nu}_{in} = n_n \bar{v}_{th,in} \bar{Q}_{in} \tag{3.19}$$

where n_n is the neutral number density, $\bar{v}_{th,in}$ is the relative thermal speed of colliding particles, and $\bar{Q}_{in}$ is the collision cross-section. The collision cross-section can be estimated using a hard-sphere approximation since no Coulomb interactions are involved. The relative

thermal speed is approximated by:

$$\bar{v}_{th,in} = \sqrt{\frac{8k_B T_{avg}}{\pi \bar{m}}} \tag{3.20}$$

where $T_{avg} = (T_i + T_n)/2$ is the averaged species temperature, and $\bar{m} = m_i m_n/(m_i + m_n)$ is the particle reduced mass [7].

For intra-species collisions between neutral particles, coulomb collisions are not involved. Therefore, the neutral-neutral collision frequency is given by [7]:

$$\bar{\nu}_{nn} = \sqrt{2} n_n v_{avg,n} \pi d_n^2 \tag{3.21}$$

where $v_{avg,n} = \sqrt{8k_B T_n/(\pi m_n)}$ is the average thermal velocity of the neutral particles, and d_n is the atomic diameter of a neutral particle. Intra-species collisions between ions are more complicated due to the coulombic interactions involved.

In order to estimate the ion thermal conductivity, the total ion-ion collision frequency is needed. For the ion-ion collision frequency, coulomb interactions must be considered. To estimate this collision frequency, the ion-ion thermal relaxation time, τ_ε^{ii}, is considered [94].

$$\tau_\varepsilon^{ii} = \frac{(2\pi)^{1/2} 6\pi \varepsilon_0^2 m_i^{1/2} (k_B T_i)^{3/2}}{Z^4 n_i e^4 \ln \Lambda} \tag{3.22}$$

where ε_0 is the permittivity of free space, Z is the charge state of the plasma, and $\ln \Lambda$ is the Coulomb logarithm. The Coulomb logarithm represents the energy-averaged term in the

expression for the averaged electron-ion collision cross-section [1,5]. Different formulations of the Coulomb logarithm have been offered by Spitzer and Harm [10], Zollweg and Liebermann [11], and Zaghloul et al. [5]. Estimating the ion-ion collision frequency to be the inverse of τ_{ε}^{ii}, it can be shown that the average total ion-ion collision frequency is given by:

$$\bar{\nu}_{ii} = Z^2 n_i \sqrt{\frac{8kT_i}{\pi m_i}} \bar{Q}_{ei} = Z^2 n_i v_{avg,i} \bar{Q}_{ei} \tag{3.23}$$

Equation (3.23) has the expected form for a collision frequency. It includes non-ideal plasma effects through the inclusion of $\bar{Q}_{ei}$. The scaling with the square of the charge state is due to the increased importance of coulomb interactions as the charge state increases.

Collision Terms

The collision terms account for the effects of elastic collisions between species. Elastic collisions do not involve a change in the nature of the colliding particles, but do transfer momentum (via a friction force) and internal energy between species. The friction force acting on species k due to elastic collisions with species α is given by [8]:

$$\mathbf{R}_k^{k\alpha} = m_k n_k \bar{\nu}_{k\alpha} \left(\mathbf{u}_\alpha - \mathbf{u}_k \right) \tag{3.24}$$

where m is the particle mass, n is the species number density, $\mathbf{u}$ is the species directed velocity, and $\bar{\nu}_{k\alpha}$ represents the collision frequency between particles of species k and species α. Since the drag forces between two different species must be equal and opposite, the

following requirement must be satisfied.

$$\bar{\nu}_{\alpha k} = \frac{m_k n_k}{m_\alpha n_\alpha} \bar{\nu}_{k\alpha} \tag{3.25}$$

Equations (3.24) and (3.25) yield the following forms for the collision drag forces acting on the electron, ion, and neutral species.

$$\mathbf{R}_e = m_e n_e \bar{\nu}_{ei}(\mathbf{u}_i - \mathbf{u}_e) + m_e n_e \bar{\nu}_{en}(\mathbf{u}_n - \mathbf{u}_e) \tag{3.26}$$

$$\mathbf{R}_i = m_e n_e \bar{\nu}_{ei}(\mathbf{u}_e - \mathbf{u}_i) + m_i n_i \bar{\nu}_{in}(\mathbf{u}_n - \mathbf{u}_i) \tag{3.27}$$

$$\mathbf{R}_n = m_e n_e \bar{\nu}_{en}(\mathbf{u}_e - \mathbf{u}_n) + m_i n_i \bar{\nu}_{in}(\mathbf{u}_i - \mathbf{u}_n) \tag{3.28}$$

The internal energy transferred to species k due to elastic collisions with species α is evaluated as [95]:

$$Q_k^{k\alpha} = \frac{3m_k}{m_\alpha} n_k \bar{\nu}_{k\alpha} \left(k_B T_\alpha - k_B T_k\right) \tag{3.29}$$

Equation (3.29) yields the following relations for the collisional exchange of internal energy between the electron, ion, and neutral species.

$$Q_e = \frac{2m_e}{m_i} n_e \bar{\nu}_{ei}(C_v T_i - C_v T_e) + \frac{2m_e}{m_n} n_e \bar{\nu}_{en}(C_v T_n - C_v T_e) \tag{3.30}$$

$$Q_i = \frac{2m_e}{m_i} n_e \bar{\nu}_{ei}(C_v T_e - C_v T_i) + \frac{2m_i}{m_n} n_i \bar{\nu}_{in}(C_v T_n - C_v T_i) \tag{3.31}$$

$$Q_n = \frac{2m_e}{m_n} n_e \bar{\nu}_{en}(C_v T_e - C_v T_n) + \frac{2m_n}{m_i} n_n \bar{\nu}_{ni}(C_v T_i - C_v T_n) \tag{3.32}$$

Reactions

The reactions of ionization and recombination are assumed to dominate within the plasma discharge. Further, due to the collisional nature of ET plasmas, electron impact ionization and three-body, electron recombination reactions are expected to dominate. The electron impact ionization rate coefficients are determined from the work of Voronov [96] who presents a practical fit formula for use in computations. The three-body, electron recombination rate coefficients are determined from Mitchner and Kruger [1].The recombination rate coefficient for three-body, electron recombination is given by:

$$\alpha_{rec} = 1.09 \times 10^{-20} T_e^{-(9/2)} n_e \quad \mathrm{m^3 sec^{-1}} \tag{3.33}$$

where T_e is in K, and n_e is in m^{-3}.

3.1.6 Transport Properties

Species' Thermal Conductivities

The species thermal conductivity is given by [97]:

$$k_k = \frac{5}{2} \frac{n_k k_B^2 T_k}{m_k \bar{\nu}_{kh}} \tag{3.34}$$

where the subscript k indicates the species (e=electrons, i=ions, n=neutrals), and ν_{kh} is the collision frequency between species k and heavy particles, including intra-species collisions.

Plasma Electrical Conductivity

The plasma electrical conductivity is given by [1]:

$$\frac{1}{\sigma} = \frac{1}{\sigma_{en}} + \frac{1}{\sigma_{ei}} \tag{3.35}$$

where σ is the plasma electrical conductivity, σ_{en} is the electron-neutral conductivity, and σ_{ei} is the electron-ion conductivity. The electron-neutral conductivity is given by:

$$\sigma_{en} = \frac{n_e e^2}{m_e \bar{\nu}_{en}} \tag{3.36}$$

The electron-ion conductivity is evaluated per the recommendation offered by Woods [7].

$$\sigma_{ei} = 1.98 \frac{n_e e^2}{m_e \bar{\nu}_{ei}} \tag{3.37}$$

3.1.7 Electric Field Determination

Due to computational constraints, the implementation of Maxwell's equations in the THOR simulation model and code has been delayed and remains topic for future research. The magnetic pressure in ET plasma discharges has been shown to be much smaller than the

kinetic pressure [6]. Therefore, the effects of the self-induced magnetic fields are neglected. In this work, as a first approximation, the electric field is evaluated based on Ohm's law. This approximation simplifies the complexity inherent in the electrodynamics at play and allows for the rough estimation of the applied electric field that drives plasma heating and charged particle motion. As discussed in Sec. 5.3, this approximation yields results that match well with experimental data and indicate that the macroscopic behavior of ET plasma discharges has been captured using this approach.

The applied electric field is evaluated using Ohm's law which is given by:

$$\mathbf{J} = \sigma \mathbf{E} \tag{3.38}$$

where $\mathbf{J}$ is the current density, σ is the plasma electrical conductivity, and $\mathbf{E}$ is the electric field. The current density is determined from the input current pulse. Example pulses of discharge current that are used as simulation inputs are shown in Fig. 1.11. The plasma electrical conductivity is represented by σ and is determined from the simulated plasma composition. Using Eq. (3.38), the applied electric field can be evaluated.

Taking advantage of the narrow geometry of the ET plasma source, electric current is assumed to be uniform along the axis of the plasma source. In addition, the radial current and radial applied electric fields are assumed to be negligible. The current density within the plasma source is then only a function of time. Reducing Ohm's law using this approach

yields:

$$J_z(t) = \frac{I(t)}{\pi R^2} = \sigma_{eq}(z,t)E_z(z,t) \tag{3.39}$$

where J_z is the axial component of the current density, I is the input current, R is the source radius, σ_{eq} is the equivalent conductivity over the ET source radial cross-section, E_z is the axial component of the electric field, z is the axial position in the ET source, and t is the simulation time. The independent variables z and t have been explicitly specified for the terms in Eq. (3.39). The axial electric field can be determined easily from Eq. (3.39).

3.1.8 Radiation Transport

The THOR model and code are equipped with two different radiation approximations: a black-body radiation approximation and a diffusion approximation for radiation heat transfer.

Black-body Radiation Approximation

In the black-body radiation approximation, the plasma core is assumed to radiate in the radial direction at a temperature equal to the average heavy-particle temperature over the geometric cross-section of the plasma source. This average temperature is used to determine the radiation heat flux from the plasma core to the ablating surface.

$$q''_{rad} = \sigma_{SB}(T^4_{avg} - T^4_{boil}) \tag{3.40}$$

where q''_{rad} is the ablation-inducing heat flux from the plasma to the ET source liner, σ_{SB} is the Stefan-Boltzmann constant, T_{avg} is the average heavy particle temperature over the source cross-section, and T_{boil} is the boiling temperature of the ET source liner material. The radiant energy loss, and therefore the q'''_{rad} terms in Eqs. (3.6) and (3.12), is determined by distributing the energy loss over the geometric cross-section of the ET plasma source and weighting the energy loss towards computational cells with higher internal energy.

Diffusion Approximation for Radiation Heat Transfer

As an alternative to the black-body radiation approximation, a diffusion approximation for radiation heat transfer has also been implemented in the THOR simulation code. The plasmas generated in ET plasma discharges are dense plasmas and the diffusion approximation has been shown to be valid for these plasmas provided an appropriate flux limiter is utilized [78,79]. Hahn et al. [79] utilized a multi-group diffusion model to capture the radiation heat transfer in plasmas similar to those produced in ET plasma discharges. They proposed a radiation flux limit equal to:

$$S_g = \frac{c}{2} U_g \tag{3.41}$$

where S_g is the radiation heat flux in frequency group g, c is the speed of light, and U_g is the radiant energy in frequency group g. Hahn et al. [79] also propose a boundary condition for the radiation heat flux at the interface between the plasma and the ablating surface that is equal to the flux limit. They argue for this condition based on the anisotropy of the radiation field at this interface and the tendency of the radiation to stream towards

the ablating surface. These affects are due to the fact that the ablating surface provides no incoming photons due to its low temperature. Hahn et al. therefore set the boundary radiation flux at this interface equal to the radiation flux limit specified in Eq. (3.41).

The diffusion model for radiation heat transfer currently implemented in the THOR simulation code is similar to the approach used by Ngo [74,98] but incorporates the findings of Hahn et al. [79]. In order to limit the complexity of the problem, the use of an averaged-group model for the radiation heat transfer has been implemented in this work. In this averaged-group model, the flux limit and ablating surface boundary flux are given by:

$$S_{rad} = \frac{c}{2} U_p \tag{3.42}$$

where S_{rad} is the radiation flux at the ablating surface boundary and the flux limit, and $U_p = 4\sigma_{SB} T_p^4 / c$ is the radiant energy of the plasma, and T_p is the plasma temperature.

By the diffusion approximation, the radiation heat transfer within the simulation domain is evaluated based on Fourier's law of conduction.

$$\mathbf{q}_{rad} = -k_{rad} \nabla T \tag{3.43}$$

where $\mathbf{q}_{rad}$ is the radiation heat flow vector, and k_{rad} is the radiation thermal conductivity. The evaluation of k_{rad} is performed as done in the work of Ngo [74,98].

$$k_{rad} = \frac{16}{3} \sigma_{SB}\, l_{rad}\, T^3 \tag{3.44}$$

where σ_{SB} is the Stefan-Boltzmann constant, l_{rad} is the radiation mean free path for the plasma, and T is the plasma temperature. The radiation mean free path is approximated by [75]:

$$\text{(MKS units)} \quad l_{rad} = 0.9017 \frac{m_e^{3/2} c}{h^2 k_e^3 e^6} \frac{(kT)^{7/2}}{N^2 \bar{m}(\bar{m}+1)^2} \quad \text{[m]} \tag{3.45}$$

where m_e is the electron mass in [kg], c is the speed of light in [m/s], h is Plank's constant in [Js], k_e is Coulomb's constant in [Nm^2/C^2], e is the electron charge in [C], k is Boltzmann's constant in [J/K], T is the temperature in [K], N is the number density in [m^{-3}], and $\bar{m} = \bar{Z}$ is the average charge state [unitless]. Coulomb's constant is given by:

$$k_e = \frac{1}{4\pi\epsilon_0} \tag{3.46}$$

It is important to emphasize the units in Eq. (3.45). The authors in Ref. [75] use CGS units. The CGS unit of electron charge is not compatible with the MKS unit of electron charge. Therefore, the inclusion of Coulomb's constant is required in MKS units. Under this approximation for radiation heat transfer, the q'''_{rad} term in Eq. (3.6) and Eq. (3.12), is replaced by $\nabla \cdot \mathbf{q}_{rad}$.

3.1.9 Ablation

The ablation of the ET source liner material is computed using the radiation flux to the surface. The ablation flux is related to the radiation heat flux through the equation:

$$\Phi_{abl} = \frac{q''_{rad}}{H_{sub}} \tag{3.47}$$

where Φ_{abl} is the ablation flux of neutral particles at the ablating surface in units of $[\mathrm{m}^{-2}\mathrm{s}^{-1}]$, q''_{rad} is the radiation heat flux deposited on the ablating surface in units of $[\mathrm{W/m}^2]$, and H_{sub} is the sublimation energy of the ET source liner material in units of [J]. The physical reasoning for this particular ablation model is based on the assumption that all the radiation heat flux is consumed in the ablation process and the ablated particles are returned to the plasma domain. This model has been applied in previous work [24, 26, 69].

3.1.10 Summary of Model Simplifications and Assumptions

- The continuum assumption is made in order to treat the plasma species as fluids. This is reasonable considering the species densities that are expected to develop inside ET plasma discharges ($n_e \sim n_i \sim 10^{23} - 10^{25}$ m^{-3} and $n_n \sim 10^{25} - 10^{27}$ m^{-3}).

- Gravitational potential energy effects are negligible to a first approximation.

- The incorporation of a plasma sheath model at the ablating or electrode surfaces is beyond the scope of this study. Due to the transient nature of a pulsed ET plasma

discharge, it is questionable whether or not a plasma sheath plays an important role in the physics. Conclusive evidence of the presence of a sheath model forming in these devices is not known to have been reported previously. Therefore, the inclusion of a plasma sheath model has been left to future studies.

- The amount of radiation heat flux absorbed by the wall material is negligible to a first approximation. All radiant energy goes into ablating the liner material.

- The source liner material is fully dissociated in the ablation process and yields only monatomic particles ($\gamma = 5/3$) [28].

- In this work, Lexan polycarbonate has been simulated as the liner material inside ET plasma discharges. The ablated particles of the Lexan liner consist of carbon, hydrogen, and oxygen. The collisions between the species are assumed to dominate over the effects of chemical reactions. This is reasonable considering the large amounts of energy deposited into an ET plasma discharge via the electric current and the resulting high temperatures.

- The mass difference between a neutral particle and an ion is neglected, and therefore $m_i = m_n$. This mass difference is five orders of magnitude lower than the neutral and ion masses and its inclusion is not expected to alter simulated results.

- The degree of ionization in the plasma is low enough so that the electron and ion viscosities can be safely ignored.

- Viscous effects in the neutral species are neglected to a first approximation. The effect of viscous forces and viscous heating of the fluid in ET plasma discharges has been neglected in the past [30, 39, 44, 69]. For plasma thrusters with the pressures typically reached in an ET plasma discharge, Pekker [38] has shown that the neglect of viscous heating is justified. It is not expected that the inclusion of viscous effects in the neutral species would significantly impact simulated results reported in this work.

- To a first approximation, the applied electric field dominates the behavior of the plasma and can be approximated using Ohm's law. While a fully-consistent treatment of the electric and magnetic fields in ET plasma discharges would involve the implementation of Maxwell's equations, at this point in the development of the THOR code, an Ohm's law approximation is considered to be sufficient to obtain estimations of macroscopic fluid behavior. In addition, due to the narrow geometry of the plasma source, the radial current and electric field components are neglected. This is discussed in more detail in Chapter 5.

3.2 Verification

Several tests were undertaken in order to verify the implementation of the numerical methods used in the THOR simulation code. Due to the complexity of the physics being simulated and the strong coupling of the species, verification test cases were carried out for individual components of the simulation code.

3.2.1 Hydrodynamics: The Sod Test Problem

The well known Sod test problem [99] was used in order to verify THOR's treatment of the hydrodynamic terms. These terms include the convection term for the continuity, momentum and energy equations, as well as the pressure gradient terms in the momentum and energy equations. Sod developed an analytical solution for a 1D shock tube problem. This analytical solution is outlined by Toro [100]. The initial conditions for the shock tube problem are shown in Fig. 3.2. The shock tube problem was simulated with a single neutral species using the hydrodynamics module developed for the THOR simulation code. The analytical solution is shown with simulation results in Fig. 3.3 for a simulation time of 20 µs. The hydrodynamics module used in the THOR code demonstrates convergence to the analytical solutions, and the hydrodynamics module is verified. Detailed convergence rates are reported

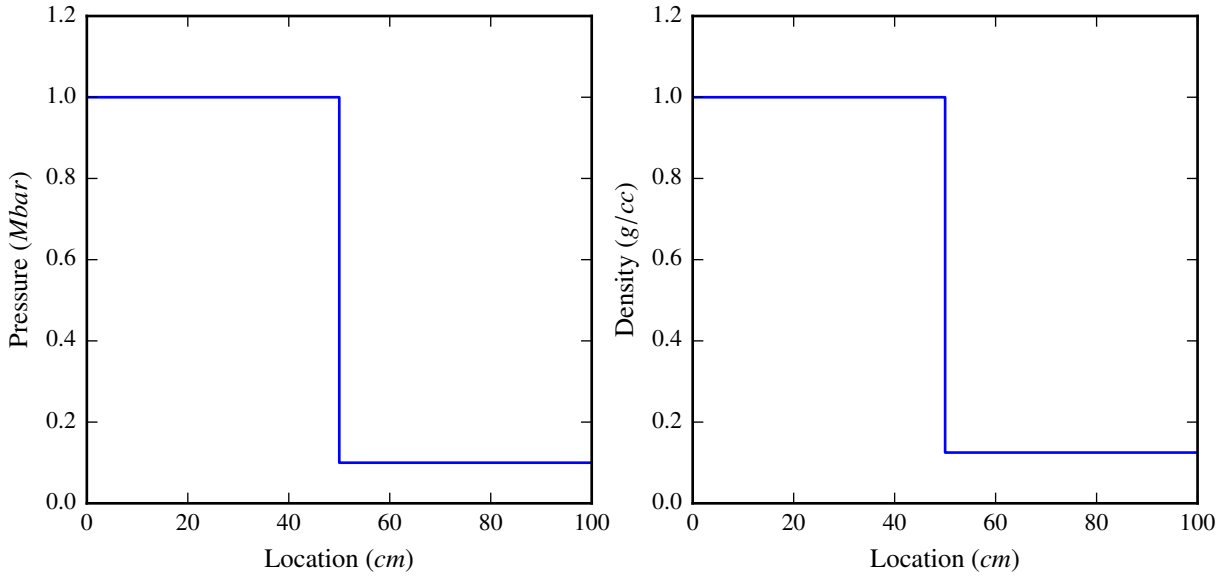

Figure 3.2: Initial conditions for the Sod test problem [99]. At $t = 0$, the separation barrier at the center of the domain is removed, and a shock wave propagates in the positive direction with a relaxation wave moving in the negative direction.

in Sec. 4.3.6. The formal order of accuracy of the methods used in the THOR hydrodynamics module is first order. The observed order of accuracy in the simulation results as reported in Sec. 4.3.6 is less than first order. This lower order convergence is expected even for correctly implemented governing equations due to the discontinuities in the analytical solution [101].

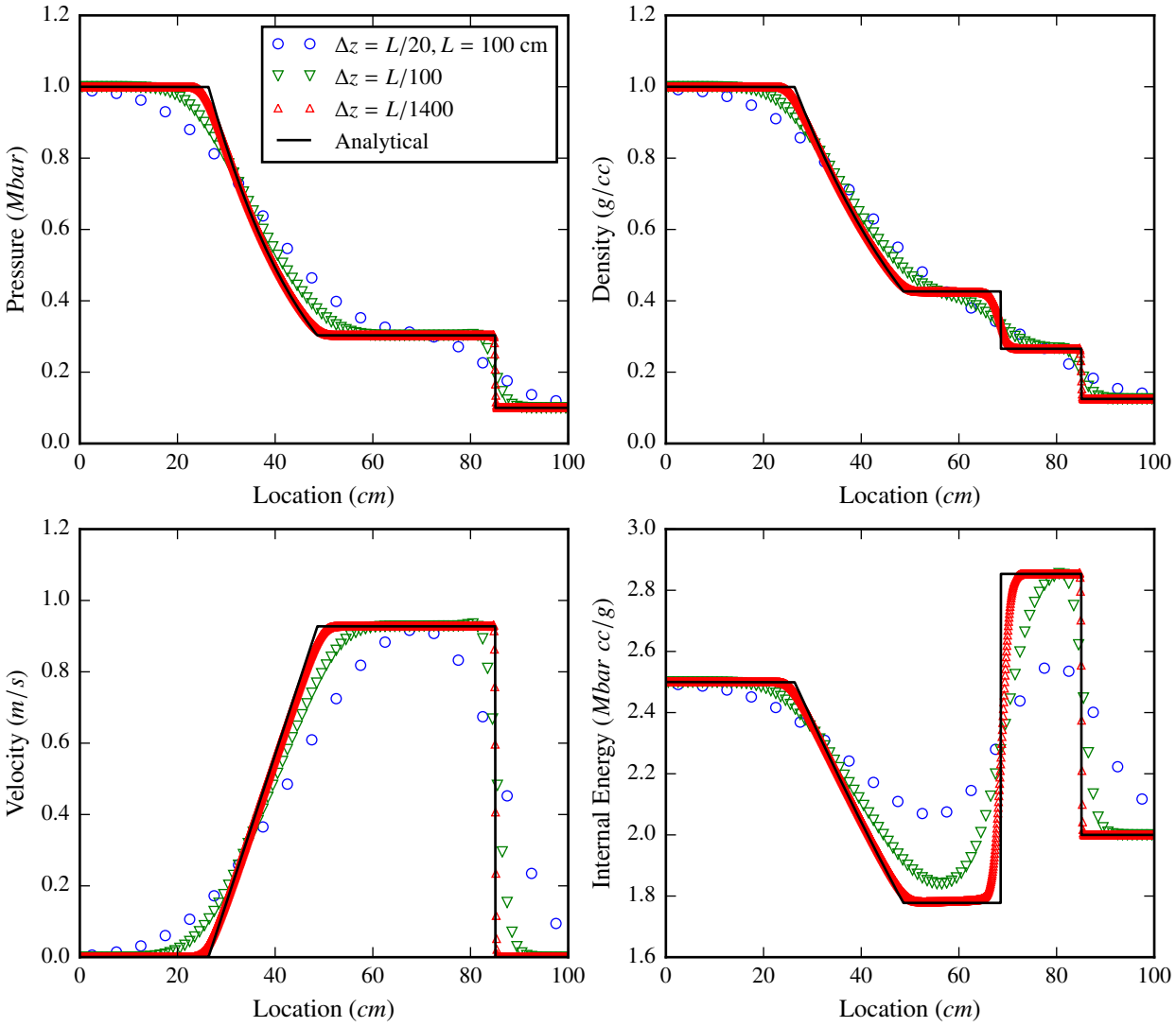

Figure 3.3: The analytical solution to the Sod test problem is shown with simulation results generated from THOR's hydrodynamic module. Only a single neutral species was simulated with $\gamma = 1.4$. Results and analytical solution are shown for a time of 20 µs. The domain length for all simulations was 100 cm.

3.2.2 Hydrodynamics: The Sedov Test Problem

In order to further verify correct implementation of the governing equations for the hydrodynamics used in the THOR code, the Sedov test problem was also simulated [102]. The Sedov test problem involves an initial concentration of energy at the center of an explosion. As time is allowed to progress, a blast wave propagates outward from the center. The blast energy used in this verification test case was $E_0 = 1.85 \times 10^{13}$ J/m along the centerline of the axisymmetric domain. The radial extent of the simulation domian was set to 1 m with initial temperature and pressure set essentially to zero except along the centerline. The initial density is set to 1.25 kg/m^3. The initial velocity is set to zero. Only a neutral species is simulated for this test case. The analytical solution is based on an energy parameter, E, which is based on the total blast energy, E_0, according to:

$$E_0 = \alpha E \tag{3.48}$$

The literature is unclear what specific value of α should be used in the case of cylindrical coordinates. Plotted results contained in Ref. [102] indicate $\alpha \approx 1$ for $\gamma = 1.4$. However, it was found that an additional geometry factor was needed in order to account for the cylindricity of the domain. Therefore, the α used in this analysis has been set to $2/(3\pi)$.

The simulation results for the Sedov test problem are reported in Chapter 5. The simulation results demonstrate qualitative convergence to the analytical solution of the Sedov

test problem. This further verifies correct implementation of the governing equations used in the THOR simulation code.

3.2.3 Electrons: Semi-Implicit Solver

The electron solver in the THOR simulation code captures the time-evolution of the electron species using the drift-diffusion approximation. The continuity and energy equations for the electrons are solved using an alternating direction implicit (ADI) method to march forward in time. In order to verify correct implementation of this method, a trend test case has been employed [103]. This test case simulates only the electron fluid which is initially at a uniform density and temperature with zero velocity. At the beginning of the simulation, the electron fluid is acted upon by a constant applied electric field. The electron fluid responds to the electric field and moves towards a distribution where the diffusion of electrons balances the drift.

The simplified governing equations for the electrons that apply to this test case are shown below.

$$\frac{\partial n_e}{\partial t} = -\nabla \cdot (n_e \mathbf{u}_e) \tag{3.49}$$

$$\mathbf{u}_e = -\frac{e\mathbf{E}}{m_e \bar{\nu}_{eh}} - \frac{\nabla P_e}{n_e m_e \bar{\nu}_{eh}} \tag{3.50}$$

$$\frac{\partial}{\partial t}(n_e C_v T_e) = -\nabla \cdot (\mathbf{u}_e n_e C_v T_e) - \nabla \cdot \mathbf{q}_e \tag{3.51}$$

A constant $\bar{\nu}_{eh}$ is used in Eq. (3.50) as well as in the evaluation of the electron thermal conductivity. This accounts for drag on the electron fluid due to interactions with a background gas. The background gas does not affect the electron fluid in any other way for this test case.

Two parameters are used in order to observe the behavior of the electron distribution as it progresses in time under the influence of the applied electric fields. The first is the normalized global time derivative defined as:

$$\bar{\theta} = \sqrt{\frac{\sum_n \theta_n^2 \alpha_n}{\sum_n \alpha_n}} \tag{3.52}$$

where θ_n is the simulated discrete time derivative for control volume n, and α_n is the volume of control volume n. The parameter θ_n represents the discrete form of the left hand side of either Eq. (3.49) or Eq. (3.51). The second parameter is the normalized global error defined as:

$$\bar{\epsilon} = \sqrt{\frac{\sum_n (\psi_n - \theta_n)^2 \alpha_n}{\sum_n \alpha_n}} \tag{3.53}$$

where ψ_n represents the discrete evaluation of the right hand side of either Eq. (3.49) or Eq. (3.51). The parameter ψ_n is explicitly calculated at the end of a time step based on the simulated electron temperature and density distributions.

For this verification test case, acceptance criteria are as follows: (1) the rate at which the normalized global time derivative tends to zero must be independent of mesh density, and (2) the normalized global error must be small relative to the normalized time derivative.

Figure 3.4: Geometries simulated in the electron verification test case: (a) $\tilde{L}$ = 3 cm, (b) $\tilde{L}$ = 12 cm, and (c) $\tilde{L}$ = 29 cm. The geometries shown represent the 2D computational domain with the lower boundary as the axis of symmetry.

The first criterion ensures the demonstration of correct spacial resolution of the discretized domain. The second criterion is a check for correct decomposition of the discretized governing equations. As mentioned previously, the electron governing equations are advanced using an ADI method. This method relies on the decomposition of the discretized terms of the governing equations into a coefficient matrix for an semi-implicit solution. This decomposition involves complex algebraic manipulations and can be a source of errors. The normalized global error is computed directly from the field variables and does not depend on this decomposition. By verifying small normalized global error, the correct decomposition of the discretized governing equations is demonstrated. This is the purpose of the second acceptance criterion.

Three different geometries were used to verify the electron solver. These geometries have characteristic lengths of $\tilde{L}$ =3, 12, and 29 cm. These geometries are illustrated in Fig. 3.4. The governing equations for this test case are discretized with two different computational meshes for each simulated geometry. The first mesh, or the base mesh, for each geometry has an average $\Delta r = \Delta z = 5 \times 10^{-4}$ m. The second mesh is roughly twice the refinement

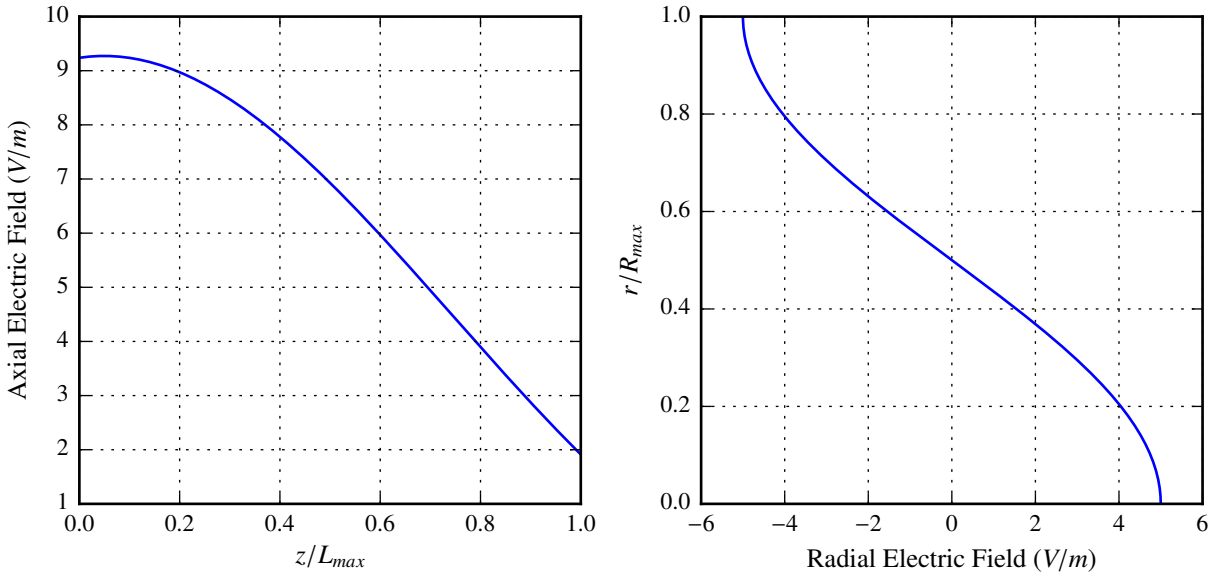

Figure 3.5: Constant applied electric field distributions applied for the three different geometries used for electron ADI solver verification test case.

of the base mesh. The applied constant electric field components used in the simulations for these three geometries are shown in Fig. 3.5.

In order to analyze the simulation behavior for the purposes of verification, the parameters defined in Eqs. (3.52) and (3.53) are plotted versus simulation time. These parameters are plotted for the continuity equation in Fig. 3.6. Figure 3.6(a) shows that the normalized global time derivative tends towards steady state as expected. Two different mesh resolutions are shown for each simulated geometry in Fig. 3.6(a). The rates of convergence to a steady solution are shown to be independent of the mesh resolution which satisfies the first criterion for acceptance. As expected, the geometries with longer characteristic lengths take longer to approach a steady solution. This is due primarily to the greater time required for electrons to traverse the longer distances.

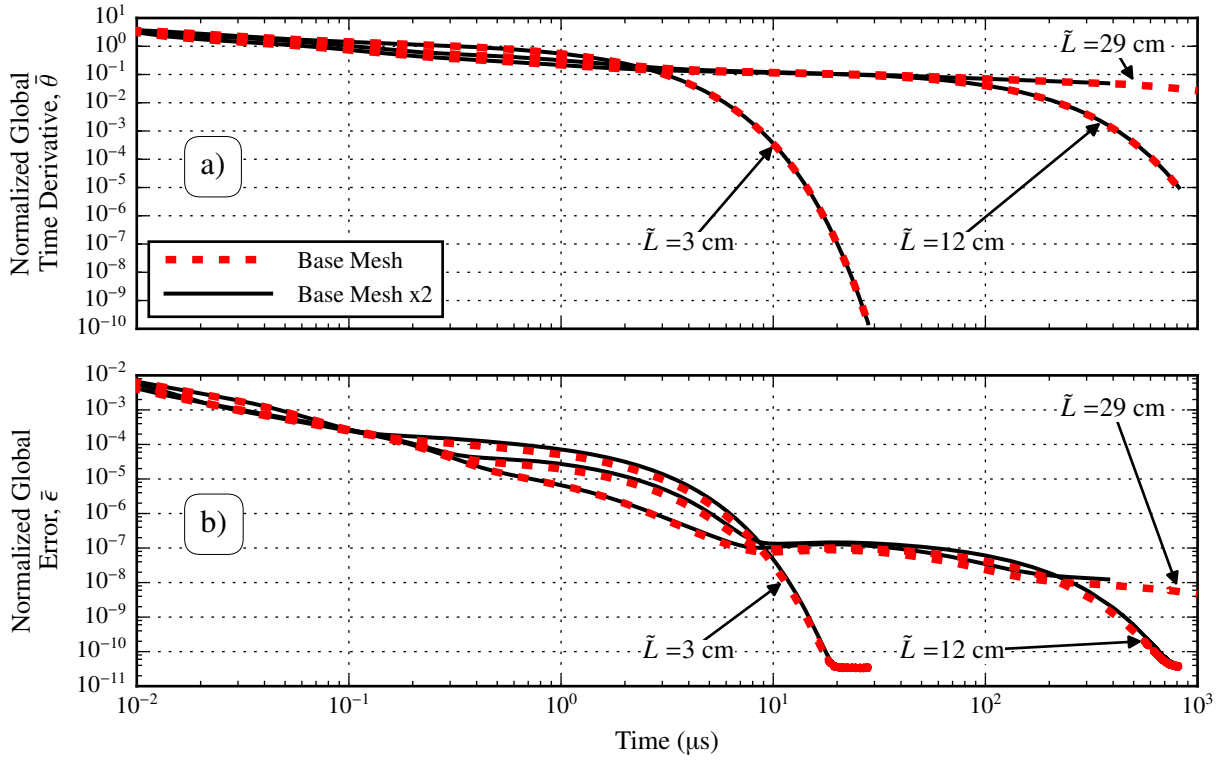

Figure 3.6: Time history of (a) the normalized global time derivative, and (b) the normalized global error for the electron continuity equation. Similar behavior is observed for the electron energy equation. The results from a base mesh and a mesh with double the base mesh's refinement are shown.

The time history of the normalized global error in the continuity equation is shown in Fig. 3.6(b). Comparing the magnitude of the error in Fig. 3.6(b), with the magnitude of the normalized time derivative Fig. 3.6(a) reveals that the errors are relatively small. In the evaluation of the error, the time derivative term is computed discretely at the end of a time step, and the remaining terms in Eq. (3.49) are computed using only the new time values of the simulation parameters. In the actual implementation, both new-time and old-time simulation values are used to advance the simulation at each time step. Therefore, a small error is expected in these calculations. Nevertheless, these errors should be small and diminishing as the simulation approaches steady state. This is observed in Fig. 3.6(b). The continuity errors do approach zero and can be seen reaching machine precision in the case of the simplest geometry ($\tilde{L}$ =3 cm). This satisfies the second criterion for acceptance. Similar trends are observed for the electron energy equation.

3.3 Validation

The THOR simulation code was compiled using both GCC (versions 4.6.3, 4.7.2, and 4.8.4) and Intel® (version 13.1) compilers. Open MPI (versions 1.4.3, 1.6.4, and 1.8.1) has been used to facilitate distributed memory parallelism. Shared memory parallelism has been facilitated by the compilers' implementations of OpenMP®. The THOR simulation code has been run on up to 12 cores on the HokieSpeed supercomputer at Virginia Tech using Intel® Xeon E5645 (Westmere) CPUs. The code has also been run using 6 cores on the

Ithaca supercomputer at Virginia Tech using Intel® Xeon E5520 (Nehalem) CPUs. Results have also been obtained using 6 cores on an HP Z220 Workstation with Intel® Core i7-3770 CPUs.

3.3.1 Total Ablated Mass

Black-body Radiation Approximation

Validation of simulation models for ET plasma discharges has been performed in the past using the total measured ablated mass in these devices. Total ablated mass measurements have been taken using the PIPE device and are reported by Winfrey et al. [26]. Here, the THOR code predictions of the total ablated mass are compared with these experimental measurements. In addition, the discretization uncertainty has been calculated for the THOR model results using the Grid Convergence Index (GCI) method [104]. The comparison of the THOR simulation results using the black-body radiation approximation for these experiments is shown in Fig. 3.7. The mesh resolutions used for the results reported in this section are specified in Table 3.5. The discretization uncertainty estimates evaluated using the GCI method are summarized in Table 3.6. The ablated mass values predicted for the different mesh resolutions are shown in Table 3.7.

The simulation results for the 4.09 kJ shot (corresponding to P228 with a 30 kA nominal peak current) indicate a much higher discretization uncertainty compared to the uncertainties of the other shot simulations. The reasons for the large estimated discretization uncertainty

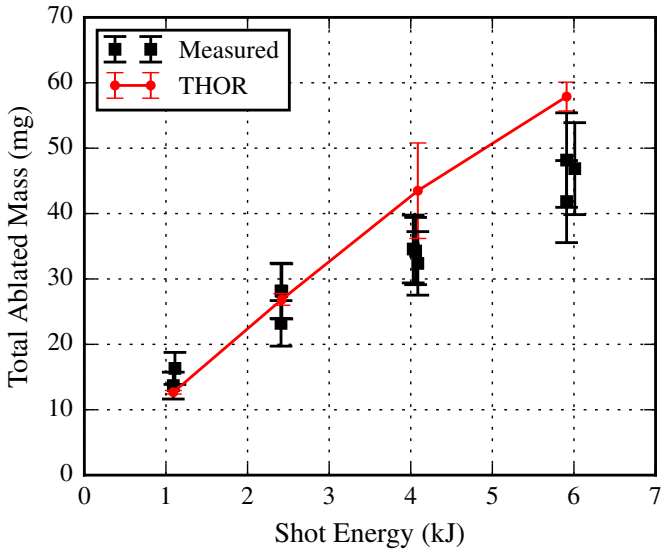

Figure 3.7: Comparison of total ablated mass predicted using the THOR simulation code and measured from the PIPE device. Measured values are reported by Winfrey et al. [26]. Computational uncertainty was estimated using the GCI method [104]. THOR simulation results were generated using the black-body radiation approximation.

Table 3.5: Mesh resolutions used to obtain THOR simulation results using the black-body radiation approximation. The domain radius was 2 mm and the domain length was 9 cm.

	Fine	**Medium**	**Coarse**
Resolution	28×420	18×360	8×360
Cell Count	11760	6480	2880
Δr (mm)	0.0714	0.111	0.250
Δz (mm)	0.214	0.250	0.250

Table 3.6: Discretization uncertainty estimates for the total ablated mass predicted using the THOR simulation code and the black-body radiation approximation. Total ablated mass was recorded at a simulation time of 250 µs.

Shot Energy (kJ)	Ablated Mass (mg)	Apparent Order of Convergence	Approximate Relative Error	Extrapolated Relative Error	Fine-grid Convergence Index
1.09	12.67	1.3	0.8%	1.7%	2.1%
2.42	26.87	2.1	2.2%	2.7%	3.3%
4.09	43.49	0.6	2.5%	15.5%	16.8%
5.91	57.89	2.2	2.8%	3.1%	3.8%

Table 3.7: Ablated mass results for different mesh resolutions. The black-body radiation approximation was used to obtain these results. All ablated mass values were recorded at a simulation time of 250 µs.

Shot Energy (kJ)	Ablated Mass (mg)		
	Fine	**Medium**	**Coarse**
1.09	12.67	12.75	12.89
2.42	26.87	27.52	28.04
4.09	43.49	44.56	45.90
5.91	57.89	59.46	60.77

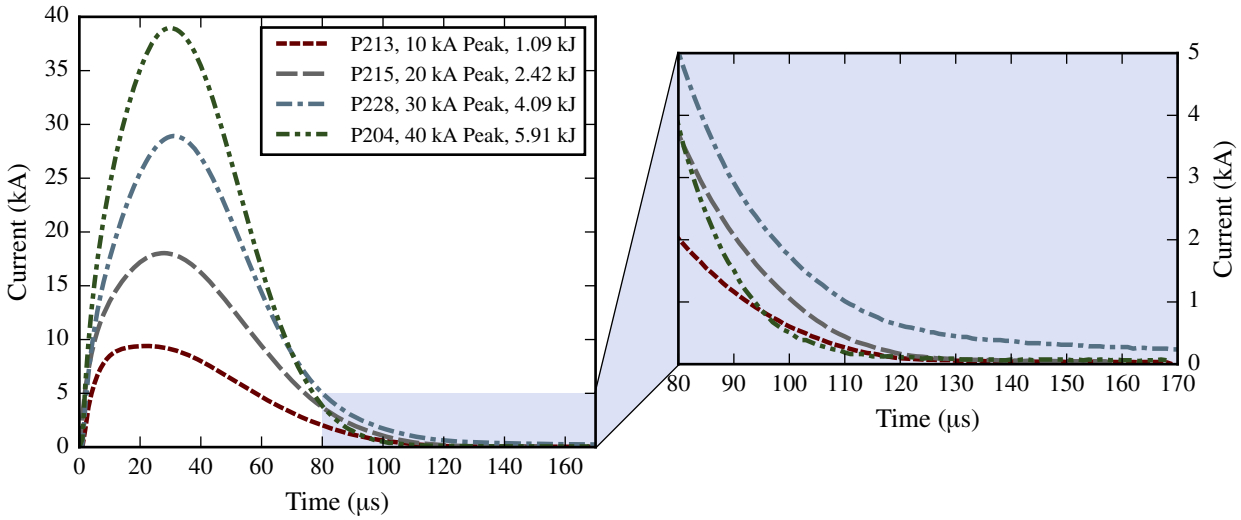

Figure 3.8: Measured current shot profiles of ET plasma discharges in the PIPE device. Legend indicates shot identifier, nominal peak current, and measured input energy to the discharge. The tail portion of the current pulses is shown to emphasize the difference in the measured currents as the current recedes. These current pulses are used as simulation inputs to the THOR simulation code.

for the 4.09 kJ shot (P228) are puzzling and reflect the sensitivity of the GCI method in estimating discretization uncertainty. The current profiles for the four simulated shots are shown in Fig. 3.8. The current pulses shown in Fig. 3.8 are used as simulation inputs to the THOR simulation code. As the current in each current pulse is decreasing, Fig. 3.8 shows that the current for P228 retains a higher current throughout the end of the discharge compared with the other current pulses. It is likely that this different behavior in shot P228 causes a higher estimated discretization uncertainty.

Diffusion Approximation for Radiation Heat Transfer

The THOR simulation code can be used to approximate the radiation heat transfer inside an ET plasma discharge using the diffusion approximation. The code predictions for the total

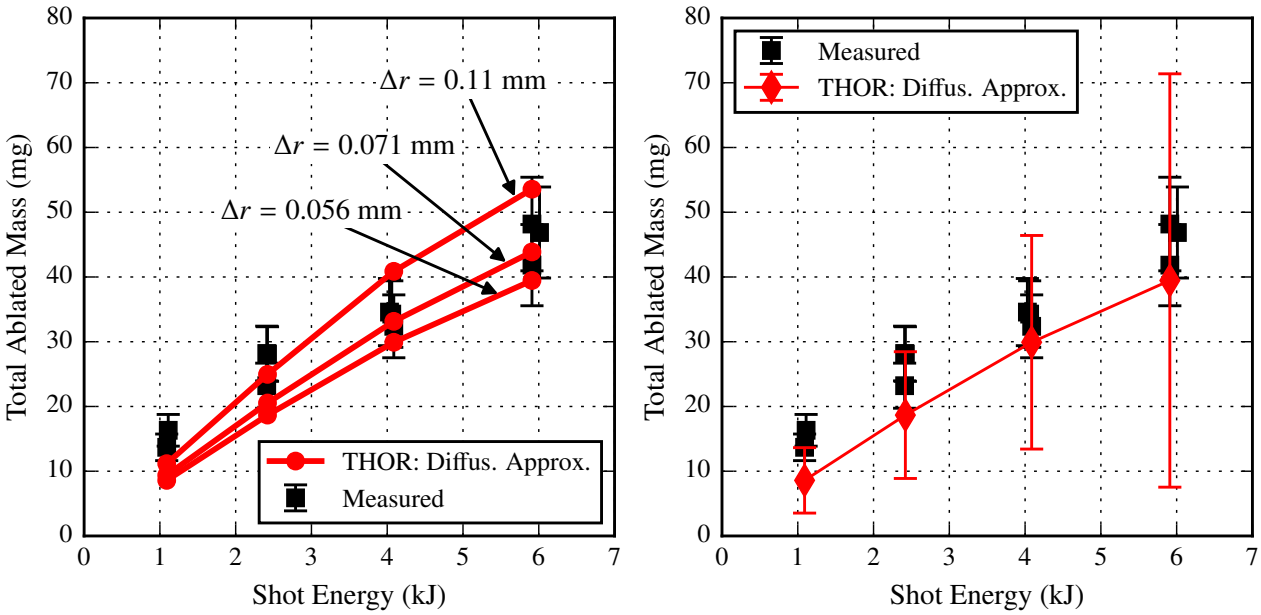

(a) Comparison of THOR simulation results using the diffusion approximation for radiation heat transfer for three different meshes.

(b) Presentation of discretization uncertainty for THOR simulation results using the diffusion approximation for radiation heat transfer.

Figure 3.9: Comparison of total ablated mass predicted using the THOR simulation code and measured from the PIPE device. Measured values are reported by Winfrey et al. [26]. THOR simulation results were generated using the diffusion approximation for radiation heat transfer. Discretization uncertainty was estimated using the GCI method [104].

ablated mass using this approximation are reported in Fig. 3.9(a-b). The mesh resolutions used to obtain the data reported in this section are shown in Table 3.8. The mesh sizes used to compute the discretization uncertainties in this section correspond to the Δr values reported in Table 3.8 as the discretization in the radial direction contributes most to mesh convergence. The approximate discretization uncertainties computed using the GCI method are reported in Table 3.9.

It is clear from Fig. 3.9 and Table 3.9 that, for the diffusion approximation for radiation heat transfer, the THOR simulation code produces results that are dependent on the mesh.

Table 3.8: Mesh resolutions used to obtain THOR simulation results using the diffusion approximation for radiation heat transfer. The domain radius was 2 mm and the domain length was 9 cm.

	Fine	**Medium**	**Coarse**
Resolution	36×360	28×420	18×360
Cell Count	12960	11760	6480
Δr (mm)	0.0556	0.0714	0.111
Δz (mm)	0.250	0.214	0.250

Table 3.9: Discretization uncertainty estimates for the total ablated mass predicted using the THOR simulation code and the diffusion approximation for radiation heat transfer. Total ablated mass was recorded at a simulation time of 250 µs.

Shot Energy (kJ)	Ablated Mass (mg)	Apparent Order of Convergence	Approximate Relative Error	Extrapolated Relative Error	Fine-grid Convergence Index
1.09	8.6	0.7	9.2%	88.9%	58.8%
2.42	18.7	0.9	10.0%	72.2%	52.4%
4.09	29.9	0.9	10.8%	78.9%	55.1%
5.91	39.5	0.6	11.2%	183.5%	80.9%

Computational constraints have limited the investigation of the effects of further mesh refinement. These results reveal areas for improvement in the THOR simulation code. It is possible that a more detailed treatment of the ablating wall boundary condition could help with mesh convergence. Currently in the simulation code, the ablated material enters the simulation domain at the material boiling temperature. It is possible that this material is actually at a higher temperature [31].

The diffusion approximation for radiation heat transfer predicts total ablated mass values within the experimental uncertainty for ET plasma discharges with input energies > 3 kJ. For these shots, the black-body approximation over-predicts the total ablated mass values. A detailed comparison of these methods, namely the black-body and diffusion approximations for radiation heat transfer, is offered in Chapter 6.

3.3.2 Measured Electrical Conductivity

Experiments have been conducted on the PIPE device to measure the electrical conductivity during an ET plasma discharge. These experimental measurements were performed by other authors and some of the measured data has been reported previously [26]. Remaining experimental measurements have been received from the original experimentalists via scholarly communication. The comparison of the measured electrical conductivity with simulated results produced using the THOR simulation code are reported in Chapter 5 in Fig. 5.5

and Fig. 5.6. The THOR simulation results were generated using the black-body radiation approximation.

3.3.3 Measured Electric Field

Measurements of the electric field strength produced in evaporation dominated high-current arcs, devices similar to ET plasma discharges, have been performed by Niemeyer [32]. Niemeyer measured the electric field strength in these devices using a variety of ablating liner materials including metals, ceramics, and polymers. The polymers used by Niemeyer were polyethylene (PE), or $(CH_2)_n$, and formaldehyde, or $(CH_2O)_n$. In this work, the THOR simulation code has been used to simulate ET plasma discharges with the polymer Lexan, or $(C_{16}H_{14}O_3)_n$, used as an ablating liner material. A comparison of Niemeyer's measurements using polymer materials with THOR's simulation results using Lexan is made in Chapter 5 in Fig. 5.7. The simulated electric field strength using THOR is shown to be consistent with the measurements of Niemeyer and also demonstrate correct scaling with the applied current density.

3.4 Model Sensitivity to Initial Pressure

The initial pressure of an experimental ET plasma discharge is typically on the order of a few kPa. For the THOR simulation code, the initial pressure can be specified by the code user. For simulation runs, it is often advantageous to initialize the simulation at higher initial

pressures near atmospheric pressure (100 kPa). This higher initialization pressure enhances simulation stability in the early portions of the simulation and allows for faster simulation during these initial stages. The sensitivity of the simulation code to the initialization pressure is briefly analyzed in this section.

In order to investigate the sensitivity of the THOR simulation model to the initial pressure, two different simulations were performed and are compared in this section. Both simulations were of a current pulse peaking at nominally 10 kA and having an active pulse length of approximately 100 µs. One simulation was initialized at a pressure of 2660 Pa. The second simulation initialized the pressure at 100 kPa. To characterize the simulation's sensitivity to the initial pressure, the internal plasma pressure located at the plasma source centerline and 6 cm from the breech of the source is recorded in time and plotted in Fig. 3.10(a). Figure 3.10(a) shows that there is little difference in the plotted results for the internal plasma pressure for these two simulations. The percent difference in the simulated internal plasma pressure is show in Fig. 3.10(b). Figure 3.10(b) shows that the percent difference in simulated internal plasma pressure drops quickly as the discharge is initialized. The percent difference is below 3% before a simulation time of 10 µs. The percent difference remains below 1% after a simulation time of 20 µs. These results show that the overall behavior of the discharge is not sensitive to the initial pressure for the 10 kA peak current pulse that has been investigated. This is due to the much higher pressures attained compared with the initial pressures considered here. Naturally, for lower current shots where the discharge

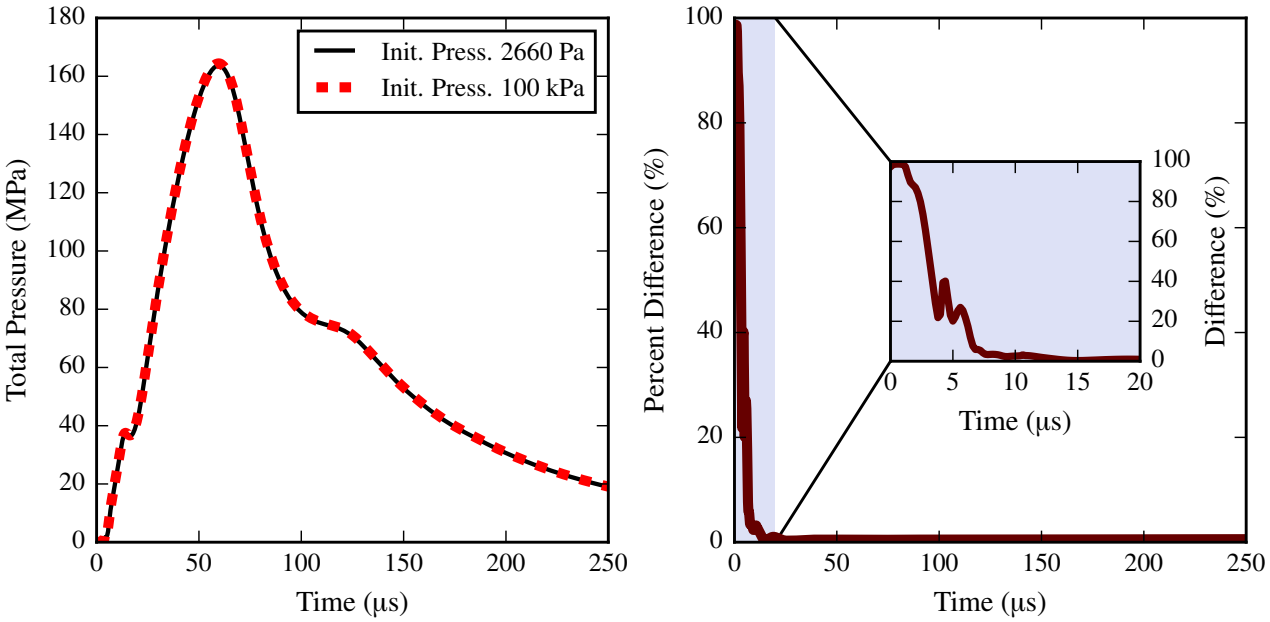

(a) Internal plasma pressure versus time for both initial pressure simulations.

(b) Percent difference in simulated internal pressures from simulations using different initial pressures.

Figure 3.10: Model sensitivity to initial plasma pressure. Both simulations analyzed are of a 10 kA peak current shot. The first and second simulations were initialized at pressures of 2660 Pa and 100 kPa, respectively. The internal plasma pressure is used to investigate the model sensitivity to initial plasma pressure. The internal pressure is taken from the simulation results at the source centerline and 6 cm from the source breech.

pressures attained are much lower than considered here, the sensitivity to initial pressure will be much greater.

3.5 Sensitivity to Inclusion of Neutral Species Viscous Effects

For the simulation results reported in Chapters 4, 5, 6, and 7, the viscosity of the neutral species has been neglected. The viscous and shear module of the THOR simulation code

is undergoing verification and only preliminary results including neutral viscous effects are available. Using these preliminary results, the sensitivity of the simulation model to the inclusion of neutral viscous effects is analyzed in this section.

In order to analyze the sensitivity of the THOR simulation code to the inclusion of neutral viscous effects, a 20 kA peak current pulse was simulated with and without neutral viscous effects included. The time evolution of the neutral species axial velocity distribution over the midpoint of the source is plotted for both simulations in Fig. 3.11. Figure 3.11 indicates that the macroscopic behavior of the neutral species flow is unchanged by the inclusion of neutral viscous effects. Local differences in the simulated velocities are generally below 5%. Percent differences exceeding 5% are mainly caused by the local neutral axial velocity being close to zero and some discharge initialization effects. Naturally, a detailed analysis of the plasma boundary layer would require more attention to the effects of viscosity. However,

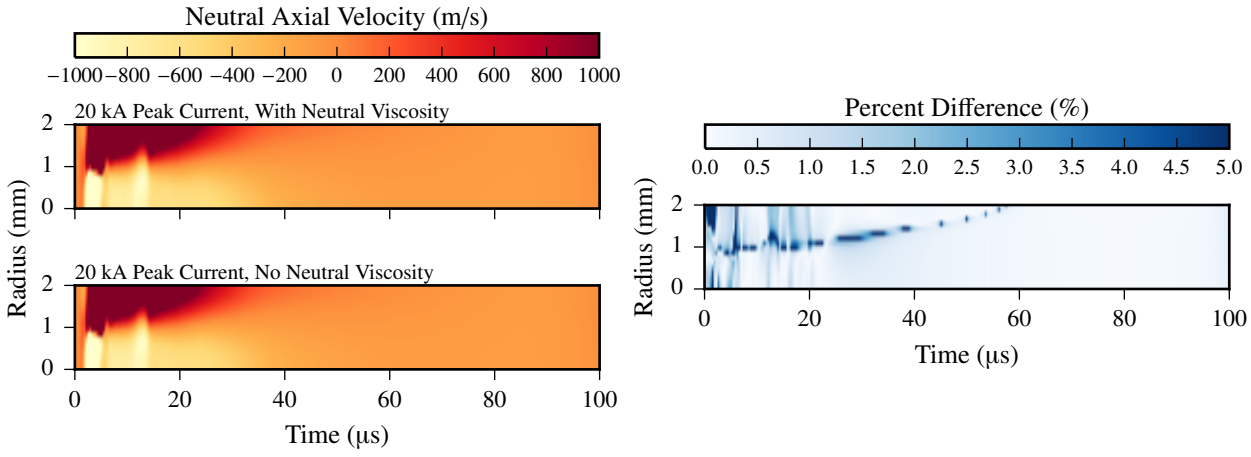

Figure 3.11: Simulation results for an input current shot with nominal peak current of 20 kA. Neutral species axial velocity distribution over the midpoint of the source is plotted versus simulation time. The percent differences in simulation results affected by the inclusion of neutral viscous effects are also shown.

Fig. 3.11 indicates that the general behavior of the flow inside an ET plasma discharge is not sensitive to the inclusion of neutral viscous effects in the simulation.

Chapter 4

Flow Characteristics and Charge Exchange Effects in a Two-dimensional Model of Electrothermal Plasma Discharges

This chapter is a manuscript published in the Journal of Fusion Energy. The final publication is available at Springer via http://dx.doi.org/10.1007/s10894-015-0013-6.
Citation: M. Esmond, A. Winfrey, Flow characteristics and charge exchange effects in a two-dimensional model of electrothermal plasma discharges. J. Fusion Energ. **35**, 244–252 (2016)

4.1 Abstract

Electrothermal (ET) plasma discharges are capillary discharges that ablate liner materials and form partially ionized plasma. ET plasma discharges are generated by driving current pulses through a capillary source with peak currents on the order of tens of kA and pulse

lengths on the order of 100 μs. These plasma discharges can be used to propel pellets into magnetic confinement fusion devices for deep fueling of the fusion reaction, ELM mitigation, and thermal quench of the fusion plasma. ET plasma discharges have been studied using 0D, 1D, and semi-2D fluid models. In this work, a fully 2D model of ET plasma discharges is presented. The newly developed model and code resolve inter-species interaction forces due to elastic collisions. These forces affect the plasma flow field in the source and impede the development of plasma pressure at the exit of the source. In this work, these affects are observed for discharge current pulses peaking at 10 kA and 20 kA.

The sensitivity of the model to the inclusion of charge exchange effects is observed. The inclusion of charge exchange has little effect on the integrated, global results of the simulation. The difference in total ablated mass for the simulations caused by the inclusion of charge exchange reactions is less than one percent. Differences in local plasma parameters are observed during discharge initialization, but after initialization, these differences diminish. The physical reasoning for this is discussed and recommendations are made for future modeling efforts.

4.2 Introduction

Electrothermal (ET) plasma discharges are created by passing high currents (on the order of tens of kA) through a capillary, also called a source. The source dimensions are typically on the order of mm in internal diameter and cm in length. The source liner material

ablates by melting, vaporization, and sublimation and then ionizes to form a partially ionized plasma. Energy is transferred to the source liner material primarily through radiative energy transport [25]. The partially ionized plasma fills the source and is ejected out the open end of the source, entering the exit chamber as a plasma jet. A schematic of an ET plasma source is shown in Fig. 4.1.

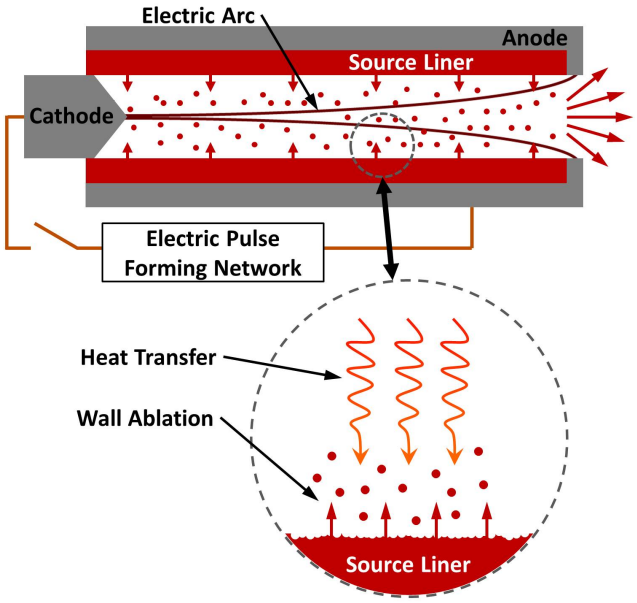

Figure 4.1: Schematic of an ET plasma source. Current flows through the source, and material is ablated from the source liner. The source length is on the order of cm and the source radius on the order of mm. The figure is not drawn to scale.

ET plasma discharges have been used in a wide variety of applications. They have been used to pre-inject plasma armatures into rail guns [48], provide better burn rate control in electrothermal-chemical guns [41,51], and simulate conditions of hard disruption in tokamak fusion reactors [65, 67, 89, 90]. These discharges are also being explored for their potential use as pellet injector systems for deep fueling of tokamak fusion reactors [42, 55–57].

ET plasma discharges have been studied theoretically and numerically. Theoretical studies are neatly summarized in the work of Ruchti and Niemeyer [31]. Time-dependent, numerical simulation of ET plasma discharges was first accomplished by Gilligan and Mohanti using a 0D model [69]. The simulation capabilities were later advanced to 1D, time-dependent models [44, 45]. These models were advanced in the work of Winfrey who studied ideal vs. non-ideal plasma effects inside ET plasma discharges and developed the 1D simulation code ETFLOW [6, 26].

In the study of ET plasma discharges, much attention has been given to the study of the vapor layer separating the ablating surface from the plasma. Hahn modeled the radiation transport through this vapor layer and found that the presence of ablation limited the heat flux and thus acted as a self-shielding mechanism [78, 79]. Eapen and Orton also demonstrated this affect using two-dimensional models of the boundary layer [80, 81]. Eapen expressed the need for a fully 2D model of an ET plasma discharge in order to capture phenomena occurring at the ablating surface and correctly evaluate the heat flux to the capillary wall.

Experimental measurements on ET plasma discharges are difficult due to the harsh environments produced inside these devices. Measurements of the total ablated mass inside these discharges have played an important role in the validation of simulation models [26, 71]. Measurement of the time varying pressure inside ET plasma discharges was accomplished by Powell and Zielinski [44]. Powell and Zielinski found that their 1D simulation model under-predicted the the value of the plasma pressure inside the capillary during an ET dis-

charge. Hamer performed spectroscopic measurements of the plasma jet exiting the capillary of an ET plasma discharge [28]. Hamer verified the assumption of complete dissociation of plasma constituents which is typically made in the modeling and simulation of ET plasma discharges. Hamer also performed bulk velocity measurements on the exiting plasma plume. Echols performed Scanning Electron Microscopy (SEM) and Energy Dispersive X-ray Spectroscopy (EDS) analyses on tungsten samples exposed to the ET discharge plasma [27]. Echols observed a melt layer extending 20 μm into the bulk material with an ablated surface thickness of approximately 4 μm.

In order to advance the understanding of ET plasma discharges and provide more detail on the plasma parameters produced in these devices, a 2D, time-dependent model has been developed. This model is based on a three-fluid description of the partially ionized plasma. The electrons, ions, and neutrals are treated as separate fluids with the necessary coupling terms. The accompanying simulation code is called the Three-fluid, 2D ET Flow Simulator (THOR). THOR is capable of simulating both the capillary source and the exit chamber where the plasma is ejected.

4.3 Model Formulation

THOR simulates the evolution of the electron, ion, and neutral species as three separate fluids in a two-dimensional (axisymmetric) domain. The governing equations for each species are

presented in this section. These governing equations are based on the derivation presented by Meier and Shumlak [17].

4.3.1 Ion Equations

The continuity equation used for the ion species is given by

$$\frac{\partial n_i}{\partial t} + \nabla \cdot (n_i \mathbf{u}_i) = \Gamma_{ion} - \Gamma_{rec} \tag{4.1}$$

where n is the number density, $\mathbf{u}$ is the directed species velocity, Γ_{ion} is the ionization rate, and Γ_{rec} is the recombination rate. The momentum equation for the ion species is

$$\frac{\partial}{\partial t}(m_i n_i \mathbf{u}_i) + \nabla \cdot (m_i n_i \mathbf{u}_i \mathbf{u}_i) = -\nabla P_i + q_i n_i \mathbf{E} + \mathbf{R}_i + \Gamma_{ion} m_i \mathbf{u}_n - \Gamma_{rec} m_i \mathbf{u}_i + \left.\frac{\delta(m_i n_i \mathbf{u}_i)}{\delta t}\right|_{cx} \tag{4.2}$$

where m is the particle mass, P is the species pressure, q is the species charge, and $\mathbf{E}$ is the electric field. The frictional drag force due to inter-species elastic collisions is represented by $\mathbf{R}$. The last term on the right hand side of Eq. (4.2) represents the change in the ion momentum due to charge exchange reactions. The energy equation used for the ion species

is

$$\frac{\partial \varepsilon_i}{\partial t} + \nabla \cdot (\varepsilon_i \mathbf{u}_i) = -\nabla \cdot \mathbf{q}_i - \nabla \cdot (\mathbf{u}_i P_i) + \mathbf{u}_i \cdot (q_i n_i \mathbf{E} + \mathbf{R}_i) + Q_i + \Gamma_{ion} \frac{\varepsilon_n}{n_n} - \Gamma_{rec} \frac{\varepsilon_i}{n_i} - q'''_{rad,i} + \left. \frac{\delta \varepsilon_i}{\delta t} \right|_{cx} \quad (4.3)$$

where $\varepsilon = nC_vT + mnu^2/2$ is the total energy of the species, $\mathbf{q}$ is the conduction heat flow vector, Q is the exchange of internal energy due to inter-species elastic collisions, q'''_{rad} is the radiation loss term, C_v is the species specific heat at constant volume, and T is the species temperature. The last term on the right hand side of Eq. (4.3) represents the change in total energy due to charge exchange reactions.

4.3.2 Neutral Equations

The governing equations for the neutral species are given by

$$\frac{\partial n_n}{\partial t} + \nabla \cdot (n_n \mathbf{u}_n) = \Gamma_{rec} - \Gamma_{ion} \quad (4.4)$$

$$\frac{\partial}{\partial t}(m_n n_n \mathbf{u}_n) + \nabla \cdot (m_n n_n \mathbf{u}_n \mathbf{u}_n) = -\nabla P_n + \mathbf{R}_n - \Gamma_{ion} m_i \mathbf{u}_n + \Gamma_{rec} m_i \mathbf{u}_i + \left. \frac{\delta (m_n n_n \mathbf{u}_n)}{\delta t} \right|_{cx} \quad (4.5)$$

$$\frac{\partial \varepsilon_n}{\partial t} + \nabla \cdot (\varepsilon_n \mathbf{u}_n) = -\nabla \cdot \mathbf{q}_n - \nabla \cdot (\mathbf{u}_n P_n) + \mathbf{u}_n \cdot \mathbf{R}_n + Q_n - \Gamma_{ion} \frac{\varepsilon_n}{n_n} + \Gamma_{rec} \frac{\varepsilon_i}{n_i} - q'''_{rad,n} + \left. \frac{\delta \varepsilon_n}{\delta t} \right|_{cx} \quad (4.6)$$

The symbols used in the neutral equations have the same meaning as the symbols used in the ion equations.

4.3.3 Electron Equations

The electrons are simulated using the drift diffusion approximation. The continuity equation for the electrons is

$$\frac{\partial n_e}{\partial t} + \nabla \cdot (n_e \mathbf{u}_e) = \Gamma_{ion} - \Gamma_{rec} \quad (4.7)$$

The electron momentum equation, by the drift-diffusion approximation, reduces to an equation of state for the electron velocity.

$$\mathbf{u}_e = -\frac{e\mathbf{E}}{m_e \bar{\nu}_{eh}} - \frac{\nabla P_e}{n_e m_e \bar{\nu}_{eh}} \quad (4.8)$$

where e is the elementary charge and $\bar{\nu}_{eh}$ is the averaged momentum transfer collision frequency for electron collisions with heavy particles. The electron energy equation is written in terms of internal energy, and is given by

$$\frac{\partial}{\partial t}(n_e C_v T_e) + \nabla \cdot (\mathbf{u}_e n_e C_v T_e) = -\nabla \cdot \mathbf{q}_e + \frac{1}{\sigma} j^2 + Q_e \quad (4.9)$$

where σ is the plasma electrical conductivity, j is the local current density, and Q_e is the heat transferred to the electrons due to elastic collisions with other species.

4.3.4 Model Closure

Each species is modeled as an ideal gas with constant $C_v = (3/2)k_B$ where k_B is Boltzmann's constant. Plasma transport properties depend on approximations of the average momentum transfer collision frequencies between species. The average electron-neutral momentum transfer collision frequency is given by

$$\bar{\nu}_{en} = n_n v_{avg,e} \bar{Q}_{en} \tag{4.10}$$

where $v_{avg,e} = \sqrt{8k_B T_e/(\pi m_e)}$ is the Maxwellian averaged thermal velocity of the electrons, n_n is the number density of the neutral species, and $\bar{Q}_{en}$ is the Maxwellian averaged momentum transfer cross section for electron-neutral collisions. In this work, $\bar{Q}_{en}$ is evaluated based on a hard sphere approximation. Similarly, the average electron-ion momentum transfer collision frequency is given by

$$\bar{\nu}_{ei} = n_i v_{avg,e} \bar{Q}_{ei} \tag{4.11}$$

where n_i is the number density of the ion species, and $\bar{Q}_{ei}$ is the Maxwellian averaged momentum transfer cross section for electron-ion collisions. $\bar{Q}_{ei}$ is determined according to the recommendations presented by Zaghloul et al. [5].

Thermal conductivities for each species are given by [97]

$$\kappa_k = \frac{5}{2}\frac{n_k k_B^2 T_k}{m_k \bar{\nu}_{kh}} \tag{4.12}$$

where the subscript k indicates the species (e=electrons, i=ions, n=neutrals), and $\bar{\nu}_{kh}$ is the collision frequency between species k and heavy particles, including intra-species collisions. The plasma electrical conductivity, σ, is evaluated from

$$\frac{1}{\sigma} = \frac{1}{\sigma_{en}} + \frac{1}{\sigma_{ei}} \tag{4.13}$$

where $\sigma_{en} = n_e e^2/(m_e \bar{\nu}_{en})$, and $\sigma_{ei} = 1.98 n_e e^2/(m_e \bar{\nu}_{ei})$ [105]. The frictional drag forces and collisional energy exchange terms are also evaluated using the momentum transfer collision frequencies [95, 106].

The electric field is approximated based on Ohm's law: $\mathbf{E} = \mathbf{J}/\sigma$. The current density, $\mathbf{J}$, is evaluated based on the input current pulse. Due to computational constraints, a one-dimensional approximation is used for the electric field, and only its axial component is simulated.

4.3.5 Boundary Conditions

The boundary conditions for the heavy species allow no flux across closed boundaries except in the case of ablation. The temperature at the closed boundary surfaces is not always known, so these surfaces are treated as adiabatic boundaries. The ablation flux is evaluated according to the relationship

$$\phi_n|_{abl} = \frac{q^{"}_{rad,tot}}{H_{sub}} \tag{4.14}$$

where $q^{"}_{rad,tot}$ is the total radiation heat flux reaching the ablating surface, and H_{sub} is the specific sublimation energy required to sublime the source liner material. This ablation model is based on the ablation models used by previous authors [24,26,69]. The total radiation flux, $q^{"}_{rad,tot}$, is approximated using a black body approximation based on the plasma temperature averaged over the geometric cross section of the source. All ablated particles enter the simulation domain as neutral particles.

The boundary conditions for the electron species also allow no flux across closed boundaries except for the cathode and anode boundaries located at the left and right ends of of Fig. 4.1, respectively. At the cathode boundary, the electron flux is directed out of the domain and is given by

$$\phi_e|_{cathode} = -n_e \mu_e E_z \tag{4.15}$$

where μ_e is the electron mobility. The electron flux at the anode boundary is determined in order to preserve global quasi-neutrality. Similar to the heavy species, closed boundaries

are treated adiabatically with respect to electron conduction heat flux. Open boundary conditions are formulated using an extrapolation technique.

4.3.6 Preliminary Verification and Validation

Formal verification of the hydrodynamic module used in THOR has been accomplished by simulating the well known Sod shock tube problem and verifying convergence to the analytical solution. Only a neutral species was used for this verification case. The convergence data is shown in Fig. 4.2. First order, Eulerian methods are used in THOR's hydrodynamic module. Less than first order convergence is observed in the verification results due to the discontinuities in the analytical solution. However, convergence to the analytical solution is demonstrated which verifies THOR's hydrodynamic module.

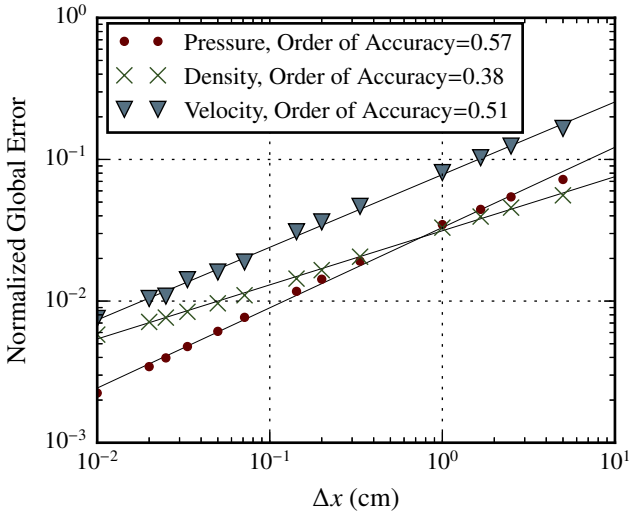

Figure 4.2: Convergence to the analytical solution of the Sod shock tube problem. A neutral species was simulated to verify THOR's hydrodynamic module. The shock tube domain is 100 cm in length.

Validation has been performed by comparing simulation results for the total ablated mass with experimental measurements. The experiments were performed on the Plasma Interaction with Propellant Experiment (PIPE) and the results are reported by Winfrey et al. [26]. The validation data is shown in Fig. 4.3. The THOR simulation code predicts the total ablated mass to be within the experimental uncertainty for shots with peak currents of 20 kA or less. However, for shots with peak currents above 20 kA, the THOR simulation code over predicts the total ablated mass. It is likely that this over prediction is due to the neglect of the vapor shielding mechanism which has been shown to become increasingly important at higher discharge energies [88]. The ETFLOW results account for the vapor shielding mechanism using a variable shielding factor.

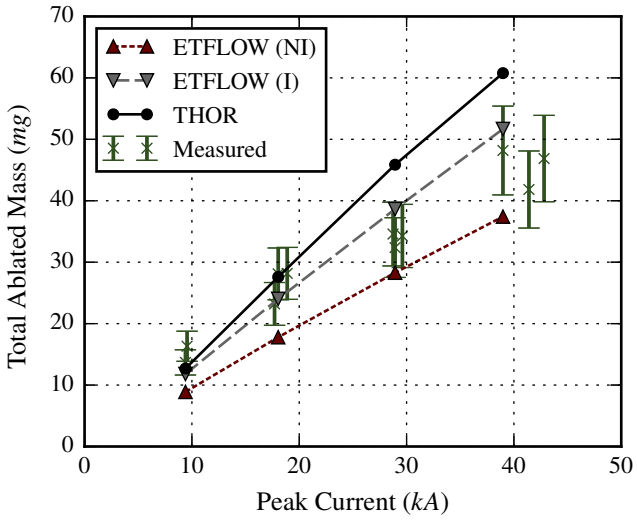

Figure 4.3: Comparison of the total predicted ablated mass with the measured ablated mass. THOR simulation results are compared with experimental measurements and predictions made using the ETFLOW 1D simulation code [26] using both the ideal (I) and non-ideal (NI) models. The experimental uncertainty is approximately 15%.

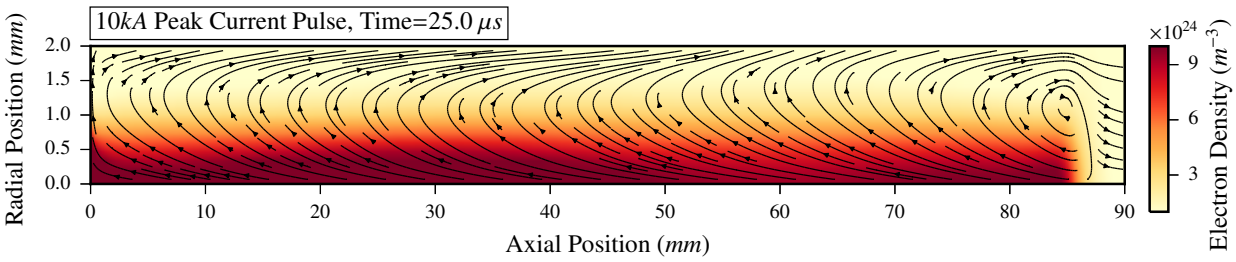

Figure 4.4: Plasma flow inside an ET plasma discharge at a discharge current of 9.4 kA. Streamlines indicate direction of neutral species flow. The electron density distribution is also shown. Results were generated using a structured grid with $\Delta z = 0.3\ mm$ and $\Delta r = 0.13\ mm$.

More detailed measurements of the plasma parameters are difficult due to the harsh environments produced inside ET plasma discharges. Simulation results of the plasma velocity at the exit of the source are consistent with velocity measurements made by Hamer [28].

4.4 Results

In this work, the results from the THOR simulation code are analyzed and observations are made of the two-dimensional flow field that develops inside the plasma source during discharge. In addition, the THOR simulation code has been equipped to simulate the plasma discharge with and without the effects of charge exchange included. This has been done in order to investigate what effect the inclusion of charge exchange reactions has on the results and inform future simulation efforts.

In this work, a capillary source with a 2 mm radius and 9 cm length is simulated. Two different current pulses are simulated. These current pulses have nominal peak currents of 10 and 20 kA. The source liner material used in this study is Lexan polycarbonate. The

governing equations were discretized on a structured grid having $\Delta z = \Delta r = 0.25\ mm$ unless indicated otherwise.

4.4.1 Internal Flow Characteristics

The THOR simulation code evolves the electrons, ions, and neutrals as three separate fluids. The frictional drag forces exerted between the species due to elastic collisions are resolved. As a result, more details of the flow characteristics can be investigated than previously possible.

In Fig. 4.4, the simulation results for the neutral species flow field are shown with the electron density distribution inside the ET plasma source. Figure 4.4 shows that, near the center of the source, the neutral species velocity is directed toward the cathode (closed) end on the left side of Fig. 4.4. At the radial extent of the source, the neutral species is directed toward the source exit where the plasma is ejected into the exit chamber. These flow conditions develop because the electron current flows toward the cathode and induces frictional drag forces on the neutral species. Previous modeling capabilities have not been able to resolve these physical details.

The sensitivity of the neutral axial velocity to the discharge current is illustrated in Fig. 4.5. At high discharge currents, the neutral axial velocity at the source centerline is directed in the negative axial direction (i.e. toward the cathode) over the majority of the source length. As the discharge current recedes, the neutral axial velocity distribution

approaches the typical distribution for compressible flow ejecting from a capillary into a large chamber.

The interactions between the plasma species and the resulting behavior of the velocity distribution affect the pressure rise at the exit of the source. Figure 4.6 shows the time history of the plasma pressure at the exit of the source and at a point internal to the source located 3 cm from the exit. The plasma pressure predicted by the THOR code is compared with predictions from the ETFLOW code. The THOR simulation code predicts peak source exit pressures of 8 and 14 MPa for the 10 and 20 kA peak current pulses simulated, respectively. The ETFLOW simulation code predicts peak source exit pressures of 42 and 96 MPa for the simulated current pulses. These differences in the source exit pressure predicted by these two separate simulation models are due primarily to THOR's inclusion of inter-species

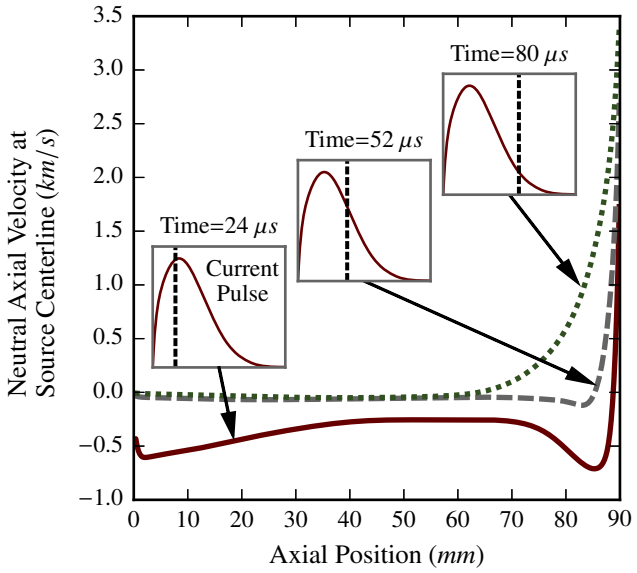

Figure 4.5: Distribution of neutral species axial velocity at the source centerline for various times in a 20 kA peak current discharge simulation. Inset plots indicate simulation time relative to the current pulse.

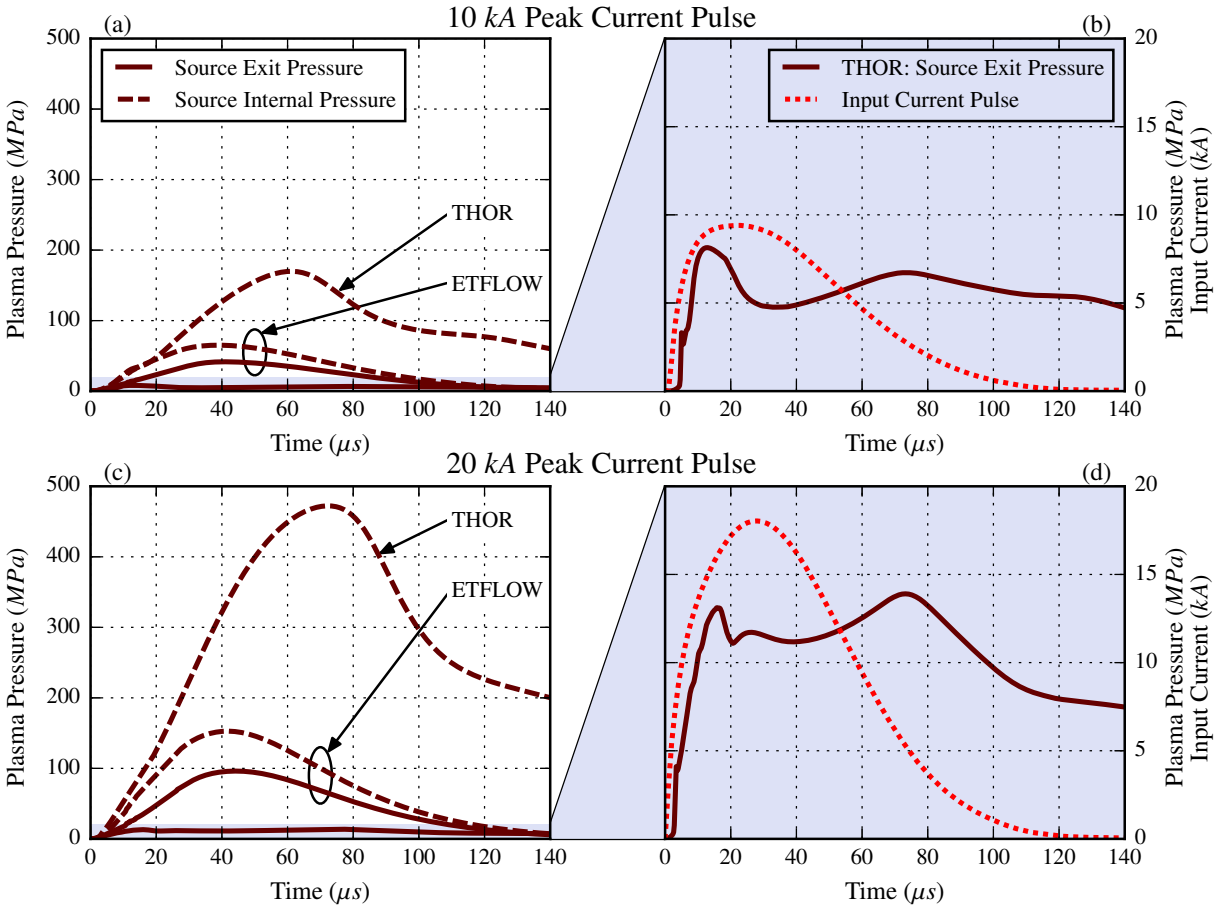

Figure 4.6: ET plasma source pressure time history. The source exit pressure and the source internal pressure are compared for the THOR simulation code and the ETFLOW simulation code in (a) and (c). The source exit pressure predicted by THOR is shown in (b) and (d) along with the current pulse which is an input to the simulation.

collisional drag forces. These drag forces affect the pressure rise at the exit of the source by opposing flow of heavy particles from the source's internal region to its exit. This behavior can be inferred from the plots in Fig. 4.6(b) and (d). These plots show the plasma pressure rise at the beginning of the simulation. However, as the discharge current reaches its peak, the source exit pressure decreases sharply. After the discharge current begins to recede, the source exit pressure rises again as inter-species collisional drag forces subside.

The THOR simulation code predicts peak internal source pressures of 170 and 470 MPa for the 10 and 20 kA peak current pulses simulated, respectively. The ETFLOW simulation code predicts peak internal pressures of 65 and 150 MPa for the simulated current pulses. These differences are due to each simulations sensitivity to the source exit pressure. ETFLOW predicts higher exit pressures which allows for more mass ejection from the source since the flow of plasma is choked at the source exit. However, there is less mass ejected in the case of the THOR simulation due to lowered source exit pressure. This causes a larger internal source pressure for the THOR simulation compared with ETFLOW.

4.4.2 Charge Exchange

The charge exchange terms in THOR's governing equations are outlined by Meier and Shumlak [17]. The charge exchange cross section is approximated using the fit formula presented by Janev and Smith [107] for hydrogen atoms. The THOR simulation code was run for the 10 kA and 20 kA peak current pulses. Both current pulses were simulated with and

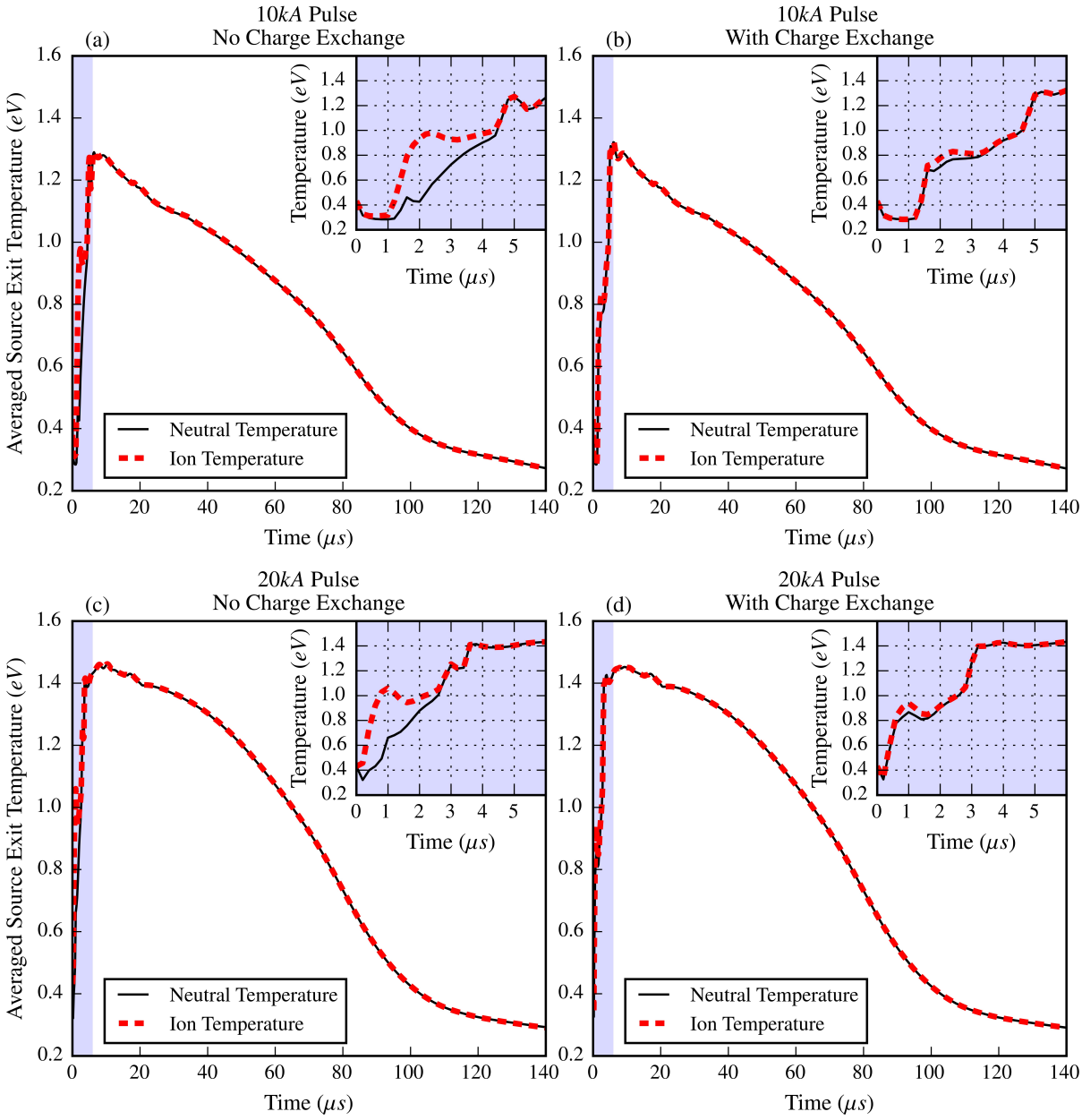

Figure 4.7: Comparison of the ion and neutral species temperatures averaged over the source exit for 10 and 20 kA peak current pulse simulations. (a) and (c) show simulation results where charge exchange effects are neglected, and (b) and (d) show results where they have been included.

without charge exchange reactions included. The averaged source exit temperatures for the ion and neutral species are shown for these four simulations in Fig. 4.7. During discharge initialization, shown in the inset plots in Fig. 4.7, the inclusion of charge exchange is shown to cause the ion and neutral temperatures to equilibrate much faster compared to when charge exchange is neglected. When charge exchange is neglected, the ion temperature at the source exit exceeds the neutral temperature by up to 0.5 eV. With charge exchange reactions included, the maximum difference in the ion and neutral temperatures is 0.08 eV at the source exit. After discharge initialization, the neutral and ion temperatures are essentially the same and represent the plasma temperature. The maximum percent difference in plasma temperature at the source exit caused by the inclusion of charge exchange effects is 1.5% after discharge initialization.

4.5 Discussion and Conclusions

A simulation model and code have been developed to investigate ET plasma discharges in greater detail than previously possible. The model and code include the effects of inter-species elastic collisions. In addition, the effects of charge exchange can be included in the simulation.

The flow of the plasma inside the capillary discharge is affected by inter-species drag forces resulting from elastic collisions. These forces cause the heavy plasma species to be entrained in the flow of electrons flowing away from the source exit near the axis of the

capillary (see Fig. 4.4). Near the source exit, the collisional drag forces impede the build up of plasma pressure. These effects are illustrated in Fig. 4.6. These pressure characteristics at the source exit may affect the performance of these devices when utilized as pellet launchers.

The effects of the inclusion of charge exchange reactions in the simulation have been isolated. The charge exchange reaction terms act to equilibrate the ion and neutral species' velocity and temperature. This process is also accomplished by elastic collisions occurring between the ion and neutral species. The equilibration time constants for these two processes can be determined from their respective cross sections and characteristic velocities. The characteristic velocity for elastic collisions is based on the thermal velocity of the neutral and ion species. From this data, the equilibration time constants, based on exponential decay to equilibrium, for both charge exchange reactions and elastic collisions are evaluated and compared in Fig. 4.8. ET plasma discharges are typically initialized at pressures on the order of kPa. Typical pressures reached inside ET plasma discharges range up to hundreds of MPa. Figure 4.8 highlights the low pressure initialization and high pressure operation regions and shows that for low pressures, the equilibration time constant for elastic collisions is on the same order of magnitude as the macroscopic time scale. This explains the differing ion and neutral temperatures in the first 6 μs of the simulation as shown in Fig. 4.7 for simulations where charge exchange is neglected. With the inclusion of charge exchange reactions, Fig. 4.8 shows that the equilibration time constant is less than the macroscopic time scale. The combined effect of elastic collisions and charge exchange causes the ion and

neutral temperatures to equilibrate more quickly. This is also illustrated in Fig. 4.7 for the simulations including charge exchange reactions compared to those that do not.

Maximum percent differences between computed results using charge exchange reactions versus neglecting charge exchange reactions is shown in Fig. 4.9. The maximum percent difference in simulated plasma parameters observed over the full simulation is 38%. As discussed previously, these large differences occur during discharge initialization and are caused by faster equilibration of the ion and neutral species at the beginning of the simulations when charge exchange is included. After a simulation time of 6 μs, the maximum observed percent difference in simulated plasma parameters is only 3%. This indicates the sensitivity of ET plasma discharge simulations to the inclusion charge exchange reactions for typical operating conditions. Percent differences are generally lower for the 20 kA peak current

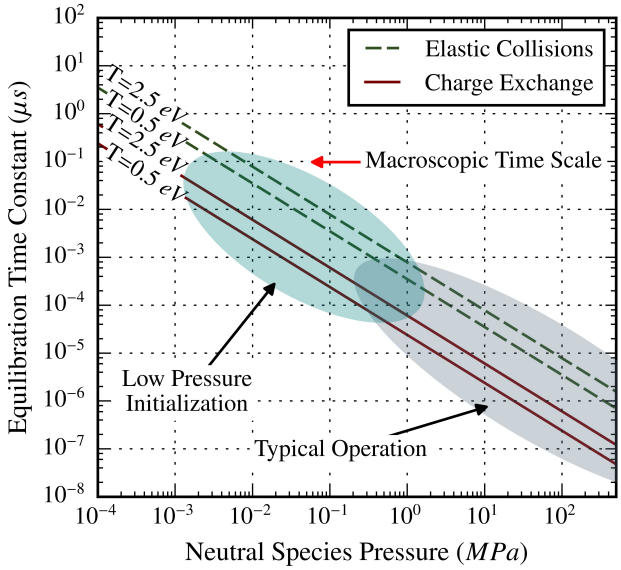

Figure 4.8: Equilibration time constants for ion and neutral species equilibration. Equilibration time constants are shown for elastic collisions and charge exchange reactions. Initialization and typical operation regions for ET plasma discharges are highlighted.

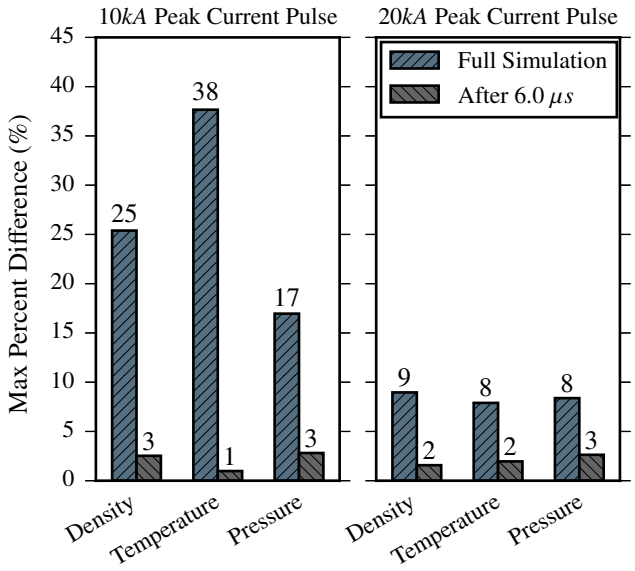

Figure 4.9: Maximum percent differences in computed results caused by the inclusion of charge exchange reactions in the THOR code. Percent differences are computed at an axial position of 6 cm measured from the cathode and at the centerline of the ET source. The maximum percent differences for the whole simulation are shown and compared to the maximum percent differences observed after 6 μs, or after discharge initialization.

pulse than for the 10 kA peak current pulse because higher operating pressures are reached more quickly in the former case.

The THOR model and simulation code have been used to gain further insight in the operation and modeling of ET plasma discharges. It has been shown that charge exchange effects are more important at lower pressures and for smaller macroscopic time scales. For typical operating pressures ($\sim MPa$) and macroscopic time scales ($\sim 0.1\mu s$) in ET plasma discharges, the inclusion of charge exchange effects causes a difference in simulated plasma parameters of approximately 3% using the model presented in this work. In addition, the results from the THOR model and code indicate that inter-species collisional drag forces impede the development of plasma pressure at the source exit. This phenomenon can be

important in predicting the performance of these devices in pellet injector systems as well as other applications that rely on exit pressure.

Chapter 5

Two-Dimensional, Three-Fluid Modeling of Capillary Plasma Discharges in Electrothermal Mass Accelerators

This chapter is a manuscript published in the Journal of Physics D: Applied Physics. The final publication is available at online at http://dx.doi.org/10.1088/0022-3727/49/21/215202.
Citation: M. Esmond, A. Winfrey, Two-dimensional, three-fluid modeling of capillary plasma discharges in electrothermal mass accelerators. J. Phys. D: Appl. Phys. **49**, 215202 (2016)

5.1 Abstract

Electrothermal (ET) plasma launchers have a wide array of applications as mass acceleration devices. An ET plasma launcher utilizes an ET plasma discharge to accelerate a projectile. ET plasma discharges are arc-driven capillary discharges that ablate liner ma-

terials and form partially ionized plasmas. ET plasma discharges are generated by driving current pulses through a capillary source. Current pulses typically have peak currents on the order of tens of kA with pulse lengths on the order of hundreds of µs. These types of plasma discharges have been explored for their application to military ballistics, electric thrusters, and nuclear fusion power. ET plasma discharges have been studied using 0D, 1D, and semi-2D fluid models. In this work, a three-fluid, fully two-dimensional model of ET plasma discharges is presented. First approximations used in the newly developed model and code are discussed and simulation results are compared with experiment. Simulation results indicate the development of back flow inside ET plasma discharges due to collisional drag forces between individual plasma species. This back flow is observed for simulations of ET plasma discharges receiving current pulses with peak currents of 10, 20, 30, and 40 kA. Simulation results also reveal the development of fluid perturbations near the breech of the plasma source. These perturbations cause variations in the plasma electrical conductivity and ultimately cause changes in the local ablation rate of the source liner. At higher current pulses, these perturbations are more localized in the region of the source closest to the breech. This effect causes a decrease in the ablated mass in this region relative to the region of the source experiencing the highest ablation.

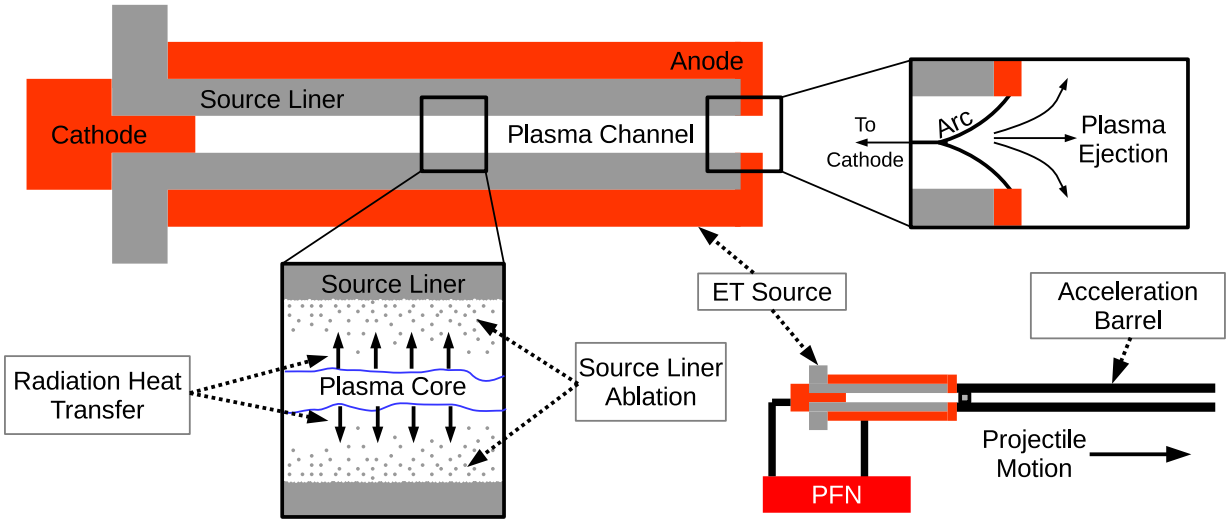

Figure 5.1: Schematic of an ET plasma source with additional components. A pulse forming network (PFN) is used to drive an electric current pulse through the ET source. Electric current flows from the cathode end to the anode end. A plasma core forms and radiant heat transfer induces ablation of the source liner material. The plasma is ejected out the open end of the source into an acceleration barrel. This figure is not drawn to scale.

5.2 Introduction

Electrothermal (ET) plasma discharges are created by passing high currents (on the order of tens of kA) through a capillary, also called a source. The source dimensions are typically on the order of millimetres in internal diameter and centimetres in length. The source liner material ablates by melting, vaporization, and sublimation and then ionizes to form a partially ionized plasma. Energy is transferred to the source liner material primarily through radiative energy transport [25]. The partially ionized plasma fills the source and is ejected out the open end of the source, entering an acceleration barrel. A schematic of an ET plasma source is shown in Fig. 5.1.

ET plasma discharges have been used in a wide array of applications. These discharges have been used to pre-inject plasma armatures into rail guns [46, 48]. The plasma armatures produced by an ET plasma discharge provide a means of control over the properties of the armature and mitigation of ablation in the rail gun. Electrothermal-Chemical (ETC) guns have used ET plasma discharges to provide better burn rate control of solid propellants in ballistic devices [41, 51]. The electrothermal ignition of the solid propellants in ballistic devices has been shown to require shorter and more consistent ignition delay times compared with conventional ignition. ET plasma launchers may prove to be a valuable means of pellet injection in tokamak fusion reactors. ET plasmas can be used to accelerate pellets to velocities needed for deep fueling of fusion reactors and also can be used to launch pellets at a sufficient frequency for pellet pacing in tokamak fusion reactors [42, 55–57]. These devices can also be used to simulate the high heat flux conditions that are expected in tokamak fusion reactors [65, 67, 89, 90]. ET plasma discharges have also been explored for use as plasma thrusters in space applications [38, 39].

Theoretical exploration and analysis of ET plasma discharges can be traced back to [32] and [29]. Theoretical studies are neatly summarized by Ruchti and Niemeyer [31]. Numerical, semi-analytical analysis of ET discharges was performed by Kovitya and Lowke [30]. Time-dependent numerical simulation of ET plasma discharges was first undertaken by Gilligan and Mohanti [69] using a 0D model. Their model solved the equations of continuity and energy, and their ablation/radiation model was based on a black-body description of the plasma and relied on a variable radiation shielding parameter. This shielding parameter accounted for the

radiation heat flux to the ablating surface that is blocked by the presence of ablated material. This shielding parameter is often called the vapor shield factor. Later advancements to these simulation models included advancement to 1D, time-dependent simulations [44, 45]. These authors solved the equations of continuity, momentum, and internal energy. Hurley *et al.* paid close attention to the formulation of the internal energy equation; he incorporated ionization energy and sublimation energy. Hurley *et al.* also utilized an adaptive vapor shield factor to account for the vapor layer that forms between the ablating surface and the plasma core. One-dimensional simulation capabilities were later advanced by [98] and [6]. These authors developed a semi-2D model of an ET plasma source. This model relied upon the numerical solution of the 1D governing equations of continuity, momentum, and energy. A radial energy equation was then used to approximate radial gradients inside the plasma source.

The simulation and modeling capabilities available for pulsed ET plasma discharges have previously been limited to 0D, 1D, and semi-2D models. It has been noted by [80] that a fully-2D model is needed in order to capture phenomena occurring at the ablating surface and correctly evaluate the heat flux to the capillary wall. Fully-2D simulations relevant to ET plasma discharges have been limited to steady-state analyses [86] and models of the plasma boundary layer [80, 81] which have not fully captured the plasma-fluid dynamics involved in ET plasma discharges. A new model and code have been developed to address this need for fully-2D simulation capabilities of pulsed ET plasma discharges.

This new model and code is called the Three-fluid, 2D ET Plasma Flow Simulator (THOR). THOR represents the first step in fully-2D, time-dependent simulation of ET plasma discharges. THOR has been developed as a computational framework to capture significantly more relevant details involved in ET plasma discharges than previously possible. THOR captures radial gradients inside ET plasma discharges which can provide valuable insight into the ablation processes occurring at the ablating surface boundary, a topic which has been the subject of considerable study [24, 33]. THOR has the capability of including charge exchange effects which have been shown to be more important for discharges at lower pressures (tens of kPa) and shorter pulse lengths ($\sim\mu$s) [108]. THOR simulates the three plasma species (ions, neutrals, and electrons) with independent temperatures. It therefore has the potential to capture certain phenomena arising from thermal non-equilibrium effects. Simulations of similar devices have been shown to have significant differences from thermal equilibrium simulations when thermal non-equilibrium is included [18].

In this work, the underlying fluid models for the three plasma constituents are briefly described. A first approximation for the electric field currently utilized in the simulation code is presented and discussed. This approximation facilitates simulation of the macroscopic fluid behavior inside ET plasma discharges. Simulation results are compared with experiment and analyzed. Analysis of simulation results focuses on emergent fluid behavior of the plasma inside ET plasma discharges. It should be noted that only simulation results for the ET plasma source have been reported in this work. Simulation of the acceleration barrel has been put off to later date.

5.3 Model Formulation

The THOR model and code uses three sets of governing equations to simulate the ion, neutral, and electron species in a two-dimensional, axisymmetric domain. The governing equations used in the model are based on the derivation presented by Meier and Shumlak [17]. The THOR model equations have been presented previously by Esmond and Winfrey [108] and are briefly described in this section. THOR simulates the evolution of the electrons using the drift-diffusion approximation and simulates the ion and the neutral species using separate sets of the Euler gas-dynamic equations with thermal conduction included in the energy equations. Radiation heat transfer from the plasma to the ablating surface is approximated using a black-body radiation approximation. The plasma species interact through ionization, recombination, collisional drag, and collisional heat exchange. In this work, the effects of charge exchange have been neglected as their inclusion is not expected to alter simulation results by more than a few percent [108]. Relations used for the plasma transport properties and collision terms have been presented previously [108]. The ionization and recombination rates are determined using coefficients from the literature [1, 96].

Due to computational constraints, the full solution of Maxwell's equations has been put off to a later date. The induced magnetic fields inside these devices have been shown to be negligible [6]. Only the electric field components are needed for the simulation. For the simulation results presented in this work, a first approximation to the electric field has been utilized. From the simulated plasma composition, the plasma electrical conductivity can be

computed as discussed by Esmond and Winfrey [108]. From the plasma conductivity, the electric field can be approximated using Ohm's law.

$$\mathbf{E} = \mathbf{J}/\sigma \tag{5.1}$$

where $\mathbf{E}$ is the electric field, $\mathbf{J}$ is the current density, and σ is the plasma electrical conductivity. The current density is determined from the input current pulse. The current is assumed to be uniform throughout the ET source which is reasonable given the geometry of the problem. The current density is then only a function of time and has only an axial component. The relation for the electric field then reduces to

$$\mathbf{E} = E_z(z,t) = \frac{J(t)}{\sigma_{eq}(z,t)} \tag{5.2}$$

where $J(t)$ is the axial current density at time t determined from the input current pulse, and σ_{eq} represents the equivalent resistance of the plasma at an axial location, z. As discussed in Sec. 5.5, this approximation yields physical and realistic results that show reasonable agreement with experimental measurements.

5.4 Model Verification

The THOR simulation code utilizes a first order, scalar-dissipative technique in order to simulate the fluid dynamics [92]. The fluids module of the THOR simulation code has been

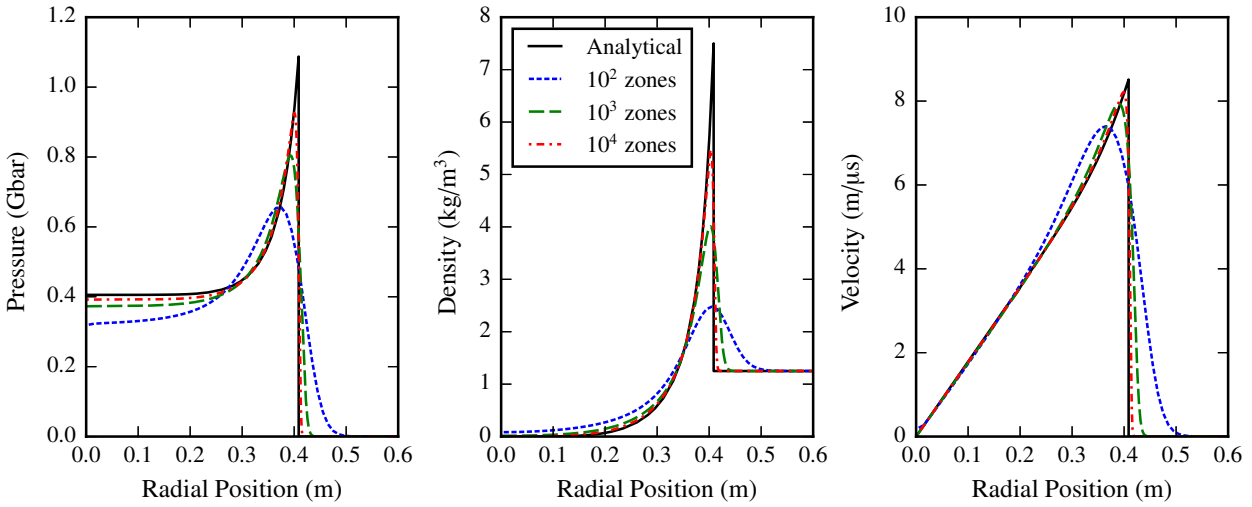

Figure 5.2: Convergence to the Sedov blast wave test problem in cylindrical coordinates for a single neutral species simulated using the fluids module of the THOR simulation code. The domain length is 1 m, the blast energy simulated is 1.85×10^{13} J/m in the cylindrical geometry. The factor α used in Ref. [102] was set to $2/3\pi$ in this work to account for the geometry. The output time is 0.02 μs.

verified against two well-known gas dynamic test problems. To verify the fluids module of the THOR simulation code, the Sod test problem was simulated in the axial direction, and the Sedov test problem was simulated in the radial direction. A single neutral species was simulated in each test problem to compare results with the analytical solution. The convergence results for the Sod test problem have been presented elsewhere [108].

Qualitative convergence to the analytical solution was observed for the Sedov test problem [102]. This test problem involves a blast wave propagating from the center of the domain outward. The direction of propagation for this verification study was in the radial direction inside the cylindrical geometry. The convergence to the analytical solution is shown in Fig. 5.2. The fluids module of the THOR simulation code demonstrates convergence to the analytical solution, and the fluids module used in the THOR code is verified.

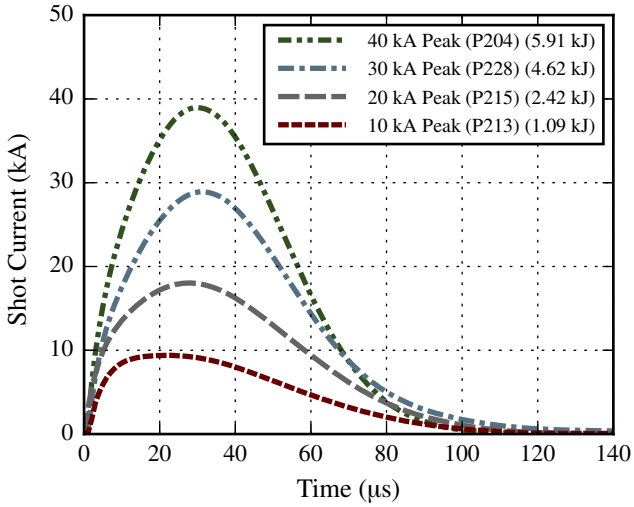

Figure 5.3: Selected experimentally measured current pulses from the Plasma Interaction with Propellant Experiment (PIPE) reported by Winfrey *et al.* [26]. The measured current pulses are used as simulation inputs to the THOR code. The legend indicates nominal peak current, PIPE shot identifier, and energy deposited in the experimental system during discharge.

5.5 Model Validation

Experimental measurements of the total ablated mass inside ET plasma discharges have played a vital role in the validation of simulation models in the past. Recent experimental results have been reported by Winfrey *et al.* [26]. In their work, Winfrey *et al.* focus on a range of experimental current pulses performed with the Plasma Interaction with Propellant Experiment (PIPE). These current pulses range from nominally 10 to 40 kA in peak current. All pulses have an active pulse length of approximately 100 μs. Four current pulses have been selected from this range to use in the present work. These current pulses are shown in Fig. 5.3. The THOR simulation code was used to simulate the four current shots shown in Fig. 5.3. The results for the total ablated mass are compared to experimentally measured

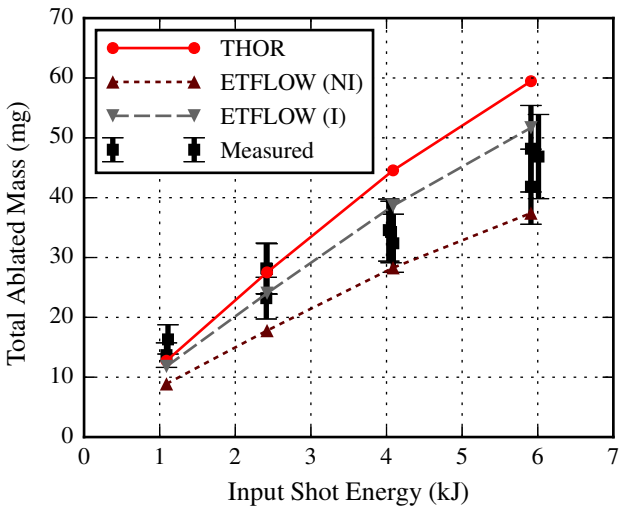

Figure 5.4: Simulation results are compared with experimental results for the total ablated mass inside ET plasma discharges for varying current shots. ETFLOW simulation results as well as results generated with THOR are shown. ETFLOW results include predictions made with the ideal(I) and nonideal(NI) conductivity models. The experimental uncertainty is approximately 15%. All THOR simulations were run to a simulation time of 250 µs. Experimental results and ETFLOW simulation results have been reported previously [26].

values as well as predictions made using the 1D simulation code, ETFLOW [26]. These comparisons are made in Fig. 5.4. ETFLOW has been widely used and is shown to achieve good agreement with the measured data especially in the case of the ideal conductivity model. The THOR simulation results over-estimate the ablated mass in the cases where greater than 3 kJ of input energy is used. This over-estimation is attributed the fact that THOR does not explicitly include a vapor shielding mechanism. The vapor shielding mechanism has been shown to become more important at higher input energies [88]. Good agreement is observed between experiment and the THOR simulation results for input shot energies less than 3 kJ.

Further validation of the present model is accomplished by comparing the measured electrical conductivity of the ET plasma source with that predicted by the THOR simulation

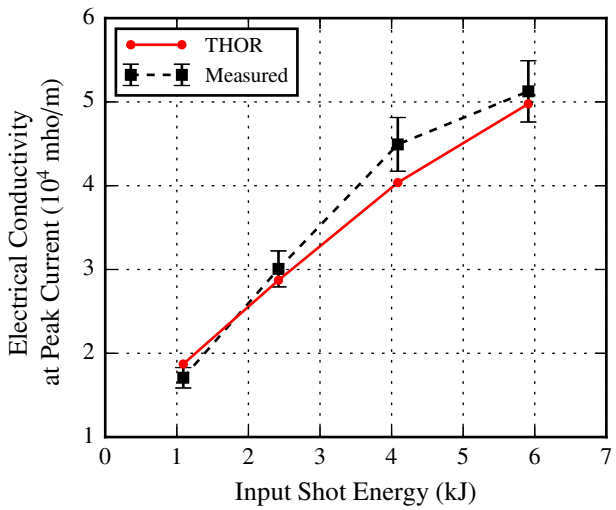

Figure 5.5: Electrical conductivities (measured and predicted) of the ET plasma source at time of peak current.

code. The electrical conductivity measured at the time of peak current in the PIPE shots is shown in Fig. 5.5. The THOR simulation values corresponding to these measurements are also shown.

The time varying electrical conductivity was measured for the PIPE shots. The simulated and measured time-varying electrical conductivities for four current shots are shown in Fig. 5.6. The uncertainties plotted in Fig. 5.6 and Fig. 5.5 represent measurement uncertainties. It should be noted that the measurements were taken over the entire electrical system while simulation results are only representative of the plasma domain. Naturally this introduces some small systematic error due to stray currents and minor electronic phenomena. This error is not readily quantifiable and does not affect results and is noted here for completeness.

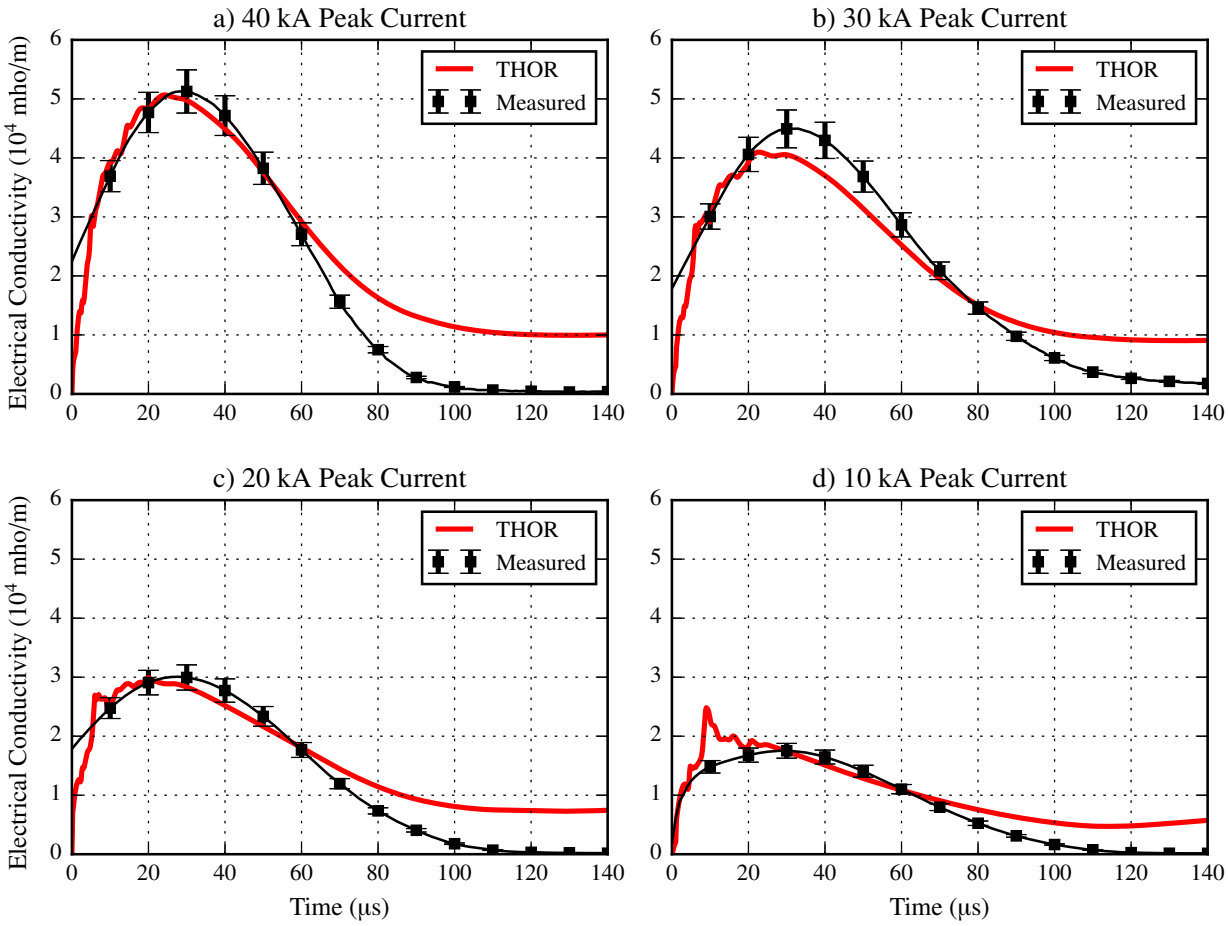

Figure 5.6: Simulation results from the THOR code for the total electrical conductivity of the ET plasma source during discharge. Measured values are also shown with measurement uncertainty.

As the current pulse dissipates (i.e. at a simulation time above 80 µs) the simulated electrical conductivity over-predicts the measured electrical conductivity. During this time, the discharge is undergoing significant recombination effects. It is clear from Fig. 5.6 that the THOR simulation code is lacking in its ability to capture these particular physics. The authors are considering possible improvements to the simulation code in order to enhance its ability to correctly capture these phenomena. However, these recombination effects are not expected to greatly influence the fluid dynamics involved in the simulation and discussed here. Other than these discrepancies near the end of the discharge, the predicted shapes of the electrical conductivity match the measured shapes very well. The predicted peak values of electrical conductivity of the ET plasma source are very close to those measured as shown in Fig. 5.5.

Simulated values for the electric field are consistent with measurements performed by [32]. The measured data taken by Niemeyer is shown with simulated results from the THOR simulation code in Fig. 5.7. For the present work, the THOR simulation code has been used with Lexan, or $(C_{16}H_{14}O_3)_n$, as the source liner material. This material is similar in composition to those used by [32]. The predicted electric field values correspond very well to the trends discovered by Niemeyer. This provides further validation of the THOR model and code.

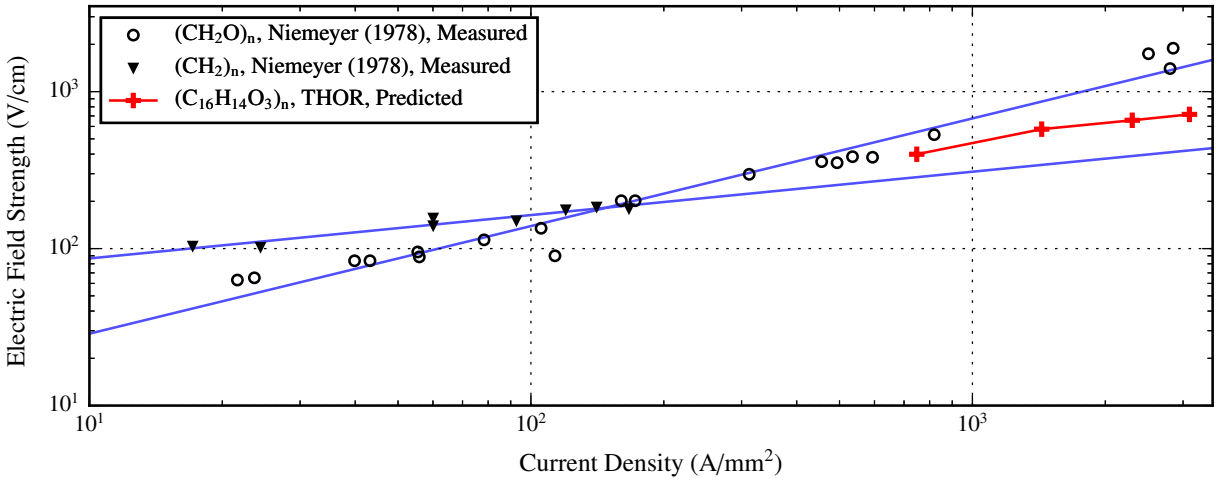

Figure 5.7: Measured values for the electric field strength as a function of current density. Different materials are represented. Measured data taken by [32]. THOR simulation results shown at time of peak current at an axial position along the source of 6 cm from the cathode (closed) end of the source.

5.6 Model Results

The THOR simulation model and code have been used to simulate four different current pulses. These current pulses have been measured experimentally and are shown in Fig. 5.3. These current pulses were performed on the Plasma Interaction with Propellant Experiment (PIPE). Experimental results from this device are reported by Winfrey *et al.* [26]. For the simulation results presented in this work, Lexan polycarbonate has been used as the source liner material. The geometry of the source was held constant with a 2 mm radius and 9 cm length. For each simulation, a mesh with $\Delta z = 0.25$ mm and $\Delta r = 0.11$ mm was used.

In order to illustrate the two-dimensional flow patterns that develop inside ET discharges as predicted by the THOR simulation code, the results from a 30 kA peak current pulse simulation are shown in Fig. 5.8. The two-dimensional flow patterns predicted by THOR

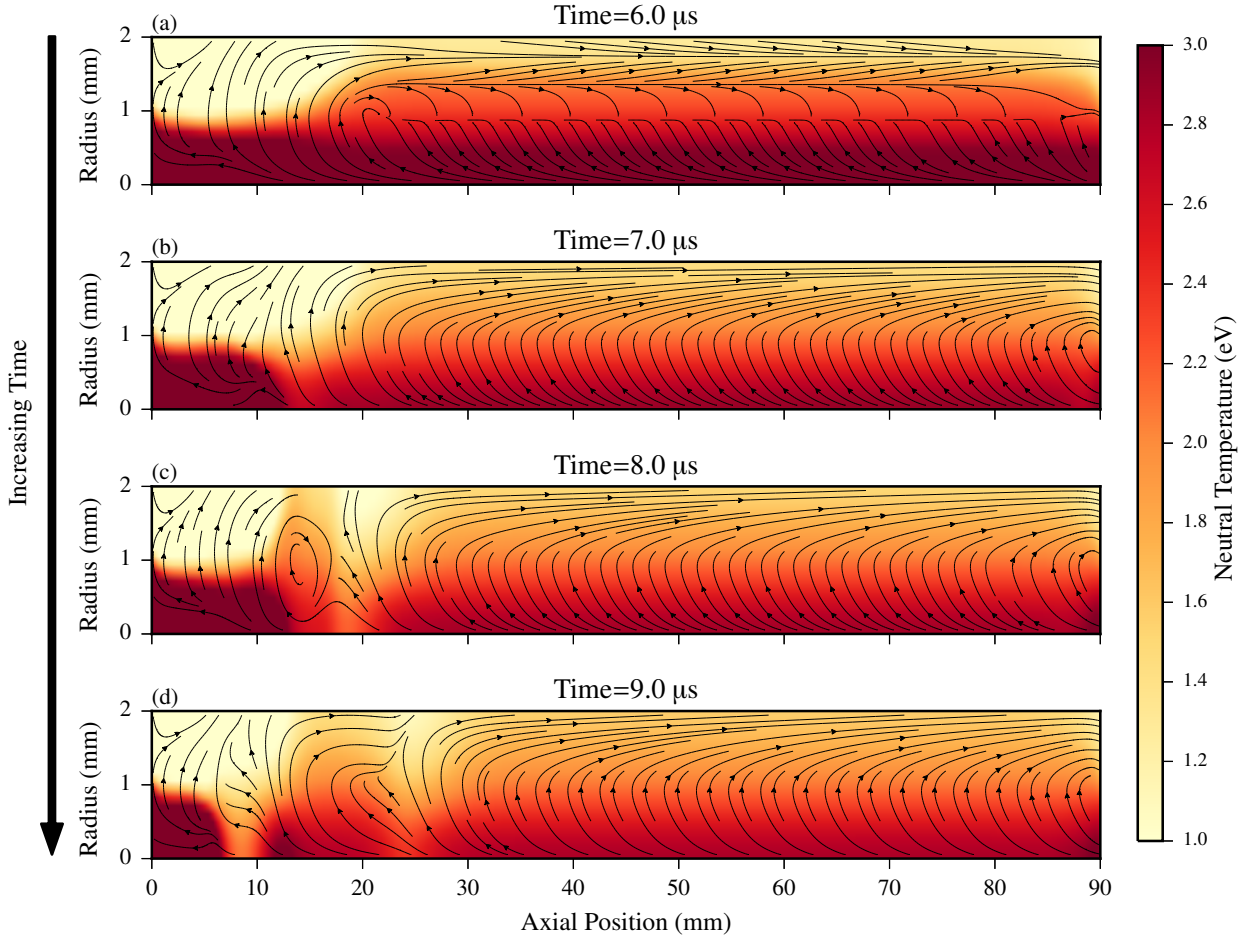

Figure 5.8: Two-dimensional flow patterns inside an ET plasma discharge with current pulse peaking at 30 kA. Streamlines indicate neutral species flow direction which is representative of plasma flow. The neutral temperature distribution is also shown. The source centerline is at the bottom of each plot. The cathode (closed) and anode (open) ends are on the left and right of each plot, respectively. Simulation times are (a) 6μs, (b) 7μs, (c) 8μs, and (d) 9μs.

show the development of two zones inside the capillary. One zone develops at the source centerline and involves plasma-fluid flow in the negative axial direction toward the cathode (closed) end of the source. The second zone develops near the radial wall of the source and is characterized by the plasma-fluid moving toward the anode (open) end and exiting the source. Near the cathode end of the source, the plasma flow from the centerline is redirected into the near-wall region. This redirection of the flow causes convective mixing of more energetic particles coming from the source centerline with the cooler plasma fluid near the ablating surface. This mixing causes changes in the plasma transport properties and drives fluid-dynamic perturbations near the cathode end of the source. These effects are observed for each of the current pulses simulated.

The development of a centerline and a near-wall zone inside of the ET plasma discharge is due to the interaction between the electron species and the heavy species. The electrons are driven toward the cathode end of the source by the electric field. The electron density and plasma temperature are higher near the centerline of the source due to colder, ablated neutral particles entering at the radial wall. The electrons interact with the heavy species via elastic collisions. The elastic collisions induce a frictional drag on the heavy species and cause a back flow of heavy species toward the cathode. Eventually the heavy species are redirected into the near-wall region and are ejected once they reach the anode end of the source.

The effects of this back flow are illustrated in Fig. 5.9 by showing the time evolution of the radial distribution of the neutral species velocity over time. The radial distributions

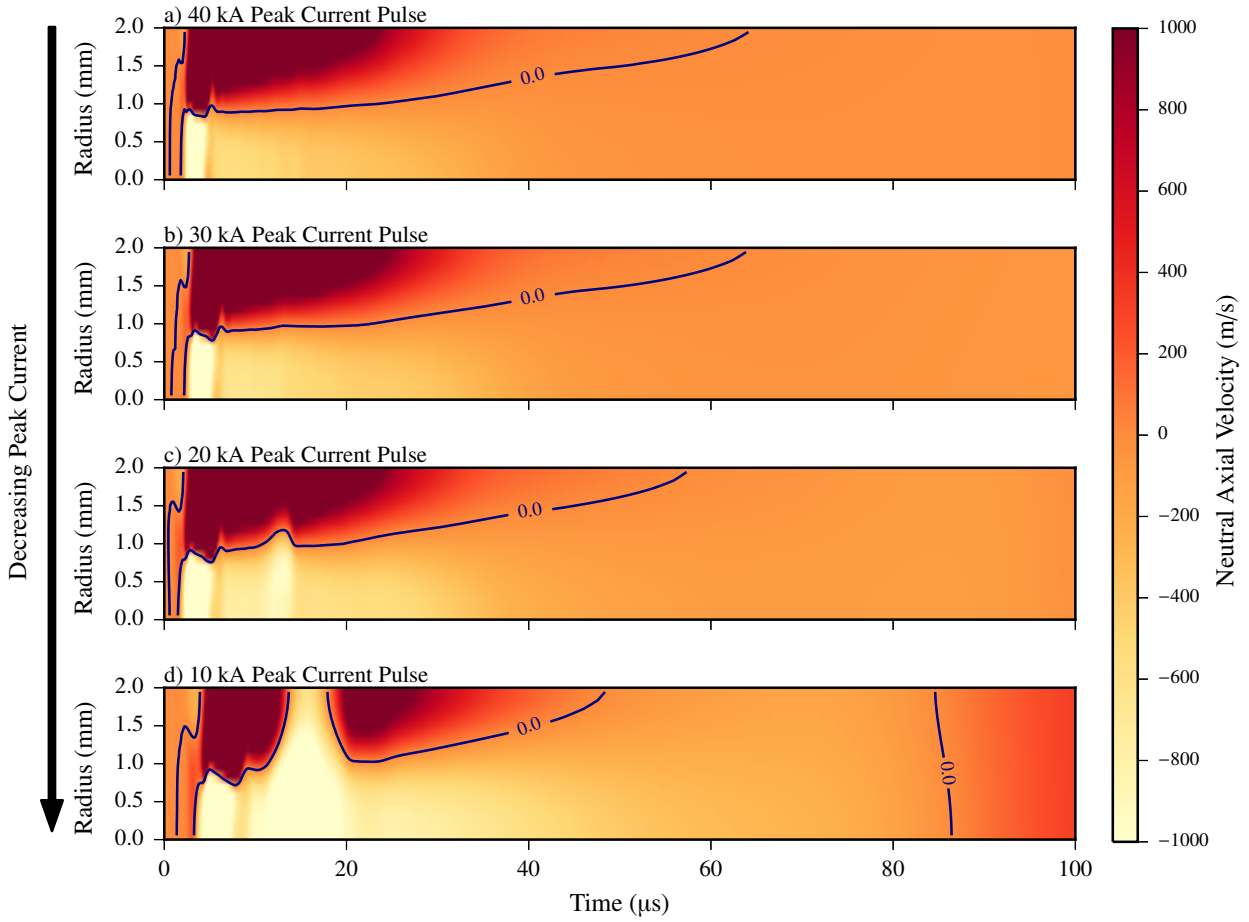

Figure 5.9: Time variations of the radial distribution of the neutral species axial velocity. Radial distributions are shown only at the midpoint of the source and are plotted up to a simulation time of 100 μs. Results are plotted for the (a) 40 kA, (b) 30 kA, (c) 20 kA, and (d) 10 kA peak current pulses.

at the midpoint of the source are shown (i.e. $z = 4.5$ cm measured from the cathode). Contour lines on Fig. 5.9 indicate sign changes in the neutral species axial velocity. The neutral species is the predominant species, and its axial velocity is representative of the heavy species axial velocity. Figure 5.9 illustrates further the development of the plasma back flow and the centerline and near-wall zones. It is observed that the distinction between the two zones is strongest during the beginning of the discharge when the discharge current is

increasing. Eventually the velocity becomes relatively uniform over the source cross section at its midpoint. It is also observed that, for the 10 kA peak current pulse, the typical behavior of the velocity distribution at the source midpoint is interrupted by a brief period of negative axial velocity over the entire source cross section. This phenomena occurs at a simulation time of 15 µs. This interruption in the behavior of the velocity is caused by the propagation of the fluid-dynamic perturbations, similar to those observed in Fig. 5.8, down the length of the source eventually reaching its midpoint, which is shown in Fig. 5.9.

It has been shown that the THOR simulation code predicts the development of fluid-dynamic perturbations that originate at the cathode end of the source. These perturbations are caused by plasma back flow inside the source and the resultant convective mixing of the plasma near the cathode end of the source. These perturbations influence the plasma transport properties and cause temporal and spacial variations in the plasma parameters inside the ET plasma discharge. These variations in the plasma parameters affect the ablation rate inside the source. The time variation in the local ablation rates inside the source is shown in Fig. 5.10. Figure 5.10 illustrates how the ablation rate is affected by the fluid-dynamic perturbations near the cathode (i.e. left) end of the source. These types of discharges are often referred to as ablation controlled arcs because of the stabilizing role that ablation plays. As larger currents are applied to the source, Fig. 5.10 indicates the expected rise in ablation rates. Figure 5.10 also illustrates the stabilizing effects of higher ablation rates. As larger currents are applied in the source, the variations in the ablation rate become more localized

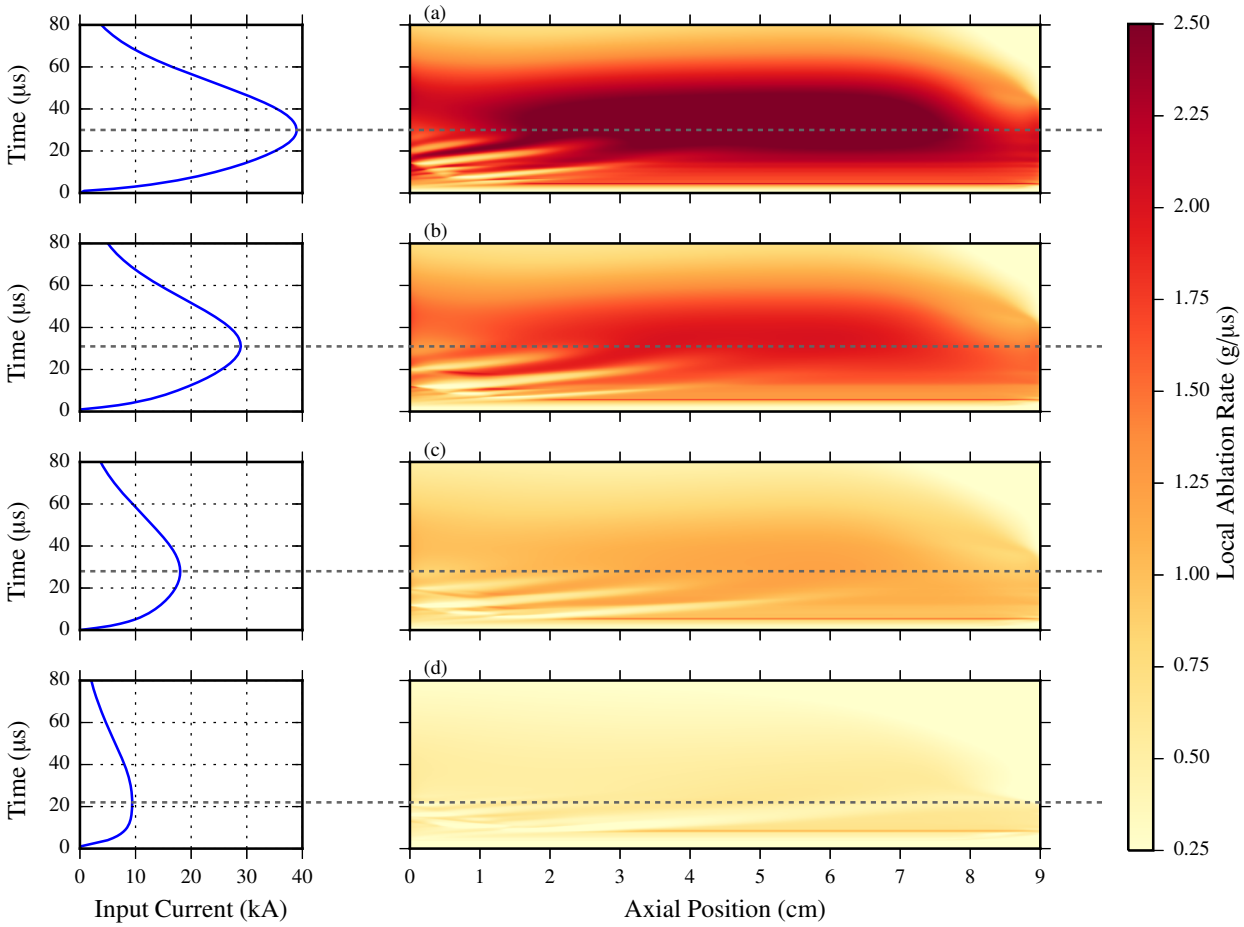

Figure 5.10: Time variation of local ablation rates along the source length for four different current pulses: (a) 40 kA, (b) 30 kA, (c) 20 kA, and (d) 10 kA peak current. The current pulses are shown on the left side of the figure. A single dotted line across the figure indicate the time of peak current in each current pulse.

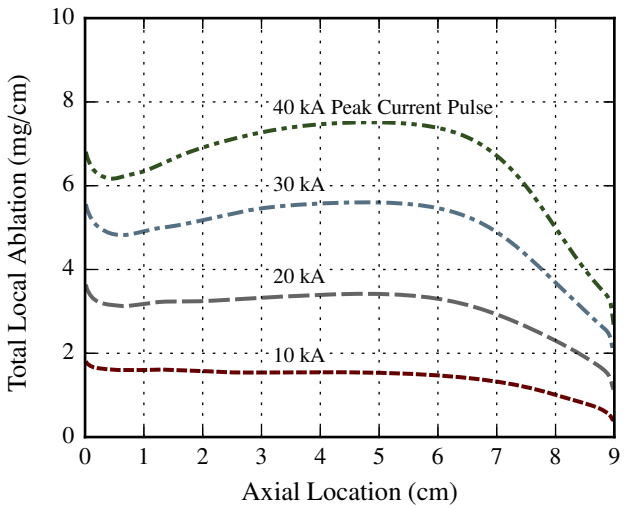

Figure 5.11: Variation in the total ablated mass along the axial length of the source after completion of discharge.

in region of source nearest the cathode. It is expected that discharge current pulses with peak currents higher than 40 kA will continue to exhibit these stabilizing effects.

As variations in the ablation rate become more localized in the region of the source near the cathode, their impact over the course of the discharge affects the topology of the total ablated mass at the end of discharge. The predicted ablation topology inside the source at the end of the discharge is shown in Fig. 5.11. Simulation results indicate post-discharge ablation is typically less near the exit of the discharge located at an axial position of 9 cm. This occurs because the exit region tends to be cooler relative to the inner region of the source due to ejection of the plasma and conduction of heat out of the domain through the open boundary. However, as the peak discharge current increases, the THOR simulation code predicts lower ablation near the cathode end of the source compared with the internal region of the source that experiences the largest ablation.

5.7 Conclusions

A fully-2D, time-dependent model of an ET plasma discharge has been developed. This represents a considerable advancement in the simulation and modeling capabilities of these discharges. The fluid dynamics of the model have been captured using the Euler gas dynamic equations. The electron fluid has been simulated using the drift-diffusion approximation. Approximations based on Ohm's law have been used for the electric field that develops inside the source. Using this approximation, reasonable agreement is achieved between simulation and experiment, and the macroscopic behavior of the plasma can be estimated. Simulation results also show consistency with the work of [32] who conducted similar experiments using a variety of materials. The use of this model and code provides the opportunity to perform more detailed analysis of ET plasma discharges than previously possible. This detail includes a more full description of the plasma-fluid dynamics involved inside the source during discharge.

A brief investigation of these plasma-fluid dynamic details has been performed. Results show that the flow of heavy gaseous particles is affected by the flow of electrons travelling away from the source exit and toward the cathode. This induces back flow of heavy particles near the source centerline. Near the closed end of the source, the heavy particles are redirected toward the radial extent of the source and toward the source exit to be ejected from the source. This causes fluid dynamic perturbations and transience in the plasma transport properties near the cathode (closed) end of the source. This transience causes variations

in the local ablation rate near the cathode. It has been observed that these effects become more localized to the cathode end of the source as the discharge peak current increases. As a result, at higher current pulses, there is up to 15% less ablated mass in the region near the cathode than the location of highest ablation occurring in the internal region of the source. These results are significant because they predict and characterize uneven ablation of the source liner material at higher discharge current pulses.

Chapter 6

Radiation Heat Transfer and Vapor Shielding in a Two-Dimensional Model of an Electrothermal Plasma Source

This chapter is a manuscript accepted for publication in the Journal of Fusion Energy. The final publication is available at Springer via http://dx.doi.org/10.1007/s10894-016-0089-7.
Citation: M. Esmond, A. Winfrey, Radiation heat transfer and vapor shielding in a two-dimensional model of an electrothermal plasma source. J. Fusion Energ. "Online First" (2016)

6.1 Abstract

Electrothermal (ET) plasma discharges are emerging as valuable mechanisms for pellet injection in magnetic confinement fusion reactors. They have been shown to be capable of achieving the required pellet velocities and pellet launch frequencies required for edge lo-

calized mode (ELM) control. Another advantage of ET plasma discharges is their ability to simulate fusion disruption events by depositing large heat fluxes on exposed materials. A deeper understanding of the heat transfer processes occurring in ET plasma discharges will aid in this particular application. ET plasma discharges involve the passage of high currents (order of tens of kA) along the axis of a narrow, cylindrical channel. As the current passes through the channel, radiant heat is transferred from the plasma core to the capillary wall. Ablated particles eventually fill the plasma channel and the partially ionized plasma is ejected. It is well known that the ablated material separating the plasma core from the ablating surface can act as a vapor shield and limit the radiation heat flux reaching the ablating surface. In this work, the results from a two-dimensional simulation model for ET plasma discharges are presented. The simulation of the plasma in a two-dimensional domain combined with the diffusion approximation for radiation heat transfer is shown to successfully simulate the effects of the vapor shield layer that develops inside these devices.

6.2 Introduction

Electrothermal (ET) plasma discharges are characterized by rapid heating and the resulting surface ablation inside a capillary geometry. Relatively large currents (tens of kA) initiate ionization and joule heating inside these devices. A schematic of an ET plasma source is shown in Fig. 6.1. Heat is transferred from the plasma to the ablating surface primarily through radiation [25]. Ablated particles fill the capillary and are ejected out the open end

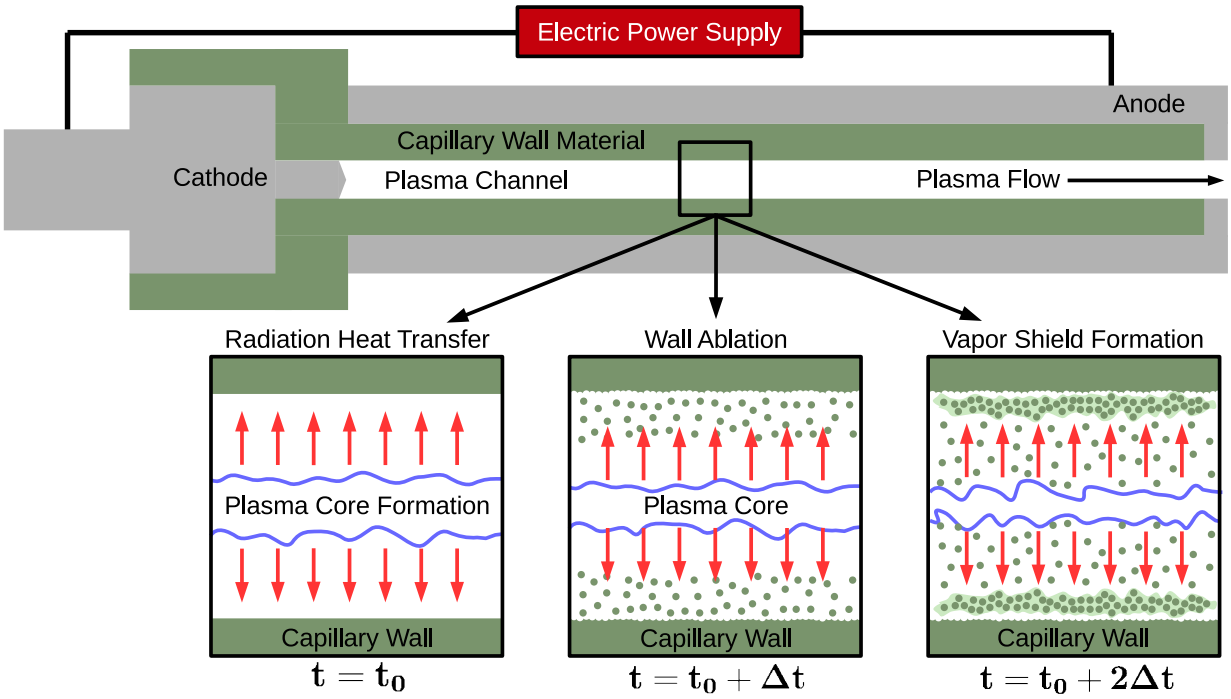

Figure 6.1: A schematic of an ET plasma source. Electric current flows through the plasma channel from the cathode to the anode. Heat is radiated from the plasma core to the capillary wall, and ablation is induced. Dense clouds of ablated vapor can build up and separate the plasma core from the capillary wall. This effect gives rise to vapor shielding. ET plasma source geometries are typically cm in length and mm in internal diameter.

as a plasma jet. Ablated particles can form a dense cloud of vapor separating the plasma core from the ablating surface. This vapor layer can block incoming radiation from the plasma core and prevent it from reaching the ablating surface. This effect is known as vapor shielding [77].

ET plasma discharges are being studied for their application to electric propulsion [38,39] and solid propellant ignition [41, 50, 52, 53]. These devices are also being explored for their potential use in pellet launcher systems for magnetic confinement fusion reactors [42, 55, 56]. ET plasma launchers offer several engineering advantages including a simple design, wide

pellet exit velocity range, and the capability of firing pellets at frequencies suitable for ELM control [57]. In addition, ET plasma discharges are being used to deliver high heat fluxes expected during disruption events in future fusion reactors [65, 68]. The investigation of the use of ET plasma discharges as high heat flux sources has been accompanied by simulation results [67]. To provide better support for these studies and deeper insight into the relationship between ablation and surface heat flux, improvements in the simulation and modeling capabilities for ET plasma discharges are required.

The ablation inside an ET plasma discharge is known to form a vapor layer separating the source liner from the plasma core. This vapor layer shields the ablating surface and limits the heat flux from the plasma core to the ablating surface [71, 77]. The boundary layer that forms between the plasma core and the ablating surface has been studied in detail by Eapen [80] and Orton [81]. These studies reinforced the concept of the vapor shield layer. Eapen and Orton focused on 2D simulation of plasma flow over a flat plate. Consequently, their results were not directly comparable with ET plasma discharge experiments. Eapen [80] expressed the need for a fully 2D model of an ET plasma source in order to sufficiently capture the fundamental physics near the ablating surface.

Foundational theoretical and semi-empirical studies were performed by Niemeyer [32] and Ibrahim [29]. Kovitya and Lowke [30] later developed a 1D, steady-state model in order to further explore the details of ET plasma discharges. They used different approximations for the radiation heat transfer from the plasma, and their results suggested that a black-body radiation approximation was well-suited to discharges with discharge current greater than 4

kA. Ruchti and Niemeyer [31] developed theoretical scaling laws for ET plasma discharge devices (a.k.a. ablation controlled arcs). These authors focused on the determination of a transparency factor which accounted for the vapor shield layer. Time-dependent modeling of pulsed ET discharge devices was performed by Gilligan and Mohanti [69] with a 0D model. These authors compared their simulation results for steady-state discharge operation with the work of Ruchti and Niemeyer [31]. Gilligan and Mohanti also compared there simulation results with pulsed ET discharge experiments that were being performed by Bourham et al. [71]. Gilligan and Mohanti [69] utilized a vapor shield factor defined as the ratio of the radiation flux reaching the ablating surface to the black-body radiation flux coming from the plasma. They adjusted the vapor shield factor in order to align simulation results with experiment. They estimated the vapor shield factor to be approximately 10%.

In the 1990s, simulation and modeling capabilities for pulsed ET plasma discharge devices progressed to 1D [45]. Hurley et al. [45] used an adaptive vapor shield factor which depended on the plasma pressure, internal energy, and sublimation energy of the liner material. However, this adaptive form for the vapor shield factor was later contested by Zaghloul et al. in favor of a constant value for the vapor shield factor [24]. Zaghloul suggested that the constant vapor shield factor be tuned in order to match simulation predictions with experimental results.

The 1D modeling capabilities were later advanced to semi-2D by Ngo et al. [74]. The semi-2D model relied on a 1D solution of bulk plasma properties and then estimated radial gradients using an radial energy equation. However, the 1D solution relied on a volumetric

source term for the ablated material rather than treating the ablation as a surface flux. This limits the ability of this semi-2D model to capture important details at the ablating surface.

More recent studies have focused on a grey-body treatment of the plasma inside ET plasma discharges. Zaghloul [25] and Pekker et al. [39] used different methods in determining the emissivity of the plasma. Zaghloul performed calculations using a 1D model, and Pekker used a 0D model. These models still incorporate ablation as a volumetric source term, which prevents the ability to capture effects occurring close to the ablating surface.

In order to address the need for a fully-2D simulation model and code for pulsed ET plasma discharge devices, the Three-fluid, 2D ET Plasma Flow Simulator (THOR) model and code have been developed. THOR couples the 2D hydrodynamics with the heat transfer effects occurring inside ET plasma devices during discharge and provides a unique and novel method of investigating the fundamental physics occurring inside these devices. The THOR simulation code is equipped to use two different approximations for the radiation heat transfer. The first approximation is a black-body approximation, and the second, a diffusion approximation. In this work, the model equations for the different radiation approximations are discussed. Simulation results are compared with experiment, and key differences between the black-body and diffusion approximations are highlighted. Lastly, the vapor shield layer simulated using the diffusion approximation for radiation heat transfer is illustrated and discussed.

6.3 Model Formulation

The THOR model and code simulate the evolution and interaction of the electron, ion, and neutral species inside ET plasma discharges in a 2D, axisymmetric domain. The electrons are simulated using the drift-diffusion approximation. The ions and neutrals are simulated using the Euler gas-dynamic equations. A first approximation for the electric field using Ohm's law is also implemented. The governing equations used in the THOR model have been introduced previously by Esmond and Winfrey [108]. Based on their work, charge exchange effects are not expected to alter results presented here by more than a few percent. Therefore, charge exchange effects have been neglected for the simulations reported in this work. In this section, the approximations used in the THOR code for radiation heat transfer are discussed in detail.

6.3.1 Radiation: Black-body Approximation

The THOR code can utilize a black-body radiation approximation for determining the radiation heat flux from the plasma to the ablating surface. For this approximation, an average temperature is determined for the heavy species over the geometric cross section of the source. The black-body radiation coming from the plasma, $q^{"}_{rad}$, is then evaluated based on this average temperature.

$$q^{"}_{rad} = \sigma(T^4_{avg} - T^4_{boil}) \tag{6.1}$$

where σ is the Stefan-Boltzmann constant, T_{avg} is the averaged heavy particle temperature, and T_{boil} is the boiling temperature of the source liner material. Previous 0D and 1D models have utilized a vapor shield factor that allows only a fraction of the black body radiation to reach the ablating surface. In these models, the vapor shield factor is typically tuned to match simulation results with experiment [24,69,88]. This approach has been avoided in the present model, and no correction factor has been used to adjust the radiation flux.

In the THOR code, the black-body radiation heat flux in Eq. (6.1) is deposited on the ablating surface and all the energy is assumed to go into causing ablation. Investigations of the effects of incorporating absorption of the radiation heat flux into the wall material have been performed for similar devices [39]. The inclusion of heat flux absorption by the wall material is not expected to significantly alter the results presented in this work, and the inclusion of these effects in the present model has been put off to a later date.

6.3.2 Radiation: Diffusion Approximation

It has been shown that the diffusion approximation for radiation heat transfer is valid for the plasmas that develop inside ET plasma discharges provided that a radiation flux limiter is used [79]. Careful attention must also be paid to the radiation flux boundary condition at the ablating surface in these devices. A radiation flux boundary condition and flux limiter have been established through the work of Hahn and Gilligan [79]. These authors used a

radiation flux boundary condition at the ablating surface given by

$$S_g = \frac{c}{2} U_g \tag{6.2}$$

where S_g is the boundary radiation flux for frequency group g, c is the speed of light, and U_g is the radiant energy. This boundary condition is suggested due to the strong anisotropy of the radiation field at the interface between the ablating surface and the plasma. These authors argue for this condition based on the similarity between the ablating surface boundary and a vacuum-fluid boundary [79]. Hahn and Gilligan also establish the radiation flux limit to be equal to the radiation flux specified in Eq. (6.2).

The diffusion model for radiation heat transfer used in THOR incorporates the findings of Hahn and Gilligan and also uses the approach adopted by Ngo [74]. It should be noted that Hahn and Gilligan utilized a multi-group diffusion model. In this work, to limit the complexity of the problem, an averaged-group diffusion model has been used. A similar approach was used by Ngo. Therefore, the boundary condition and flux limit for radiation heat transfer are given by

$$S_{rad} = \frac{c}{2} U_p \tag{6.3}$$

where $U_p = 4\sigma T_p^4 / c$ is the radiant energy of the plasma, and T_p is the plasma temperature. The plasma temperature at the boundary of the domain is used to determine the boundary radiation flux per Eq. (6.3).

By the diffusion approximation, the radiation heat flux within the simulation domain is given by

$$\mathbf{q}_{rad} = -k_{rad} \nabla T_p \tag{6.4}$$

where k_{rad} is the radiation thermal conductivity. The radiation thermal conductivity is given by [74, 75]

$$k_{rad} = \frac{16}{3} \sigma \, l_{rad} \, T_p^3 \tag{6.5}$$

where l_{rad} is the radiation mean free path. The radiation mean free path is approximated by [75]

$$l_{rad} = 0.9017 \frac{m_e^{3/2} c}{h^2 k_e^3 e^6} \frac{(k_B T_p)^{7/2}}{N^2 \bar{Z} (\bar{Z} + 1)^2} \quad \text{meters} \tag{6.6}$$

where m_e is the electron mass in [kg], c is the speed of light in [m/s], h is Plank's constant in [J s], k_e is the Coulomb constant in [Nm^2/C^2], e is the electron charge in [C], k_B is Boltzmann's constant in [J/K], T_p is the plasma temperature in [K], N is the total number density in [m^{-3}], and $\bar{Z}$ is the average charge state [unitless]. It should be noted that the form used by Zeldovich and Raizer for the radiation mean free path is in CGS units [75]. This form has been converted to MKS units in Eq. (6.6). In the present work, the radiation energy transferred in the domain is distributed between the ion and neutral species based on their mole fractions.

6.3.3 Ablation

The ablation at the surface of the source liner is determined based on the radiation flux to the surface and the heat of sublimation of the source liner material [24, 26, 45, 69].

$$\phi_{abl} = \frac{q^{"}_{rad}}{H_{sub}} \tag{6.7}$$

where ϕ_{abl} is the ablating particle flux at the ablating surface [$1/(m^2 s)$], $q^{"}_{rad}$ is the radiation heat flux to the ablating surface [W/m^2], and H_{sub} is the heat of sublimation per particle of the ablating surface material [J].

6.4 Results and Discussion

The computational investigations reported in this work were of an ET plasma source with a 9 cm length and a 2 mm radius. The source liner material used in this study was Lexan polycarbonate, or $(C_{16}H_{14}O_3)_n$. The sublimation energy for Lexan polycarbonate has been approximated to be 54 MJ/kg [109]. The average particle mass is 1.28×10^{-26} kg, and therefore, in this work, $H_{sub} = 6.91 \times 10^{-19}$ J/particle. Experimental measurements reported in this work were performed by Winfrey et al. [26]. The THOR simulation code was used to acquire simulation results for both the black-body radiation approximation and the diffusion approximation for radiation heat transfer. The black-body radiation results reported in this work were obtained using a computational mesh with $\Delta z = 2.14 \times 10^{-4}$ m and $\Delta r =$

7.14×10^{-5} m. The diffusion approximation results were obtained using a computational mesh of $\Delta z = 2.5 \times 10^{-4}$ m and $\Delta r = 5.56 \times 10^{-5}$ m. Experimentally measured current pulses are used as simulation inputs. Experiments have been performed using the Plasma Interaction with Propellant Experiment (PIPE) and reported in the work of Winfrey et al. [26]. Simulation results from four PIPE shots are reported in this work. The four PIPE shots are identified as P213, P215, P228, and P204. These PIPE shots have nominal peak currents of 10, 20, 30, and 40 kA, and input shot energies of 1.09, 2.42, 4.09, and 5.91 kJ, respectively. Each current pulse has an active pulse length of approximately 100 µs. Current pulses for these shots are well-documented [26].

Validation of the THOR model and code has been performed by comparing the total predicted ablated mass with the total measured ablated mass. This comparison is shown in Fig. 6.2. Figure 6.2 indicates that the results from the black-body radiation approximation align better with experiment at input shot energies less than 3 kJ. However, the black-body radiation approximation tends to overestimate the total ablated mass at input shot energies higher than 3 kJ. The diffusion approximation for radiation heat transfer underestimates the total ablated mass for input shot energies less than 3 kJ, but predicts ablated mass values within the experimental uncertainty for input shot energies higher than 3 kJ. This difference in the lower (i.e. < 3 kJ) and higher (i.e. > 3 kJ) input shot energies has been observed by Winfrey et al. [26]. These authors focused on ideal versus non-ideal behavior of the plasma. Their findings suggest that plasma non-ideality becomes more important as the discharge energy increases. Similarly, in this work, the results indicate that detailed estimation of

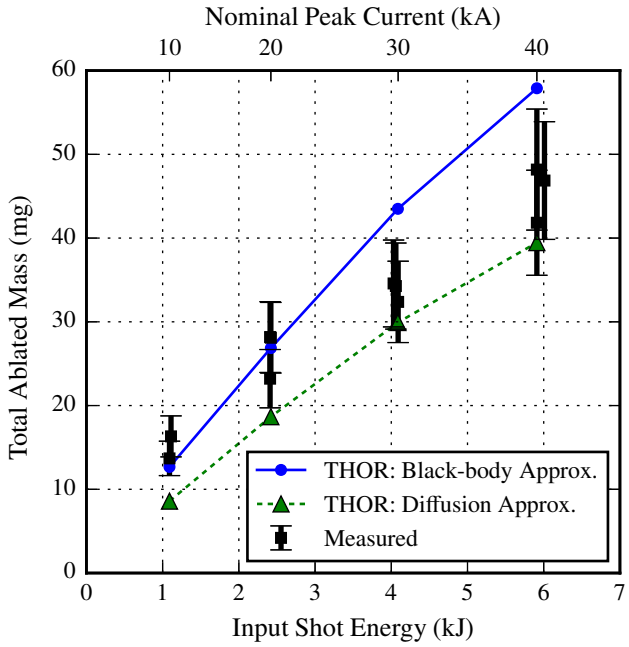

Figure 6.2: The total ablated mass predicted using the THOR simulation code is compared with experimentally measured ablated mass. Experimental measurements are reported by Winfrey et al. [26]. Four different current pulses, P213, P215, P228, and P204, were simulated using the THOR simulation code with both the black-body and diffusion approximations for radiation heat transfer. THOR simulations were run to a simulation time of 250 µs.

the radiation heat flux becomes more important as the discharge energy increases. This observation is consistent with the work of AlMousa [88] who observed that the vapor shield layer becomes more important at higher discharge energies. The vapor shield layer develops as ablated particles enter the capillary source and shield the capillary walls from incoming plasma radiation. In the THOR code, the diffusion approximation for radiation heat transfer accounts for this vapor shield layer by forcing thermal energy to diffuse from the plasma core through the ablated vapor toward the ablating surface. This technique of capturing the effects of the vapor shield layer has not been implemented previously. The black-body approximation ignores the vapor shield layer and allows energy to be transferred directly

from the plasma core to the ablating surface. This results in an overestimation of total ablated mass at input discharge energies > 3 kJ.

Each of the four PIPE current shots were simulated with both the black-body and diffusion approximations for radiation heat transfer. Therefore, a total of eight simulations are represented in this work. The ablation rates predicted in each simulation are shown as a function of simulation time in Fig. 6.3. As implied in Fig. 6.2, the diffusion approximation for radiation heat transfer results in a lower ablation rate throughout the simulation. As discussed later, this lower ablation rate is due primarily to the ability of the diffusion approximation to capture the effects of the vapor shield layer which reduces ablation. The black-body radiation approximation predicts relatively high transience in the ablation rate early in the discharge as shown in Fig. 6.3. This transience has been investigated in more detail in a previous work [110]. In contrast to the black-body results, the diffusion approximation results show a relatively steady rise and fall in the ablation rate as the input current increases and recedes.

To further investigate the differences in the two approximations for radiation heat transfer, the time evolution of the radial distribution of the neutral temperature is shown in Fig. 6.4. The neutral temperature is representative of the plasma temperature as the species tend toward local thermodynamic equilibrium. The black-body radiation approximation predicts a very fast rise in temperature at the core of the ET plasma source. This happens during the first 10 µs of the discharge. As the simulation progresses, the core temperature quickly diminishes as the temperature over the remainder of the source cross-section rises. It

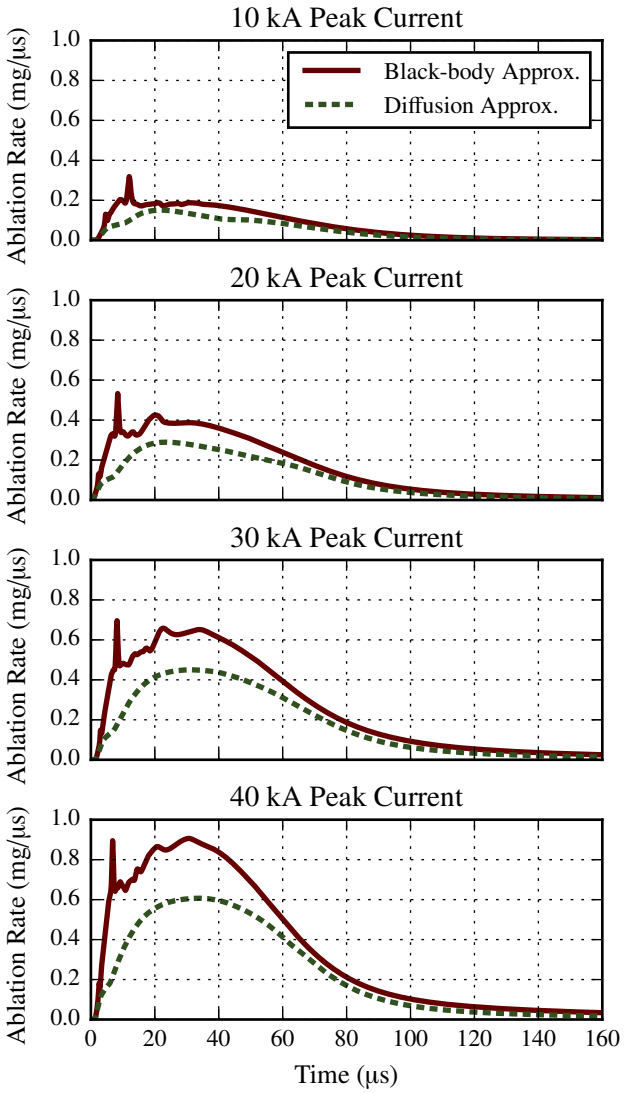

Figure 6.3: The ablation rate time history for each of the eight THOR simulations represented in this work.

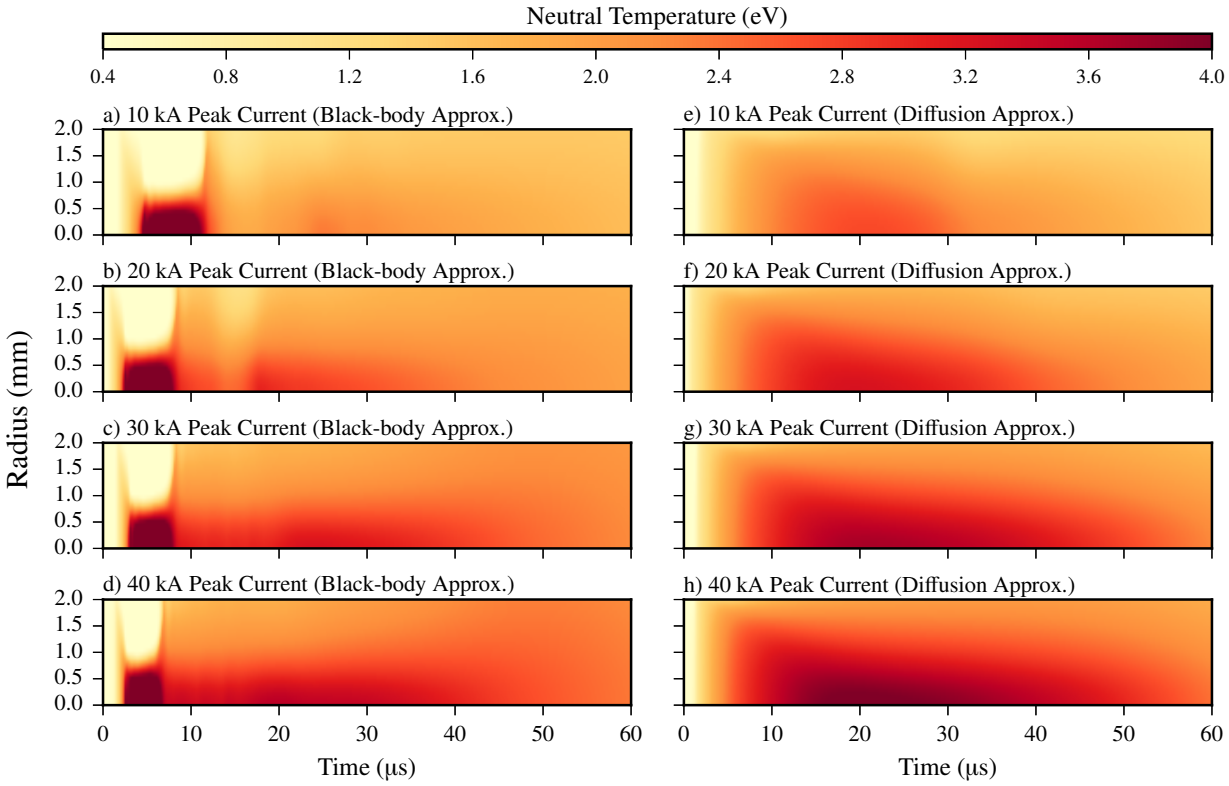

Figure 6.4: The time history of the neutral species temperature distribution over the mid-point of the source (i.e. $z = 4.5$cm). Black-body radiation results are shown in (a)-(d), diffusion approximation results are shown in (e)-(h).

is interesting to note the similarity between the results shown in Fig. 6.4(a-d) and the results presented by Zaghloul [25]. Zaghloul performed a simulation of a 40 kA peak current shot and focused on reproducing the experimental ohmic power input to the source. Zaghloul observed a spike in the plasma temperature at the beginning of the discharge similar to those observed in Fig. 6.4. In this work, and in that of Zaghloul, the initial spike in the temperature is attributable to the lower initial plasma density. At lower plasma densities, the high ohmic power input from the electric current will quickly raise the temperature of the plasma. As the plasma density increases due to ablation, the plasma temperature reduces. The diffusion approximation for radiation heat transfer predicts a relatively gradual rise in the temperature over the cross section of the source. This is due to rapid diffusion of thermal energy by radiation heat transfer. Radiation diffusion is more rapid at the beginning of the simulation due to the lower initial plasma densities.

After discharge initialization (approx. 12 µs), the radial temperature gradients observed for the diffusion approximation are greater than those predicted in the black-body approximation. This is due to the direct energy transfer from the plasma core to the ablating surface via the black-body radiation approximation. By using the diffusion approximation, this energy at the plasma core must diffuse through the plasma bulk in order to reach the ablating surface. This effect increases temperature gradients in the radial direction inside the ET plasma source. In Fig. 6.5, the temperature distributions at the source midpoint ($z = 4.5$cm) of the ET plasma source at simulation times of 30 µs are shown for each simulation. The higher temperatures at the plasma core predicted by the diffusion approximation

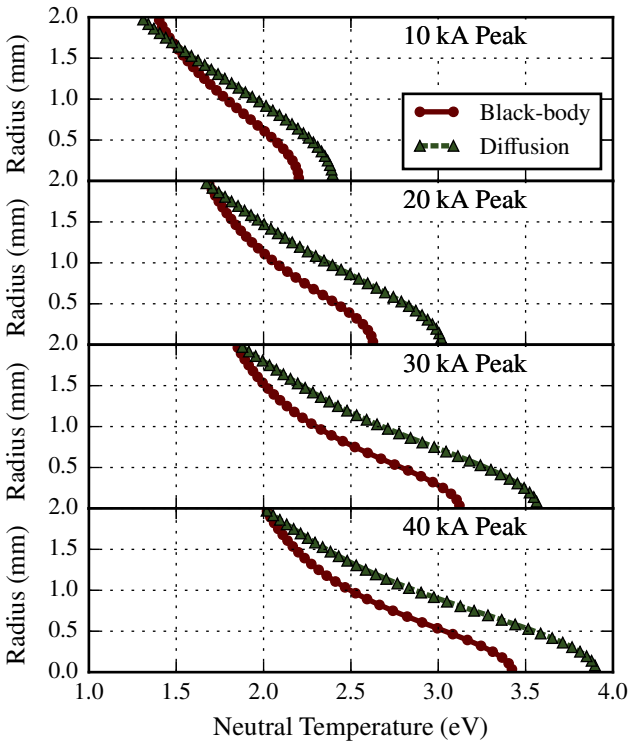

Figure 6.5: Neutral species radial temperature distribution at the source midpoint (z = 4.5cm) at a simulation time of 30 µs.

result in a higher electrical conductivity. Higher electrical conductivity reduces the ohmic power deposited in the device. The lowered energy deposition plays a role in lowering the total predicted ablated mass for these simulations (see Fig. 6.2).

Further investigation of the simulation results reveals information about the development of the vapor shield layer separating the plasma core from the ablating surface. As discussed in Sec. 6.3.2, the diffusion approximation for radiation heat transfer relies on the radiation thermal conductivity k_{rad}. The radiation thermal conductivity can be used as an indicator of the vapor shield layer inside the ET plasma source during operation. The full spacial distribution of the radiation thermal conductivity inside the ET plasma source is shown

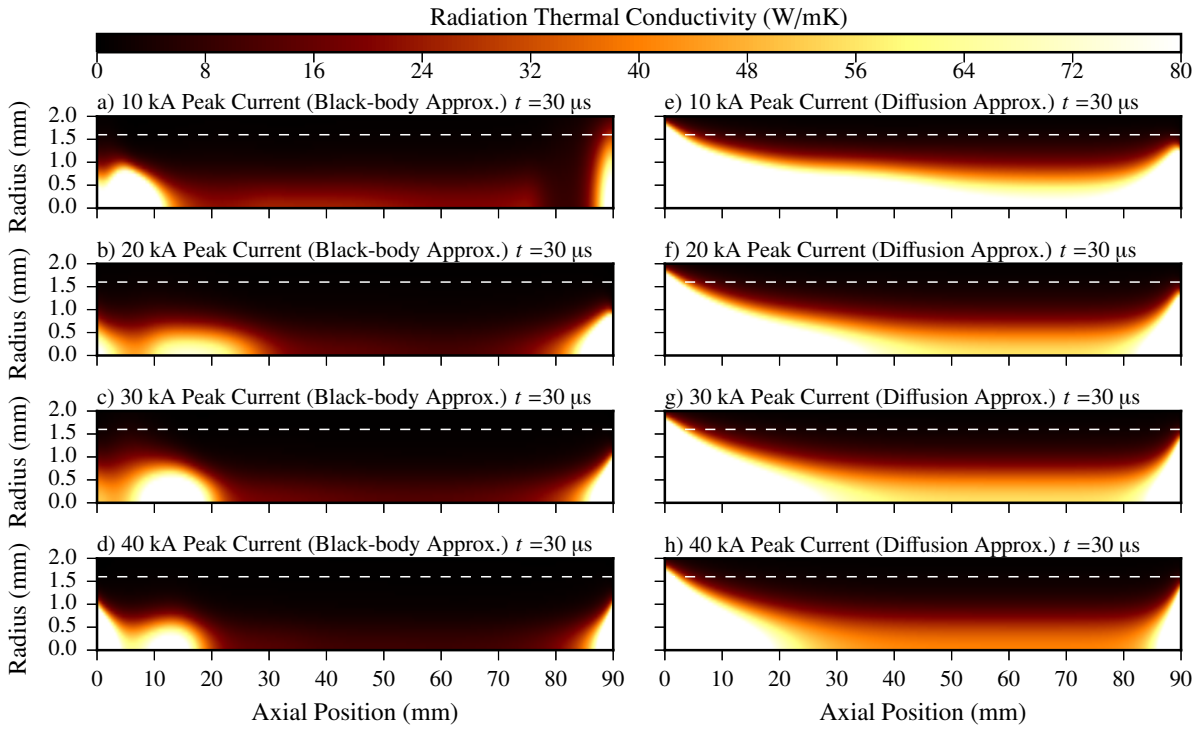

Figure 6.6: Full distributions of the radiation thermal conductivity. Black-body approximation results are shown in (a)-(d), and diffusion approximation results are shown in (e)-(h). The simulation time for each distribution is 30 µs corresponding roughly to the time of peak current. The ablating surface is at a radius of 2 mm. The source centerline is at a radius of 0 mm. The dashed line in each plot indicates the thickness of the vapor shield layer as estimated by Ibrahim [29]. The radiation thermal conductivity is not incorporated in the black-body radiation model but is shown in (a)-(d) for the sake of comparison.

for each simulation at a simulation time of 30 µs in Fig. 6.6. For the black-body radiation approximation, there is little evidence of a vapor layer forming at the boundary between the plasma core and the ablating surface (see Fig. 6.6(a-d)). It should be noted that the black-body radiation approximation results do not incorporate the use of the radiation thermal conductivity; it is shown here for comparison. The diffusion approximation results clearly indicate the development of a vapor shield layer which is indicated by the region of relatively low radiation thermal conductivity near the ablating surface (see Fig. 6.6(e-h)). The

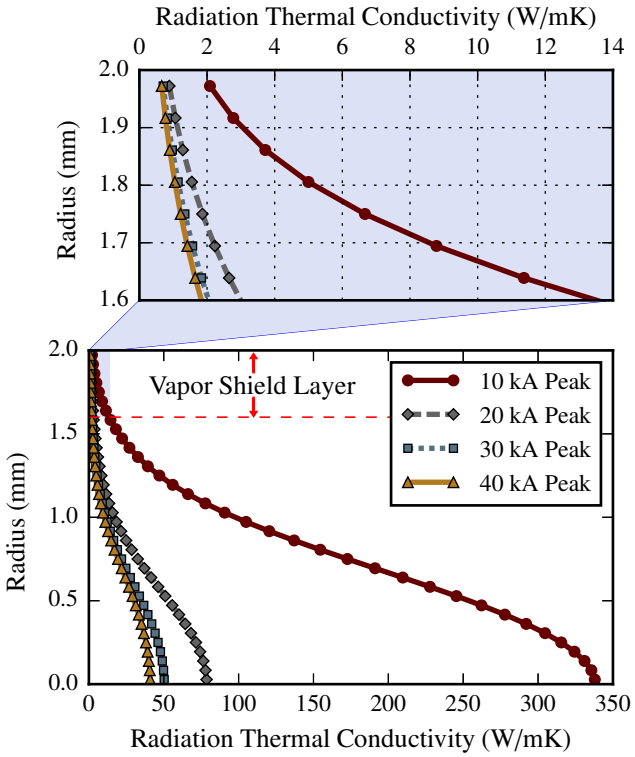

Figure 6.7: The radial distribution of the radiation thermal conductivity for the 10, 20, 30, and 40 kA peak current pulse simulations using the diffusion approximation for radiation heat transfer. The dashed line indicates approximate thickness of the vapor shield layer as estimated by Ibrahim [29]. Results are shown for simulation times corresponding to the time of peak current in each discharge.

radiation thermal conductivity is lower near the ablating surface because of generally lower temperatures and increased particle density due to ablation. This lower radiation thermal conductivity is indicative of the vapor shield layer which limits the heat transfer from the plasma core to the ablating surface. The dashed line shown in Fig. 6.6(a-h) indicates the estimated thickness of the vapor shield layer [29].

The distributions of the radiation thermal conductivity for the diffusion approximation results are shown at the source midpoint in Fig. 6.7. The radiation thermal conductivity is higher for the 10 kA peak current shot due to the lower particle densities caused by less

ablation. Higher ablation, as in the cases of the 20, 30, and 40 kA peak current pulses, leads to a lower radiation thermal conductivity overall. Figure 6.7 highlights the vapor shield layer and shows that in this layer, the radiation thermal conductivity is less than or equal to 4% of the maximum radiation thermal conductivity of the same current shot at simulation times of peak discharge current. The thickness of the vapor shield layer shown in Fig. 6.7 is based on an estimate made by Ibrahim [29].

6.5 Conclusions

The Three-fluid, 2D ET Plasma Flow Simulator (THOR) has been developed in order to investigate the fundamental physics occurring inside ET plasma discharges in more detail than previously possible. THOR couples the hydrodynamics, species interactions, and heat transfer effects inside an ET plasma discharge. Recent enhancements of the THOR model and code allow for the estimation of heat transfer effects via a diffusion approximation for radiation heat transfer. Simulation results for both the original black-body radiation approximation and the diffusion approximation have been analyzed and compared. The black-body approximation produces better agreement with experiment for lower discharge energies (< 3 kJ) while the diffusion approximation produces better agreement at higher discharge energies (> 3 kJ). This is attributed to the increasing importance of the vapor shield layer that develops near the ablating surface inside ET plasma discharges at higher discharge energies. The diffusion approximation is shown to successfully simulated the effects

of the vapor shield layer without the need for a tunable correction factor. The implementation of the diffusion approximation for radiation heat transfer in the THOR code allows for the direct simulation of the vapor shield layer. This ability represents a significant advancement in the simulation and modeling capabilities available for ET plasma discharges and facilitates a deeper understanding of the underlying physics involved in these devices. This deeper understanding of the underlying physics will be an aid to researchers utilizing the high heat fluxes in ET plasma discharges to simulate disruption conditions in future fusion reactors.

Chapter 7

Investigation of Source Geometry Effects in a Pulsed Electrothermal Plasma Discharge Using a Two-Dimensional Simulation Model

This chapter is a manuscript submitted for publication in IEEE Transactions on Plasma Science. Citation: M. Esmond, A. Winfrey, Investigation of source geometry effects in a pulsed electrothermal plasma discharge using a two-dimensional simulation model. Manuscript submitted for publication. (2016)

7.1 Abstract

Electrothermal (ET) plasma discharges have application to mass acceleration technologies relevant to military ballistics and magnetic confinement fusion reactor operation. ET plasma discharges are initiated in capillary geometries by passing large currents (order of tens of

kA) along the capillary axis. A partially ionized plasma then forms and radiates heat to the capillary walls inducing ablation. Ablated particles enter the capillary plasma source and cause a pressure surge that can propel pellets to velocities exceeding 2 km/s. These devices present several advantages over other mass accelerator technologies due to their a simple design and ability to achieve high projectile launch frequencies. In order to investigate the operation of ET plasma discharges in more detail than previously possible, a two-dimensional, multi-fluid model has been developed to simulate the plasma-fluid dynamics that develop in these devices during operation. In this work, the 2D simulation model is used to investigate the effect of source geometry and current density on discharge characteristics. Peak pressure and electric field magnitudes for pulsed discharge operation are shown to scale well with theoretical and empirical scaling laws for steady-state discharge operation. The pulse shape of the source internal pressure is shown to change significantly with increasing source radius. The behavior of other plasma parameters are investigated. In addition, observations of the departure from the ablation-controlled arc regime are presented. This analysis suggests that, for the current pulse length investigated, source radii higher than 4 mm require significantly more current density in order to produce sufficient ablation to stabilize the plasma discharge.

7.2 Introduction

Electrothermal (ET) plasma discharges produce partially ionized plasma inside a capillary geometry called a source. Typical source radii are on the order of mm and lengths are on

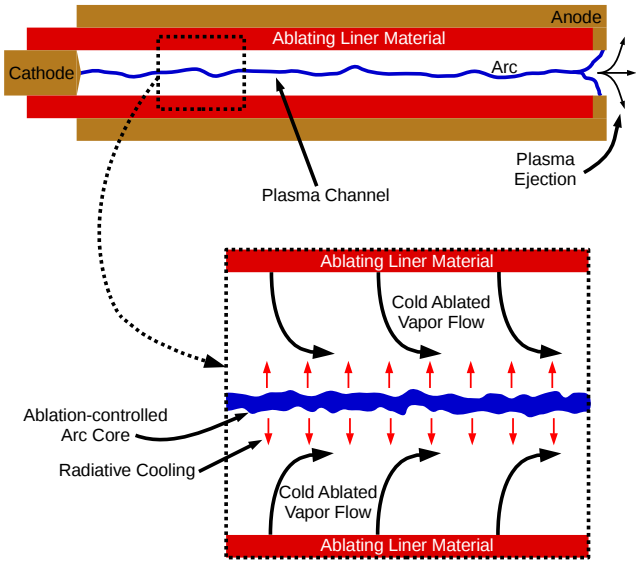

Figure 7.1: An ET plasma source schematic (not to scale). An electric current is driven through the plasma channel from the cathode to the anode. The plasma arc forms and radiates heat to the source liner. The liner material ablates, and ablated particles act to cool and stabilize the plasma arc. The partially ionized plasma is then ejected from the open end of the source into and acceleration barrel (not shown).

the order of cm. Large electric currents (order of tens of kA) are passed through the source in order to initiate the plasma. The electric current is typically pulsed, and pulse lengths are usually on the order of hundreds of µs. Radiant heat flux from the plasma core incident on the liner material (i.e. capillary wall) induces ablation. The ablated vapor is cold relative to the plasma arc and convectively cools the arc. As ablated particles fill the plasma source, plasma is ejected out of the open end of the source usually into an acceleration barrel. A schematic of an ET plasma source is shown in Fig. 7.1.

ET plasma discharges have been widely studied and applied to various mass acceleration technologies. These discharge devices have been used to pre-inject plasma armatures into magnetic rail guns in order to gain better control of armature properties [46, 48]. ET plasma

discharges have also been used to provide the sole means of acceleration for projectiles in small-caliber weapons [43]. A significant amount of research has been performed in the area of electrothermal chemical (ETC) guns [41, 52, 53, 91, 111]. ETC guns use an ET plasma discharge in order to ignite solid propellant in a combustion chamber. ETC guns provide significant advantages over conventional ballistic devices due to decreased ignition delay times and more consistent ignition times [52]. The concept of using an energetic ET source, where the ablating liner material is a energetic fuel, has recently been explored in connection with mass acceleration [58].

ET plasma discharges are also applicable to magnetic confinement fusion technology as pellet injector systems [42,55–57] and experimental high heat flux sources [65,67,112]. Pellet injection in magnetic confinement fusion reactors accomplishes plasma core fuelling [60], edge localized mode (ELM) control [61], disruption mitigation [63], and thermal quench of the fusion plasma [113]. The capabilities of ET plasma discharges to achieve the required pellet velocities as well as high pellet launch frequencies have been demonstrated computationally [57]. Components inside future magnetic confinement fusion reactors will experience large heat fluxes during operation. The performance of tungsten under these high heat fluxes has recently been investigated using an ET plasma source [112].

Simulation and modeling capabilities of pulsed ET plasma discharges have been limited to 1D models in recent years [26,44,45]. The validity of 1D models relies on small aspect ratios (i.e. the ratio of the capillary radius to its length). Most experimental and computational work has focused on these small aspect ratios ranging from 0.017 to 0.025 [26, 57]. As

researchers and scientists seek to leverage the advantages of ET plasma discharges, the need to understand the behavior of these devices when operated under different geometric configurations increases. The behavior of ET plasma discharge sources at higher aspect ratios has not been studied in much detail due to the limits of the simulation and modeling capabilities. In order to investigate the behavior of ET plasma discharges at higher aspect ratios, a fully-2D model of the discharge needs to be employed.

7.3 THOR: A Fully-2D Model for ET Plasma Discharges

To address the need for a 2D model of a pulsed ET plasma source, the Three-fluid, 2D ET Plasma Flow Simulator (THOR) has been developed. The governing equations used in the THOR model and code have been presented previously [108] and are summarized in this section. THOR simulates the time evolution of the electron, ion, and neutral species. The electrons are simulated using the drift-diffusion approximation, and the ion and neutral species are simulated with separate sets of the Euler gas-dynamic equations. The three species interact in the simulation domain by means of ionization, recombination, collisional drag, and collisional heat exchange. Based on the findings of Esmond and Winfrey [108], charge exchange effects have been neglected in the present work. A first approximation to the electric field based on Ohm's law is currently implemented, and the radiation heat transfer from the plasma to the ablating surface is modeled using a black-body radiation approximation. Simulation results from the THOR code have been verified and validated

[108]. In this work, the THOR model and code are used to explore the effect of increasing source radius on plasma parameters inside a pulsed ET plasma discharge.

7.4 Review of Theoretical and Empirical Scaling Laws

Scaling laws for ET plasma discharges and similar devices have been developed in the past and are reviewed in this section. The primary authors who have contributed to this effort are Niemeyer [32] and Ibrahim [29, 114]. Capillary plasma discharges (a.k.a. ET plasma discharges) have also been referred to as evaporation or ablation-dominated high-current arcs. Both Niemeyer and Ibrahim considered steady-state discharge operation in a capillary geometry open at both axial ends. As will be considered in Sec. 7.5, the scaling laws developed by Niemeyer and Ibrahim are also applicable to the subject of the present work, namely, a pulsed discharge open only at one axial end.

Niemeyer developed theoretical scaling laws for key parameters in capillary plasma discharges [32]. His scaling laws were validated primarily by the measurement of the electric field strength for a variety of source liner materials and current densities. Niemeyer conducted experiments with source liner materials including ceramics, metals, and polymers. Niemeyer's experimental capillary geometries were 0.5-2 mm in radius, and 1-20 mm in total length. His scaling laws for the electric field strength and pressure are given by

$$E_z \propto \left(\frac{I}{\pi R^2}\right)^{3/5} R^{1/5} \tag{7.1}$$

$$P \propto \ell \left(\frac{I}{\pi R^2} \right)^{8/5} R^{1/5} \tag{7.2}$$

where E_z is the electric field strength, I is the input current, R is the source radius, ℓ is the source half length, and P is the pressure.

Ibrahim [29, 114] developed semi-empirical scaling laws backed by more extensive measurements. Ibrahim used a polymethylmethacrylate liner material that was transparent in order to take photographic, spectroscopic, and radiative measurements of the arc emissions from the discharge channel. He used two different geometries, one with 15 cm length and 3 mm radius, and one with 20 cm length and 5 mm radius. His semi-empirical scaling laws for electric field strength and central pressure are given by

$$E_z = 2.65 j^{0.4267} \quad \text{V/cm} \tag{7.3}$$

$$P = 6.375 \times 10^{-3} j^{0.955} \quad \text{bar} \tag{7.4}$$

where j is the current density in units of A/cm^2.

Niemeyer predicted that the pressure and electric field scale more strongly with current density compared with Ibrahim's predictions. This difference may be due to a variety of causes including the fact that Ibrahim used a transparent liner material. The use of a transparent liner material would allow radiative energy to be released that otherwise would have gone into ablating the liner material and increasing the discharge pressure. Similar

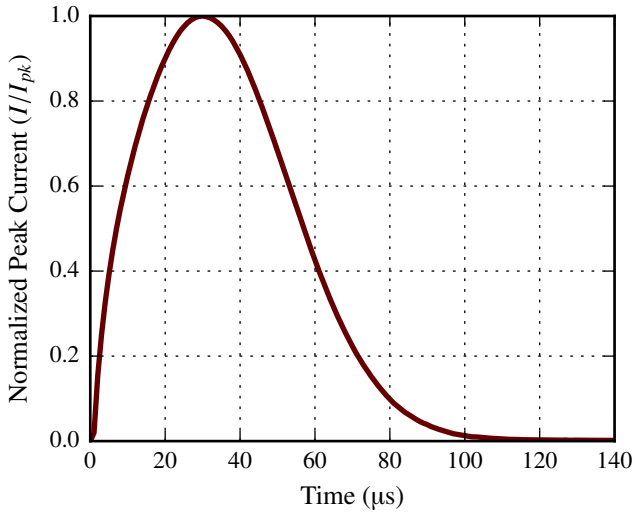

Figure 7.2: Normalized input current pulse. Current pulse is scaled in order to reach specific peak currents and corresponding peak current densities. The length of the current pulse has been held constant in the present work.

reasoning could be employed to explain the weaker scaling of the electric field in the case of Ibrahim's predictions.

7.5 Results

The THOR simulation code was used to perform simulations of ET plasma sources with a range of current pulses and source radii. The source length was held constant for this study at 9 cm, and the source liner material simulated was Lexan, or $(C_{16}H_{14}O_3)_n$. Current pulses are used as simulation inputs. For this study, a single current pulse was used and scaled up to reach required peak currents and corresponding peak current densities. The normalized current for each input current pulse used in this study is shown in Fig. 7.2. The source radii simulated were 2, 2.5, 3, 3.5, 4, 5, and 6 mm. The peak currents simulated were 10, 20, 40,

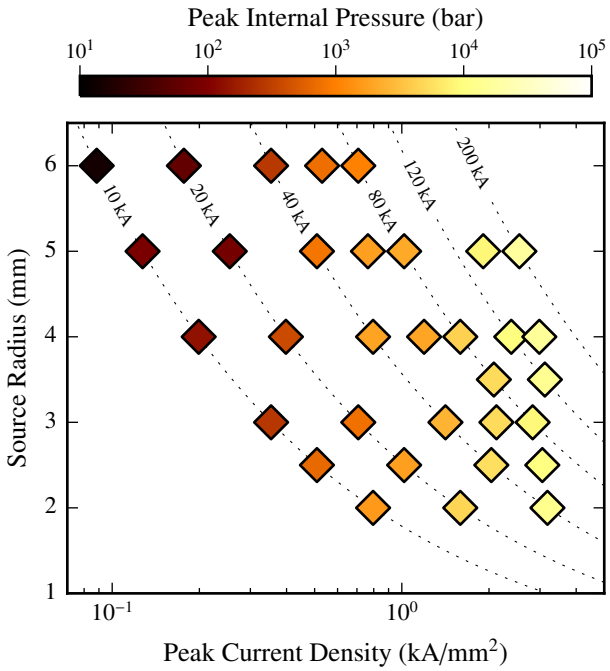

Figure 7.3: Simulated source radius versus the peak current density. Each simulation reported in the present work is represented by a single marker. Peak internal pressure was taken from the simulation results at the source centerline and 3 cm from the source opening. Contour lines indicate peak discharge current used in the simulation.

60, 80, 120, 150, and 200 kA. Each simulation was carried out on a computational grid with $\Delta z = 4.0 \times 10^{-4}$ m and $\Delta r = 1.67 \times 10^{-4}$ m. The simulation parameters of source radius and peak current density used in this study are presented in Fig. 7.3. Peak simulated internal pressure in the ET plasma source is also reported in Fig. 7.3 for each simulation.

In Fig. 7.4, simulated results for the peak internal pressure and electric field strength are compared with the scaling laws developed by Niemeyer and Ibrahim (see Sec. 7.4). Internal pressure and electric field strength are recorded from the simulation results at the source centerline and 3 cm from the source exit. The THOR simulation results for peak internal pressure show good agreement with the scaling predictions of Niemeyer. It is interesting to

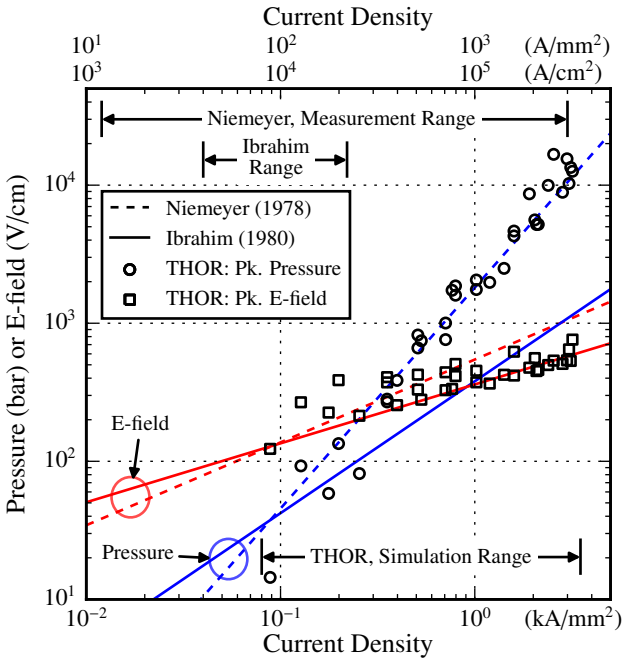

Figure 7.4: Peak internal pressure and electric field strength predicted by the THOR simulation code at varying peak current densities. The internal pressure and electric field strength were taken from the simulation results at an axial distance of 3 cm from the source exit. Scaling laws developed by Niemeyer [32] and Ibrahim [29] are also plotted as dashed and solid lines, respectively. The range of current densities for which experiments were performed by these authors is indicated on the plot along with the range of simulated current densities using the THOR code.

note this agreement between the THOR simulation results and Niemeyer's predictions due to the fact that Niemeyer's work only considered steady state operation of a discharge open at both axial ends while THOR is used to simulate a pulsed discharge open at one axial end. The THOR simulation results for the peak electric field strength scale well with the predictions made by Ibrahim. A closer investigation of the measurements reported by Niemeyer show that the scaling of the electric field strength can vary based on the liner material used in the discharge. Niemeyer's measurements for the electric field strength in a polyethylene discharge show weaker scaling with the current density than is reflected in his derived scaling

law. As indicated in Fig. 7.4, Ibrahim's experiments of a polymethylmethacrylate discharge also indicate weaker scaling with current density than predicted by Niemeyer. Therefore, it is not surprising that the THOR simulation results for Lexan discharges show scaling of the electric field strength aligning better with that of Ibrahim due to the similarity in the materials used.

7.5.1 Effect of Increasing Source Radius on Pulsed ET Plasma Discharge Parameters

The THOR simulation code has been used to simulate pulsed ET plasma discharges for a range of source radii and peak current densities (see Fig. 7.3). In order to investigate the effect of increasing the source radius on plasma parameters, the six simulations with the highest peak current densities were analyzed in detail. These six simulations have roughly similar peak current densities that are between 2.5 and 3.2 kA/mm^2. These simulations represent source radii ranging from 2-5 mm. The time history of the total internal plasma pressure developed inside the ET plasma source for these six simulations is shown in Fig. 7.5. Figure 7.5 illustrates a change in the behavior of the internal pressure as the source radius increases. For a source radius of 2 mm, the internal pressure pulse demonstrates a wider profile in the time domain. As the source radius increases, the profile in the time domain becomes more narrow. The 2.5 and 3 mm radius simulations indicate transition profiles between the wide and narrow pressure profiles. These pressure characteristics will play an important role in the functionality of an ET plasma discharge when being used as a launching

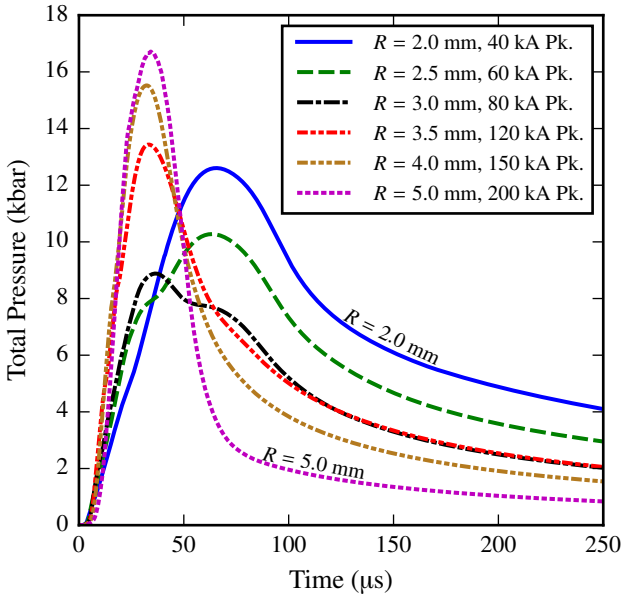

Figure 7.5: The time history of the total internal pressure inside the ET plasma source during simulation. Internal pressure is recorded at the source centerline and 3 cm from the source exit. Simulation peak currents and source radii are indicated in the legend. The peak current density achieved for each simulation is roughly similar ranging from 2.5 to 3.2 kA/mm^2.

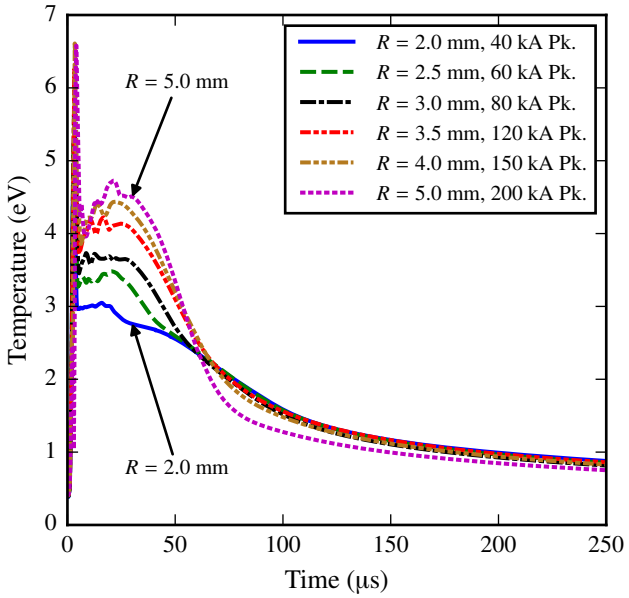

Figure 7.6: Temporal variation of the internal temperature during discharge simulation. The temperature is recorded at the source centerline and 3 cm from the source exit. Legend indicates peak discharge current and simulated source radius.

device. The change in the behavior of the internal pressure is due to the lower densities that are developed inside the source due to higher source radii.

The time history of the internal plasma temperature is shown in Fig. 7.6. The THOR simulation results predict a fast rise and fall in the plasma temperature in the first 10 μs of the discharge. This fast rise and fall in temperature is consistent with the findings of a previous study [25] and is due to low initial plasma density. Overall, the THOR simulation code predicts higher internal/core temperatures at higher source radii during the first 60 μs of the discharge. The prediction of higher core temperatures is due to the lower densities that develop at the plasma core for higher source radii. The radial distributions of the plasma temperature for the different source radii are shown in Fig. 7.7 for a simulation time of 30 μs. Figure 7.7 shows that the temperature variation over the source cross section is higher at

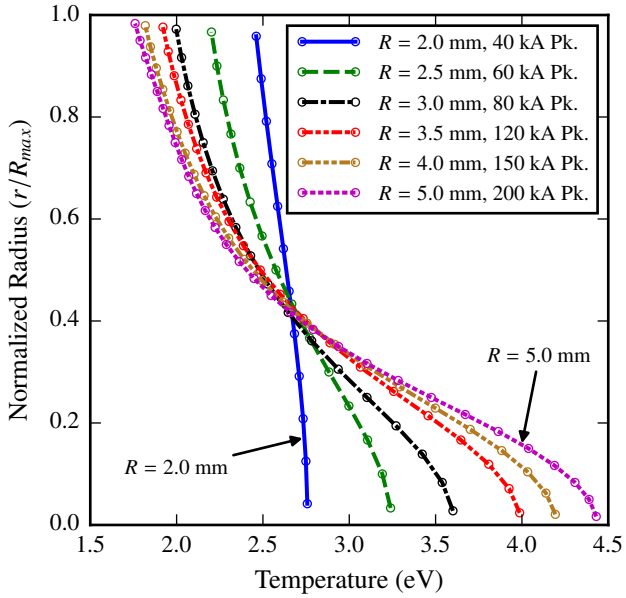

Figure 7.7: Radial distribution of the plasma temperature at the midpoint of the ET plasma source at a simulation time of 30 µs (time of current peak). Legend indicates peak current and simulated source radius.

higher source radii. These larger temperature variations for higher source radii are a result of the increase in the physical distance between the plasma core, where a significant portion of the ohmic power is deposited, and the ablating surface. The ablating surface absorbs thermal energy and introduces cold, ablated particles into the flow. It is interesting to note that the average temperature over the geometric cross sections represented in Fig. 7.7 varies from 2.6-2.7 eV. This suggests that the average temperatures over the geometric cross section are similar for similar peak current densities. Analysis of only the plasma core temperature (as shown in Fig. 7.6) leaves out these details.

7.5.2 Observations of Departure from the Ablation-controlled Arc Regime

In a foundational work on capillary plasma discharges, Ruchti and Niemeyer [31] call these types of discharges ablation-controlled arcs. These authors explain that ablation acts to cool and stabilize the arc as it forms inside the capillary channel. This language is especially helpful as the simulation results obtained using the THOR model and code are analyzed, especially in the case of the lower current densities considered. A close inspection of Fig. 7.4 reveals that at lower current densities there is more spread in the simulation data. As will be discussed in this section, this spread in the data is attributed to a departure from the ablation-controlled arc regime. The THOR simulation code is not equipped at this time to accurately model some of the phenomena occurring after the departure from the ablation-controlled arc regime. However, THOR simulation results are used in this section in order to make qualitative observations about the behavior of the discharge under these conditions.

In order to investigate the behavior of an ET plasma discharge at low current densities, four simulations are investigated in detail. Each of these simulations was conducted using an input current pulse peaking at 20 kA. The simulated source radii for these simulations were 2, 2.5, 4, and 5 mm. These simulations correspond to peak current densities ranging from 1.6 to 0.25 kA/mm^2. The time history of the internal plasma temperature for these four simulations is shown in Fig. 7.8. Each simulation represented in Fig. 7.8 demonstrates a fast rise in temperature in the first 10 μs. As the plasma temperature increases, ablation of the source liner material is induced. For the 2 and 2.5 mm source radii (Fig. 7.8a), the

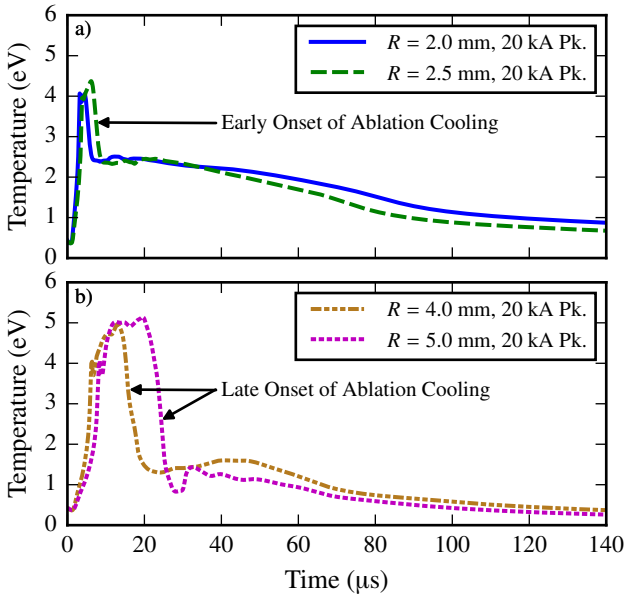

Figure 7.8: The time history of the internal plasma temperature illustrates the onset of ablation cooling inside four simulations of an ET plasma discharge. Each simulation was produced with the same current pulse but differing source radii. Early onset of ablation cooling occurs for the 2 and 2.5 mm radius simulations. However, for 4 and 5 mm radius, late onset of ablation cooling occurs.

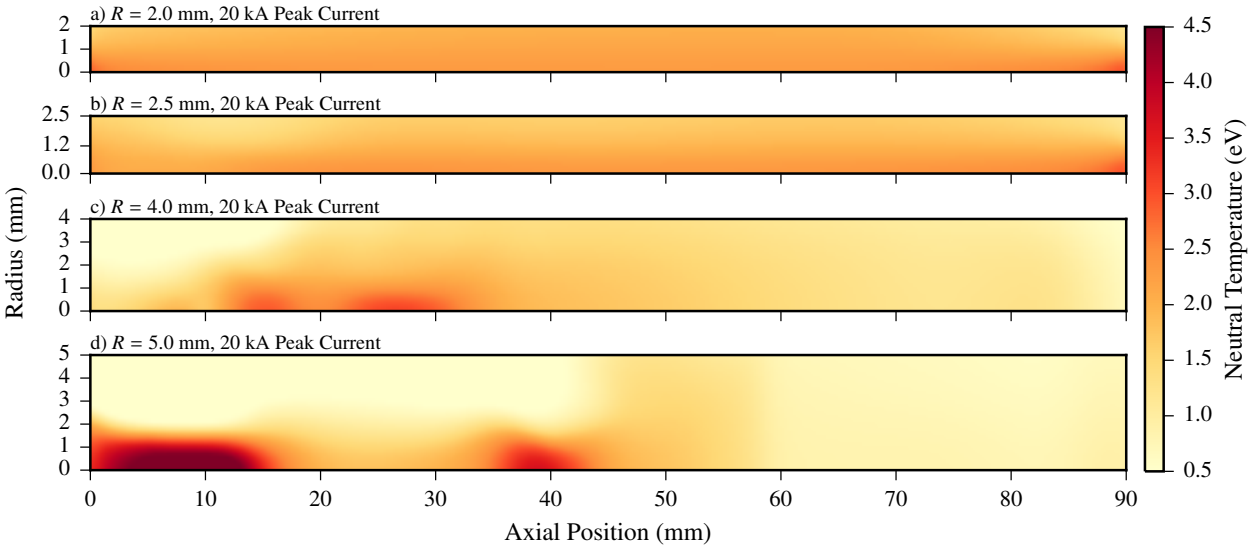

Figure 7.9: Full distributions of neutral species temperature at a simulation time of 30 µs corresponding to time of peak current. Results from a 20 kA peak current pulse simulated for sources with radii of 2, 2.5, 4, and 5 mm are shown.

induced ablation cools the plasma early in the simulation. However, for the 4 and 5 mm source radii simulations (Fig. 7.8b), the onset of the ablation cooling occurs much later in the simulation. This late onset of ablation cooling is an indication that the discharge is not sufficiently controlled by the ablation process. Operating in the ablation-controlled arc regime is desirable because of the more reliable operating characteristics and more efficient conversion of electric energy to ablated material.

A qualitative illustration of the behavior of these discharge simulations is shown in Fig. 7.9. Figure 7.9(a-b) illustrate stable operation for discharge simulations with source radii of 2 and 2.5 mm. However, in the larger source radii simulation results shown in Fig. 7.9(c-d), pockets of high plasma temperature within the domain are shown. These significant, local variations in temperature support significant variations in the time domain as

the simulation progresses. The lack of discharge stability is indicative of insufficient ablation to cool and stabilize the plasma core in the 4 and 5 mm source radius simulations. The peak current densities achieved for these simulations were 0.4 and 0.25 kA/mm^2. When operating in steady state, it is expected that discharges at similar current densities would eventually stabilize. But these results indicate that, for a pulsed ET system, higher current densities are required to operate ET plasma discharges in the ablation-controlled arc regime. The simulation results presented in this work can be used to estimate the required peak current densities for certain geometric configurations of a pulsed ET plasma source. This is discussed in more detail in Sec. 7.6.

7.6 Discussion and Conclusions

A two-dimensional model and code have been developed for pulsed ET plasma discharges. The model and code are called the Three-fluid, 2D ET Plasma Flow Simulator (THOR). THOR has been developed in part to understand the effects of source geometry on discharge operating characteristics. Thorough understanding of these characteristics will aid engineers and scientists in the design, operation, and implementation of these devices as mass acceleration systems.

Pulsed operation of ET plasma discharges has been simulated for a range of source radii and peak current densities (see Fig. 7.3). Both the internal source plasma pressure and electric field strength scale well with the scaling laws developed by Niemeyer and Ibrahim

(see Fig. 7.4). This affirms that pressure and electric field scaling laws for steady-state discharges open at both ends are appropriate for pulsed discharge systems open at one end.

ET plasma discharge pressure pulses at varying source radii have been analyzed and shown to change significantly as the source radius increases. These variations have been illustrated for different current pulses with similar current densities and different source radii (see Fig. 7.5). Simulation results indicate that larger source radii produce pressure pulses that are narrower in the time domain. This behavior is expected due to the lower densities that are developed in the source at higher source radii. But this behavior is important for the design of these systems as mass accelerators.

The time variations of the internal plasma temperature have been investigated for current shots with similar peak current densities but varying source radii. Larger radii tend to develop higher core temperatures due to lower core densities (see Fig. 7.6). However, the radial distributions of the plasma temperature reveal lower temperatures developing near the ablating surface for higher source radii (see Fig. 7.7). The results indicate that the average temperature over the source cross section is approximately the same for the different source radii at similar current densities.

The departure from the ablation-controlled arc regime has been qualitatively investigated. While the THOR simulation code is not equipped at this time to accurately simulate all the non-equilibrium effects that arise when operating outside the ablation-controlled arc regime, qualitative observations can still be made regarding general discharge characteristics. As may be expected, low current densities and higher source radii encourage the departure from

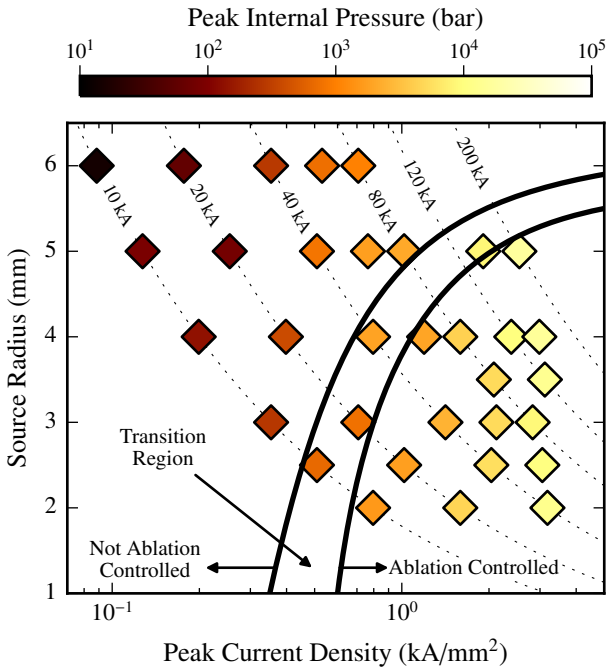

Figure 7.10: Simulated source radius versus peak current density. Individual simulations are represented by data points. Peak internal pressure is indicated for each simulation. Contours indicate values of required peak current. A qualitative estimate of the location of the transition region from the ablation-controlled arc regime is presented.

the ablation-controlled arc regime. Some of the qualitative effects of this departure have been presented (see Fig. 7.9). A qualitative investigation of the simulation results reveals the operating parameters corresponding to a transition region where pulsed ET plasma discharge operation departs from the ablation-controlled arc regime. Figure 7.10 shows the qualitative estimation of these operating parameters for this transition region. The transition region for the departure from the ablation-controlled arc regime is shown to the be dependent on current density and source radius. The results presented in this work focused on a discharge current pulse with different peak currents but the same pulse length. It is expected that increasing the pulse length will expand the ablation-controlled arc region in Fig. 7.10 to

include more source radii and current densities. An analysis of the effect of increasing the pulse length on this transition region has been put off to a later date.

The analyses presented in this work were made possible by the novel 2D modeling and simulation capabilities made available by the development of the THOR simulation code. Estimations and expected behavior of plasma parameters for a range of source geometric configurations have been presented. In addition, the transition from the ablation-controlled arc regime at low current densities and large source radii has been observed qualitatively. The results of this study are very valuable to engineers and scientists seeking to develop and refine designs for ET plasma launchers.

Chapter 8

Conclusions

8.1 Summary

Electrothermal (ET) plasma discharges have a variety of applications to mass acceleration technologies and nuclear fusion energy. These devices have been studied for decades and several simulation models have been developed. These simulation models have included 0D and 1D models with both time-independence and time-dependence. Semi-2D models have also been developed to provide estimations of the radial gradients that develop inside these devices.

As simulation models and diagnostic capabilities have advanced, a deeper understanding of the physical processes involved in ET plasma discharges has continued to emerge. The concept of the vapor shield layer caused by the ablating vapor has been established. The

vapor shield layer involves the shielding of the ablating surface from plasma radiation by the ablated vapor. This vapor shield phenomenon has been experimentally verified [71]. The existence of this vapor shield layer and the quest to correctly simulate its effects on the total ablated mass in these devices has provoked a significant amount of research.

Some authors have sought to capture the ablation phenomenon using kinetic ablation models for the layer separating the ablating surface and the plasma core [33, 84]. These kinetic ablation models have been coupled to 1D simulation models. There have also been several studies that indicate that the shielding effects of the ablating vapor can be captured by simulating the gradients that develop normal to the ablating surface and including the hydrodynamic details of the plasma flow [80,81]. These particular studies have been limited in their applicability, and there is still a need for a fully-2D simulation model of an entire ET plasma discharge device to continue to investigate the ablation phenomenon.

The Three-fluid, 2D ET Plasma Flow Simulator (THOR) model and code have been developed to meet the need for a fully-2D simulation model of ET plasma discharges. The THOR simulation code simulates the time evolution of the electron, ion, and neutral species in the partially ionized plasma using separate sets of governing equations. Due to the 2D nature of the simulation code, THOR is able to simulate the entrance of the ablating vapor into the domain as a surface flux which allows for prediction of the development of the radial gradients that are produced inside these devices. By capturing these important radial gradients, the vapor shield phenomenon can be characterized with greater accuracy and precision than previously possible. The capability of the simulation code goes far beyond

the more detailed simulation of the vapor shield layer and includes the simulation of the effects of inter-species interactions and departure from the ablation-controlled arc regime.

8.2 Conclusions

The THOR simulation code has been used to simulate pulsed ET plasma discharges with nominal peak currents of 10, 20, 30, and 40 kA. These particular discharges have been experimentally performed on the PIPE device [26]. Upon analysis of the simulation results for these discharges, the following conclusions have been made:

- In Chapter 4, the uniquely 2D flow patterns that arise due to inter-species collisions are presented. These patterns involve back-flow of the heavy plasma species near the source centerline. This back-flow of heavy species is caused by frictional drag on these species from the electrons moving toward the cathode at the closed end of the ET source. Simulation results indicate that the frictional drag with the electrons can steepen the pressure gradient near the source exit which causes a lower source exit pressure than may otherwise be predicted. This effect is important in the design of these systems as mass acceleration devices.

- In Chapter 4, the effects of the inclusion of charge exchange reactions are presented. Inclusion of charge exchange reactions affects simulation results most significantly during discharge initialization when the pressures are low (tens of kPa). Typical operation of the ET plasma discharges of interest in this study is several MPa. Following from

this, it was shown that inclusion of charge exchange reactions may only be important at shorter macroscopic time scales and lower discharge pressures.

- In Chapter 5, the back-flow of heavy species caused by collisional drag with electrons is investigated in more detail. This back-flow of heavy species near the centerline of the ET plasma source is eventually redirected at the closed cathode end of the source. This effect encourages the development of plasma-fluid perturbations in this region which can propagate down the axis of the source. These perturbations are shown to become more localized to the cathode end of the source as the peak discharge current increases. A result of this is that, as the peak discharge current increases, less ablation occurs near the cathode region of the source compared with the central region of the source.

- In Chapter 6, the modeling of radiation heat transfer via the diffusion approximation and the use of a black-body radiation approximation are compared. The diffusion approximation for radiation heat transfer is shown to have the capability of correctly capturing the effects of the vapor shield layer. This is evidenced by the lower radiation thermal conductivity that develops near the ablating surface due to the relatively low temperatures and high particle densities. Simulation results for the total ablated mass agree well with experimental measurements for input shot energies greater than 3 kJ. At these higher energies, the vapor shield layer is expected to play an important role in the ablation process.

A parameter study was also performed using the THOR simulation code in order to evaluate the effects of source geometry on pulsed ET plasma discharge operation. This study varied the source radius from 2 to 6 mm, and 100 µs pulses were simulated with peak currents ranging from 10 to 200 kA. This study is presented in Chapter 7. The conclusions of this study are as follows:

- The peak plasma pressure and electric field strength scaling with the peak current density agrees well with theoretical and semi-empirical scaling laws developed by previous authors.

- Increasing the source radius and lowering the peak current density encourages departure of the discharge from the ablation-controlled arc regime. Departure from this regime indicates that the arcs that develop inside these discharges are not sufficiently cooled by ablation and eventually become unstable.

- The parameters required for operation of ET plasma discharges in the ablation-controlled arc regime for the current pulse length investigated were estimated. Based on the simulation results, it is estimated that at source radii greater than 4 mm, a significant increase in the peak current density is required in order to allow the discharge to operate in the ablation-controlled arc regime.

The use of the THOR model and simulation code have extended the knowledge and understanding of ET plasma discharges by providing detailed simulation information regarding important phenomena. Unique and novel features of the THOR model and code have allowed

for numerical observations that have never before been possible. The development of this model and code represent a major step forward in the simulation and modeling capabilities of ET plasma discharges. Conclusions reported in this work as well as conclusions yet to be drawn from simulation results will aid in the design and implementation of these devices.

8.3 Future Work

The fully-2D modeling efforts for pulsed ET plasma discharges have only just begun. The impact of continued research in this area is expected to be significant as ET plasma discharges become more and more important in emerging technologies. Proposed directions for future work are presented below:

- Implementation of geometric transformations in order to simulate a tapered ET plasma source in 2D would advance the concept of using this configuration to enhance the performance of ET plasma discharges.

- Modeling of energetic eroding materials with combustion in order to perform more detailed analyses of the physical processes that are involved in this type of operation.

- Enhancement of the model used for radiation heat transfer in order to improve ablated mass predictions.

- Detailed modeling of the plasma plume exiting an ET plasma discharge in order to provide direct comparison with measurements taken from this region.

- Detailed non-equilibrium modeling and further analysis of the departure from the ablation-controlled arc regime.

Bibliography

[1] M. Mitchner and C. Kruger, *Partially Ionized Gases*. New York, NY: John Wiley & Sons, 1973, no. p. 36.

[2] J. Bittencourt, *Fundamentals of Plasma Physics*. New York, NY: Springer, 2010, no. 3rd edn.

[3] R. Thompson, "Fully coupled fluid and electrodynamic modeling of plasmas: A two-fluid isomorphism and a strong conservative flux-coupled finite volume framework," Ph.D. dissertation, University of Tennessee, Knoxville, TN, 2013.

[4] D. Griffiths, *Introduction to Electromagnetics*, 3rd ed. Boston, MA: Addison-Wesley, 1998.

[5] M. R. Zaghloul, M. A. Bourham, J. M. Doster, and J. D. Powell, "On the average electron-ion momentum transport cross-section in ideal and non-ideal plasmas," *Phys. Lett. A*, vol. 262, no. 1, pp. 86–89, 1999.

[6] A. Winfrey, "A numerical study of the non-ideal behavior, parameters, and novel applications of an electrothermal plasma source," Ph.D. dissertation, North Carolina State University, Raleigh, NC, 2010.

[7] L. Woods, *An Introduction to the Kinetic Theory of Gases and Magnetoplasmas*. New York, NY: Oxford University Press, 1993.

[8] P. Bellan, *Fundamentals of Plasma Physics*. Cambridge University Press, 2006.

[9] R. Cohen, L. S. Jr., and P. Routly, "The electrical conductivity of an ionized gas," *Phys. Rev.*, vol. 80, no. 2, pp. 230–238, 1950.

[10] L. S. Jr. and R. Harm, "Transport phenomena in a completely ionized gas," *Phys. Rev.*, vol. 89, no. 5, pp. 977–981, 1953.

[11] R. J. Zollweg and R. W. Liebermann, "Electrical conductivity of nonideal plasmas," *J. Appl. Phys.*, vol. 62, no. 9, 1987.

[12] T. C. S. Chapman, *The Mathematical Theory of Non-uniform Gases: An Account of the Kinetic Theory of Viscosity, Thermal Conduction, and Diffusion in Gases*, 3rd ed. New York, NY: Cambridge University Press, 1990.

[13] J. Lamarsh and A. Baratta, *Introduction to Nuclear Engineering*, 3rd ed. Upper Saddle River, New Jersey: Prentice Hall Inc., 2001.

[14] "Outline history of nuclear energy," World Nuclear Association, March 2014. Web. Accessed March 10, 2016, http://www.world-nuclear.org/information-library/current-and-future-generation/outline-history-of-nuclear-energy.aspx.

[15] "Us nuclear power plants," Nuclear Energy Institute, Web. Accessed March 10, 2016, http://www.nei.org/Knowledge-Center/Nuclear-Statistics/US-Nuclear-Power-Plants.

[16] D. Burke, Wikipedia, 2006, Web. Accessed December 29, 2015, [Image] https://en.wikipedia.org/wiki/File:Toroidal_coord.png.

[17] E. T. Meier and U. Shumlak, "A general nonlinear fluid model for reacting plasma-neutral mixtures," *Physics of Plasmas*, vol. 19, no. 072508, p. 072508, 2012.

[18] J. P. Trelles, J. V. R. Heberlein, and E. Pfender, "Non-equilibrium modelling of arc plasma torches," *J. Phys. D: Appl. Phys.*, vol. 40, pp. 5937–5952, 2007.

[19] T. Deconinck, S. Mahadevan, and L. Raja, "Computational simulation of coupled nonequilibrium discharge and compressible flow phenomena in a microplasma thruster," *J. Appl. Phys.*, vol. 106, no. 063305, 2009.

[20] D. Breden, K. Miki, and L. Raja, "Self-consistent two-dimensional modeling of cold atmospheric-pressure plasma jets/bullets," *Plasma Sources Sci. Tehcnol.*, vol. 21, no. 034011, 2012.

[21] T. Deconinck, S. Mahadevan, and L. L. Raja, "Simulation of direct-current surface plasma discharge phenomena in high-speed flow actuation," *IEEE Trans. Plasma Sci.*, vol. 35, no. 5, pp. 1301–1311, 2007.

[22] J. D. Bukowski, D. B. Graves, and P. Vitello, "Twodimensional fluid model of an inductively coupled plasma with comparison to experimental spatial profiles," *J. Appl. Phys.*, vol. 80, no. 5, p. 2614, 1996.

[23] U. Shumlak and J. Loverich, "Approximate riemann solver for the two-fluid plasma model," *J. Comput. Phys.*, vol. 187, pp. 620–638, 2003.

[24] M. R. Zaghloul, M. A. Bourham, and J. M. Doster, "Semi-analytical modelling and simulation of the evolution and flow of ohmically-heated non-ideal plasmas in electrothermal guns," *J. Phys. D: Appl. Phys.*, vol. 34, pp. 772–786, 2001.

[25] M. R. Zaghloul, "Improved modelling of electrothermal plasma source with radiation transport," *J. Phys. D: Appl. Phys.*, vol. 41, no. 225206, pp. 1–10, 2008.

[26] A. L. Winfrey, M. A. A. Al-Halim, J. G. Gilligan, A. V. Saveliev, and M. A. Bourham, "A study of plasma parameters in a capillary discharge with calculations using ideal and nonideal plasma models for comparison with experiment," *IEEE Trans. Plasma Sci.*, vol. 40, no. 3, pp. 843–852, 2012.

[27] J. Echols, "Investigation of tungsten surface effects under high heat flux conditions," Master's thesis, Virginia Tech, Blacksburg, VA, 2014.

[28] M. Hamer, "Design of optical measurements for electrothermal plasma discharges," Master's thesis, Virginia Tech, Blacksburg, VA, 2014.

[29] E. Z. Ibrahim, "The ablation dominated polymethylmethacrylate arc," *J. Phys. D: Appl. Phys.*, vol. 13, pp. 2045–2065, 1980.

[30] P. Kovitya and J. J. Lowke, "Theoretical predictions of ablation-stabilised arcs confined in cylindrical tubes," *J. Phys. D: Appl. Phys.*, vol. 17, pp. 1197–1212, 1984.

[31] C. B. Ruchti and L. Niemeyer, "Ablation controlled arcs," *IEEE Trans. Plasma Sci.*, vol. PS-14, no. 4, pp. 423–434, 1986.

[32] L. Niemeyer, "Evaporation dominated high current arcs in narrow channels," *IEEE Trans. Power App. Syst.*, vol. PAS-97, no. 3, pp. 950–958, 1978.

[33] M. Keidar and I. D. Boyd, "Ablation study in the capillary discharge of an electrothermal gun," *J. Appl. Phys.*, vol. 99, p. 053301, 2006.

[34] N. N. Ogurtsova, I. V. Podmoshenskii, and P. N. Rogovtsev, "Calculation of the parameters of an optically dense plasma obtained by a discharge with an evaporating wall," *High. Temp.*, vol. 9, no. 3, 1971.

[35] R. L. Burton and P. Turchi, "Pulsed plasma thruster," *J. Propul. Power*, vol. 14, no. 5, pp. 716–735, 1998.

[36] M. Keidar, I. D. Boyd, and I. I. Beilis, "Electrical discharge in the teflon cavity of a coaxial pulsed plasma thruster," *IEEE Trans. Plasma Sci.*, vol. 28, no. 2, pp. 376–385, 2000.

[37] ——, "Model of an electrothermal pulsed plasma thruster," *Journal of Propulsion and Power*, vol. 19, no. 3, pp. 424–430, 2003.

[38] L. Pekker, "Zero-dimensional time-dependent model of high-pressure ablative capillary discharge for plasma thrusters," *Journal of Propulsion and Power*, vol. 25, no. 4, pp. 958–969, 2009.

[39] L. Pekker and O. Pekker, "Model of high-pressure ablative capillary discharge for plasma thrusters," *Journal of Propulsion and Power*, vol. 27, no. 2, pp. 477–484, 2011.

[40] J. R. Greig, J. Earnhart, and N. Winsor, "Investigation of plasma-augmented solid propellant interior ballistic processes," *IEEE Trans. Magn.*, vol. 29, no. 1, pp. 555–560, 1993.

[41] C. M. Edwards, M. A. Bourham, and J. G. Gilligan, "Experimental studies of the plasma-propellant interface for electrothermal-chemical launchers," *IEEE Trans. Magn.*, vol. 31, no. 1, pp. 404–409, 1995.

[42] R. W. Kincaid and M. A. Bourham, "Electrothermal plasma gun as a pellet injector," *J. Fusion Technol.*, vol. 26, no. 3, pp. 637–641, 1994.

[43] R. Alimi, L. Bakshi, E. Kot, N. Shafir, D. Forte, and M. Sudai, "Experimental ballistic improvement in a pure electrothermal (et) 25-mm gun," *IEEE Trans. Magn.*, vol. 43, no. 1, pp. 284–288, 2007.

[44] J. D. Powell and A. E. Zielinski, "Capillary discharge in the electrothermal gun," *IEEE Trans. Magn.*, vol. 29, no. 1, pp. 591–596, 1993.

[45] J. D. Hurley, M. A. Bourham, and J. G. Gilligan, "Numerical simulation and experiment of plasma flow in the electrothermal launcher sirens," *IEEE Trans. Magn.*, vol. 31, no. 1, pp. 616–621, 1995.

[46] R. L. Burton, S. A. Goldstein, D. A. Tidman, S. Y. Wang, N. K. Winsor, and F. D. Witherspoon, "Emet technology for rail launchers," *IEEE Trans. Magn.*, vol. Mag-22, no. 6, pp. 1410–1415, 1986.

[47] R. L. Burton, F. D. Witherspoon, and S. Goldstein, "The emet railgun projectile," *IEEE Trans. Magn.*, vol. 27, no. 1, pp. 527–532, 1991.

[48] F. D. Witherspoon, R. L. Burton, and S. A. Goldstein, "A second generation emet railgun for secondary arc studies," *IEEE Trans. Magn.*, vol. 27, no. 1, pp. 91–96, 1991.

[49] G. Dale and M. Bourham, "Pulse power system characterization of the plasma interactions with propellants experiment (pipe) electrothermal plasma gun," *IEEE Trans. Plasma Sci.*, vol. 30, no. 5, pp. 1852–1857, 2002.

[50] M. Ryan, "The interaction of an electrothermal plasma with ja2 solid propellant," Ph.D. dissertation, The University of Texas at Austin, Austin, TX, 2006.

[51] A. Porwitzky, "An end-to-end model of an electrothermal chemical gun," Ph.D. dissertation, The University of Michigan, Ann Arbor, MI, 2008.

[52] A. Porwitzky, M. Keidar, and I. Boyd, "Progress towards an end-to-end model of an electrothermal chemical gun," *IEEE Trans. Magn.*, vol. 45, no. 1, pp. 412–416, 2009.

[53] X. Li, R. Li, S. Jia, and Y. Zhang, "Interaction features of different propellants under plasma impingement," *J. Appl. Phys.*, vol. 112, no. 063303, pp. 1–8, 2012.

[54] E. Shcolnikov, A. Chebotarev, Y. Kulikov, A. Melnik, and S. Volkov, "High efficiency electrothermal accelerator," *IEEE Trans. Magn.*, vol. 31, no. 1, pp. 447–451, 1995.

[55] A. L. Winfrey, J. G. Gilligan, and M. A. Bourham, "A computational study of a capillary discharge pellet accelerator concept for magnetic fusion fueling," *J. Fusion Energ.*, vol. 32, pp. 227–234, 2013.

[56] A. L. Winfrey, M. A. Al-Halim, A. V. Saveliev, J. G. Gilligan, and M. A. Bourham, "Enhanced performance of electrothermal plasma sources as fusion pellet injection drivers and space based mini-thrusters via extension of a flattop discharge current," *J. Fusion Energ.*, vol. 32, pp. 371–377, 2013.

[57] T. E. Gebhart, R. T. Holladay, M. J. Esmond, and A. L. Winfrey, "Optimization of fusion pellet launch velocity in an electrothermal mass accelerator," *J. Fusion Energ.*, vol. 33, no. 1, pp. 32–39, 2014.

[58] A. Winfrey, M. A. Al-Halim, S. Mittal, and M. Bourham, "Study of high-enthalpy electrothermal energetic plasma source concept," *IEEE Trans. Plasma Sci.*, vol. 43, no. 7, pp. 2195–2200, 2015.

[59] S. Mittal, "Computational analysis and design of the electrothermal energetic plasma source concept," Master's thesis, Virginia Tech, Blacksburg, VA, 2015.

[60] S. Combs, L. Baylor, S. Meitner, J. Caughman, D. Rasmussen, and S. Maruyama, "Overview of recent developments in pellet injection for iter," *Fusion Engineering and Design*, vol. 87, pp. 634–640, 2012.

[61] L. R. Baylor, N. Commaux, T. C. Jernigan, N. H. Brooks, S. K. Combs, T. E. Evans, M. E. Fenstermacher, R. C. Isler, C. J. Lasnier, S. J. Meitner, R. A. Moyer, T. H. Osborne, P. B. Parks, P. B. Snyder, E. J. Strait, E. A. Unterberg, and A. Loarte, "Reduction of edge-localized mode intensity using high-repetition-rate pellet injection in tokamak h-mode plasmas," *Phys. Rev. Lett.*, vol. 110, no. 245001, 2013.

[62] P. de Vries, M. Johnson, B. Alper, P. Buratti, T. Hender, H. Koslowski, V. Riccardo, and J.-E. Contributors, "Survey of disruption causes at jet," *Nucl. Fusion*, vol. 51, no. 053018, p. 12pp, 2011.

[63] P. L. Taylor, A. G. Kellman, T. E. Evans, D. S. Gray, D. A. Humphreys, A. W. Hyatt, T. C. Jernigan, R. L. Lee, J. A. Leuer, S. C. Luckhardt, P. B. Parks, M. J. Schaffer, D. G. Whyte, and J. Zhang, "Disruption mitigation studies in diii-d," *Phys. Plasmas*, vol. 6, no. 5, pp. 1872–1879, 1999.

[64] M. A. Bourham, J. Gilligan, O. Hankins, W. Eddy, and J. Hurley, "Electrothermal plasma source as a high heat flux simulator for plasma-facing components and launch technology studies," *9th International Conference on High Power Particle Beams*, pp. 1979–1983, May 1992.

[65] J. Gilligan and M. A. Bourham, "The use of an electrothermal plasma gun to simulate the extremely high heat flux conditions of a tokamak disruption," *J. Fusion Energ.*, vol. 12, no. 3, pp. 311–316, 1993.

[66] P. V. Gonzalez, J. Gilligan, A. Winfrey, and M. Bourham, "Generalized scaling laws of plasma parameters in electrothermal plasma sources for fusion disruption erosion and hypervelocity launch applications," *IEEE Trans. Plasma Sci.*, vol. 43, no. 10, pp. 3645–3652, 2015.

[67] J. R. Echols and A. L. Winfrey, "Ablation of fusion materials exposed to high heat flux in an electrothermal plasma discharge as a simulation for hard disruption," *J. Fusion Energ.*, vol. 33, pp. 60–67, 2014.

[68] ——, "Surface effects of low incident angle, high heat flux plasma on tungsten utilizing an electrothermal source," *In Submission.*, no. Manuscript provided courtesy of authors.

[69] J. G. Gilligan and R. B. Mohanti, "Time-dependent numerical simulation of ablation-controlled arcs," *IEEE Trans. Plasma Sci.*, vol. 18, no. 2, pp. 190–197, 1990.

[70] E. Jacob, S. Bouquet, and B. Tortel, "A global theoretical approach for the electrothermal gun: Scaling laws and a 0-d time-dependent model," *IEEE Trans. Magn.*, vol. 31, no. 1, pp. 419–424, 1995.

[71] M. A. Bourham, O. E. Hankins, O. Auciello, J. M. Stock, B. W. Wehring, R. B. Mohanti, and J. G. Gilligan, "Vapor shielding and erosion of surfaces exposed to a high heat load in an electrothermal accelerator," *IEEE Trans. Plasma Sci.*, vol. 17, no. 3, pp. 386–391, 1989.

[72] J. Powell and A. Zielinski, "Theory and experiment for an ablating-capillary discharge and application to electrothermal-chemical guns," Ballistic Research Laboratory, Aberdeen Proving Ground, MD, Tech. Rep. BRL-TR-3355, 1992.

[73] M. Zaghloul, M. A. Na'imi, and M. Bourham, "Measurement of electrical conductivity of weakly nonideal multicomponent plasma mixtures generated from dielectric materials," *IEEE Trans. Plasma Sci.*, vol. 37, no. 8, pp. 1626–1631, 2009.

[74] H. Ngo, M. Bourham, and J. Doster, "Heat and current transport in a metal-vapor electrothermal plasma source for electrothermal-chemical guns," vol. 1. Tucson, AZ: *35th JANNAF Combustion Subcommittee Meeting*, December 1998, pp. 187–197.

[75] Y. Zeldovich and Y. Raizer, *Physics of Shock Waves and High Temperature Hydrodynamic Phenomena*. New York, NY: Academic Press, 1966, vol. 1.

[76] M. Saha, "Ionization in the solar chromosphere," *Phil. Mag.*, vol. 40, no. 238, pp. 472–488, 1920.

[77] J. Gilligan, D. Hahn, and R. Mohanti, "Vapor shielding of surfaces subjected to high heat fluxes during a plasma disruption," *J. Nucl. Mater.*, vol. 162–164, pp. 957–963, 1989.

[78] N. Hahn, "Energy transport through the plasma boundary layer," Ph.D. dissertation, North Carolina State University, Raleigh, NC, 1989.

[79] D. Hahn and J. G. Gilligan, "Radiation transport through a plasma boundary layer between armatures and material surfaces," *IEEE Trans. Magn.*, vol. 27, no. 1, pp. 251–256, 1991.

[80] J. Eapen, "Theoretical and numerical foundations for simulation of ablative plasma flow in electrothermal-chemical mass accelerators," Master's thesis, North Carolina State University, Raleigh, NC, 1998.

[81] N. Orton, "Boundary layer energy transport in plasma devices," Ph.D. dissertation, North Carolina State University, Raleigh, NC, 2000.

[82] M. Keidar, J. Fan, I. D. Boyd, and I. I. Beilis, "Vaporization of heated materials into discharge plasmas," *J. Appl. Phys.*, vol. 89, no. 6, pp. 3095–3098, 2001.

[83] M. Keidar, I. D. Boyd, and I. I. Beilis, "On the model of teflon ablation in an ablation-controlled discharge," *J. Phys. D: Appl. Phys.*, vol. 34, pp. 1675–1677, 2001.

[84] M. R. Zaghloul, "On the vaporization of teflon and heated compound-materials in ablation-controlled arcs," *J. Appl. Phys.*, vol. 95, no. 7, pp. 3339–3343, 2004.

[85] R. Li, X. Li, S. Jia, and A. Murphy, "Comparisons of kinetic ablation models for the capillary discharge," *J. Appl. Phys.*, vol. 108, no. 023301, pp. 1–8, 2010.

[86] ——, "A two-dimensional capillary discharge model considering the ablation and deposition processes," *J. Appl. Phys.*, vol. 110, p. 093302, 2011.

[87] M. R. Zaghloul, "Rosseland and planck mean and multi-group opacities of weakly non-ideal flibe plasma," *Plasma Phys. Control. Fusion*, vol. 49, pp. 1129–1143, 2007.

[88] N. AlMousa, L. Winfrey, J. G. Gilligan, and M. A. Bourham, "Radiative heat transport through vapor plasma for fusion heat flux studies and electrothermal plasma sources applications," *J Nucl Ene Sci Power Generat Technol*, vol. 3:1, pp. 1–7, 2014.

[89] R. Majumdar, J. G. Gilligan, A. L. Winfrey, and M. A. Bourham, "Supersonic flow patterns from electrothermal plasma source for simulated ablation and aerosol expansion following a fusion disruption," *J. Fusion Energ.*, vol. 33, pp. 25–31, 2014.

[90] ——, "Scaling laws of bulk plasma parameters for a 1-d flow through a capillary with extended convergingdiverging nozzle for simulated expansion into fusion reactor chamber," *J. Fusion Energ.*, vol. 34, pp. 905–910, 2015.

[91] A. Winfrey, S. Mittal, and M. A. Al-Halim, "Hyper jet focused-injection tapered capillary plasma source concept," *IEEE Trans. Plasma Sci.*, vol. 43, no. 6, pp. 2104–2109, 2015.

[92] S. Tatsumi, L. Martinelli, and A. Jameson, "Flux-limited schemes for the compressible navier-stokes equations," *AIAA Journal*, vol. 33, no. 2, pp. 252–261, 1995.

[93] C. Laney, *Computational Gasdynamics*. New York, NY: Cambridge University Press, 1998.

[94] K. Miyamoto, *Plasma Physics for Nuclear Fusion*. MIT Press, Revised Edition, 1989.

[95] S. Braginskii, *Review of Plasma Physics edited by M.A. Leontovitch*. New York, NY: Consultants Bureau, 1965, vol. 1, p. 217.

[96] G. S. Voronov, "A practical fit formula for ionization rate coefficients of atoms and ions by electron impact: Z=1-28," *Atomic Data and Nuclear Data Tables*, vol. 65, no. DT970732, pp. 1–35, 1997.

[97] V. Golant, A. Zhilinsky, and I. Sakharov, *Fundamentals of Plasma Physics*. New York, NY: John Wiley & Sons, 1980, no. p. 192.

[98] H. Ngo, "A pseudo-two-dimensional, time-dependent model of the heat and current transport within an electrothermal plasma source," Master's thesis, North Carolina State University, Raleigh, NC, 1998.

[99] G. A. Sod, "A survey of several finite difference methods for systems of nonlinear hyperbolic conservation laws," *J. Comput. Phys.*, vol. 27, pp. 1–31, 1978.

[100] E. Toro, *Riemann Solvers and Numerical Methods for Fluid Dynamics: A Practical Introduction*, 2nd ed. Berlin - Heidelberg, Germany: Springer, 1999, no. pp. 133–136.

[101] J. W. Banks, T. Aslam, and W. J. Rider, "On sub-linear convergence for linearly degenerate waves in capturing schemes," *J. Comput. Phys.*, vol. 227, pp. 6985–7002, 2008.

[102] L. Sedov, *Similarity and Dimensional Methods in Mechanics*, 10th ed. Boca Raton, FL: CRC Press, 1993, no. pp. 261–288.

[103] K. Salari and P. Knupp, "Code verification by the method of manufactured solutions," Sandia National Lab, P.O. Box 5800, Albuquerque, NM 87185-0825, Tech. Rep. SAND2000-1444, 2000.

[104] I. B. Celik, U. Ghia, P. J. Roache, and C. J. Freitas, "Procedure for estimation and reporting of uncertainty due to discretization in cfd applications," *J Fluid Eng-T ASME*, vol. 130, no. 7, p. 078001, July 2008.

[105] L. Woods, *An Introduction to the Kinetic Theory of Gases and Magnetoplasmas*. New York, NY: Oxford University Press, 1993, no. p. 199.

[106] J. Bittencourt, *Fundamentals of Plasma Physics*. New York, NY: Springer, 2010, no. 3rd edn. p. 203.

[107] R. K. Janev and J. J. Smith, "Cross sections for collision processes of hydrogen atoms with electrons, protons and multiply charged ions," *At. Plasma-Mater. Interact. Data Fusion*, vol. 4, no. 1, 1993.

[108] M. J. Esmond and A. L. Winfrey, "Flow characteristics and charge exchange effects in a two-dimensional model of electrothermal plasma discharges," *J. Fusion Energ.*, vol. 35, no. 2, pp. 244–252, 2015.

[109] R. Mohanti, "Time dependent numerical simulation of nonideal plasmas in ablation controlled arcs," Ph.D. dissertation, North Carolina State University, Raleigh, NC, 1990.

[110] M. J. Esmond and A. L. Winfrey, "Estimation of transient effects of > 2 mm radii in electrothermal plasma launchers for fusion fueling," *Transactions of the American Nuclear Society*, vol. 113, pp. 381–384, 2015, washington, D.C., November 8–12, 2015.

[111] R. Li, X. Li, S. Jia, A. Murphy, and Z. Shi, "Study of different models of the wall ablation process in capillary discharge," *IEEE Trans. Plasma Sci.*, vol. 38, no. 4, pp. 1033–1041, 2010.

[112] J. R. Echols and A. L. Winfrey, "Surface effects of low incident angle, high heat flux plasma on tungsten utilizing an electrothermal source," *In Submission*, Manuscript provided courtesy of authors.

[113] V. M. Timokhin, V. Y. Sergeev, and B. V. Kuteev, "Study of discharge quenching in the t-10 tokamak by injecting high-z impurity pellets," *Plasma Phys. Rep.*, vol. 27, no. 3, pp. 181–194, 2001.

[114] E. Z. Ibrahim, "The ablation dominated polymethylmethacrylate arc, correction," *J. Phys. D: Appl. Phys.*, vol. 14, p. 1729, 1981.